Ferdinand-Braun Institut, Leibniz-Institut für Höchstfrequenztechnik

# MOVPE growth and characterization of (In,Ga)N quantum structures for laser diodes emitting at 440 nm

vorgelegt von
Diplom-Physiker
Veit Hoffmann
aus Chemnitz

Von der Fakultät II - Mathematik und Naturwissenschaften
der Technischen Universität Berlin
zur Erlangung des akademischen Grades
Doktor der Naturwissenschaften
- Dr. rer. nat. -

genehmigte Dissertation

Promotionsausschuss:

Vorsitzender: Prof. Dr. M. Lehmann
Gutachter: Prof. Dr. M. Kneissl
Gutachter: PD Dr. habil. A. Dadgar
Gutachter: Prof. Dr. G. Tränkle

Tag der wissenschaftlichen Aussprache: 18.04.2011

Berlin 2011
D83

## Zusammenfassung

Die Arbeit beschreibt die Herstellung von nitrid-basierten Laserheterostrukturen im Wellenlängenbereich zwischen 400 nm und 450 nm mittels Metallorganischer Gasphasenepitaxie. Um Bauelemente mit niedrigen Schwellstrom bzw. - leistungsdichten zu realisieren, wurden die Materialeigenschaften der Indiumgalliumnitrid (InGaN) Multi-Quantenfilme (MQW)s in der aktiven Zone untersucht und mit den Bauelementeigenschaften prozessierter optisch gepumpter Laserstrukturen und elektrisch gepumpter Laserdioden (LD)s korreliert. Weiterhin wurde untersucht, welchen Einfluss die Schichtstruktur der aktiven Zone und des umgebenden Wellenleiters auf die Materialverstärkung und die Verstärkung der Mode in der Laserstruktur hat.

Zunächst wurden 15 - 100 nm dicke InGaN Einzelschichten auf GaN/ Saphir abgeschieden und analysiert, um das InGaN Wachstum und die Entstehung von Materialdefekten zu verstehen. Das spiralförmige Winden der Wachstumsfronten um bestehende Schraubenversetzungen und die Bildung von zusätzlichen v-förmigen Oberflächendefekten wurden als hauptsächliche Ursachen für die Abnahme der kristallinen Perfektion in den InGaN Schichten identifiziert. Die Abkehr vom Stufenflusswachstum und die Bildung von stabilen Facetten mit erhöhtem Indiumeinbau führt zu einer lateralen Variation der Indiumkonzentration in den Schichten, was mittels dynamischer Elastizitätstheorie und der Untersuchung des InGaN- Wachstums auf unterschiedlich orientierten GaN/Saphir Proben erklärt wird.

Anhand von Laserstrukturen mit Emissionswellenlängen um die 400 nm wurden die Materialeigenschaften der InGaN- Quantenfilme mit den Bauelementeigenschaften korreliert: In den dünnen InGaN Quantenfilmen führt die laterale Variation der Indiumkonzentration und der InGaN- Schichtdicke aufgrund des dreidimensionalen Wachstums zu starken lateralen Variationen der Bandlücke. Systematische Untersuchungen von optisch gepumpten Laserstrukturen mit unterschiedlichen Bandkantenfluktuationen zeigten, dass mit zunehmender Variation der Bandkante die Schwellenleistungsdichte der Laser steigt. Die damit einhergehende Verbreitung der Lumineszenzlinienbreite bei niedriger Anregungsdichte ist ein guter Indikator für die Abnahme der Materialverstärkung bei der Emissionswellenlänge. Mittels des gefundenen Zusammenhangs wurden die Wachstumsbedingungen der InGaN Quantfilme optimiert und elektrisch gepumpte Laser mit Schwellstromdichten um 6 $kA/cm^2$ realisiert.

Anschließend an die Optimierung der InGaN- Wachstumsbedingungen zur Verbesserung der InGaN- Materialverstärkung wurde der Einfluss der Schichtstruktur der aktiven Zone und des GaN Wellenleiterkerns auf die modale Verstärkung des Lasers untersucht. Dafür wurden die Strukturen mit verschiedenen Lasersimulationsprogrammen modelliert und die Ergebnisse mit optischen Pumpexperimenten verglichen. Es zeigte sich, dass die Wellenleiterschichtdicke mit zunehmender Emissionswellenlänge erhöht werden muss, um die Abstrahlung der Mode insbesondere ins Substrat zu vermindern.

Neben den Anpassungen des Wellenleiters und der Optimierung der Wachstums-

bedingungen erfordert die Realisierung von Lasern mit höheren Indiumgehalten in den Quantenfilmen für Emissionswellenlängen um die 440 nm eine Anpassung der Heterostruktur der aktiven Zone und einen Wechsel zu defektarmen GaN-Substraten. Mittels Messungen an optisch gepumpten Laserstrukturen und Bauelementsimulationen wird gezeigt, dass durch diese Manahmen die Indiumkonzentrationsfluktuationen in den Quantenfilmen reduziert, das Oszillatormoment erhöht und die Ladungsträgerinjektion in die einzelnen Quantenfilme verbessert werden kann. Eine erste elektrisch betriebene Laserstruktur, gewachsen auf GaN- Substrat mit Emission um 440 nm, zeigte eine Schwellstromdichte von $\simeq 10\,\mathrm{kA/cm^2}$.

# Contents

# 1

# Introduction

## 1.1 Motivation

Compound semiconductor opto-electronic devices are an inherent part of many everyday objects, e.g. light emitting diodes (LED)s, and modern technologies such as laser diodes (LD)s based fiber-optic communication. Due to the narrow band gap of the commonly used arsenide and phosphide compound semiconductor materials the emission and thus the applications are limited to the infra-red to the yellow/green range of the spectrum. Wurzite gallium nitride (GaN) and its alloys exhibit a direct band gap that theoretically covers the emission spectrum from the deep ultra violet (UV) (aluminum gallium nitride - $Al_{1.00}Ga_{0.00}N \simeq 6.2\,eV = 200\,nm$ [1]) to the red (indium gallium nitride - $In_{1.00}Ga_{0.00}N \simeq 0.7\,eV = 1750\,nm$ [2, 3]) wavelength region. Similar to conventional phosphide or arsenide based lights emitters, (In,Ga)N based opto-electronic devices can be cost-efficiently produced in a high number on one wafer enabling new applications in the whole mentioned range of the spectrum. Nevertheless, (In,Ga)N LDs are commercially available only for a limited number of distinct wavelengths and properties that mainly fit the requirements of strong-selling products such as blue-ray disk, laser projectors [4], laser printers and reprographics [5]. Beside the usage in new consumer electronic products nitride based LDs enable more compact and more efficient systems for a wide range of existing applications since LDs outperform conventional solid-state laser systems in terms of lifetime, robustness, size and power consumption.

Fig. 1.1 shows the absorption spectra of pure water with a distinct minimum in the blue wavelength region. Since water covers more than 70% of the earth's surface and is component of every life form the analysis of its resolved ingredients is of great interest in many fields of research and application. For instance, solid state light sources emitting at the absorption minima of water are potentially used in medical applications like single cells cytometry [7] or undersea optical communications [8]. Since the emission wavelength of nitride based LDs is adjustable over a wide range, tailor-made light sources can be realized for solutions with specific absorption minima or for spectroscopic applications in general, e.g. Raman spectroscopy [9], laser- induced fluorescence emission for in-vivo chlorophyll fluorescence [10] or DNA sequencing [11].

The goal of the presented work is the realization of a current injection semiconductor laser diode (LD) emitting at 435.9 nm. The wavelength corresponds to the $7^3S_1 - 6^3P_1$

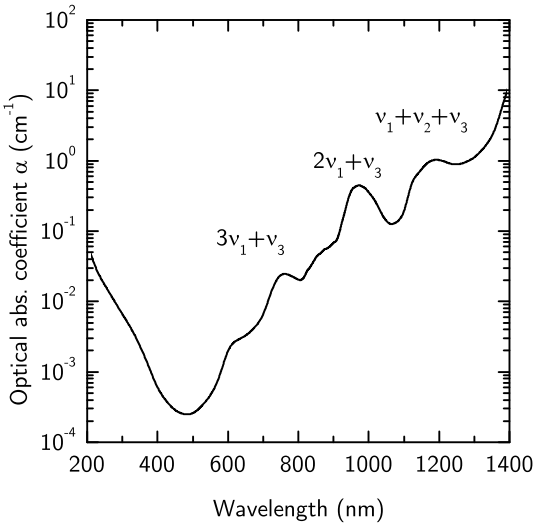


Figure 1.1: Absorption spectra of pure water showing lowest absorption in the blue wavelength region [6]. Wavelengths of increased absorption due to the distinct vibrational modes (symmetric stretching $\nu_1$, symmetric bending $\nu_2$ and asymmetric stretching $\nu_3$) are marked.

line of atomic mercury [12] in gas-discharge lamps, which is used for many biomedical and technical applications such as malaria [13] or tuberculosis [14] diagnosis, cell [15] and neural [16] research, fluorescence microscopy for chemical analysis [17] food safety and environmental testing [18].

## 1.2 (Al,In,Ga)N growth challenges

(Al,In,Ga)N device development starts with the specification of the heterostructure design. In general, LD heterostructures involve a high number of layers with different alloy compositions. The layer heterostructure is deposited on a GaN or a hetero-substrate, such as sapphire, silicon or silicon carbide by metal organic vapor phase epitaxy (MOVPE). Detailed information on the growth method can be found elsewhere [19, 20]. In order to reveal the optimum growth conditions for every single layer, the preparation of the different alloys is investigated before assembling the heterostructure. The realization of (Al,In,Ga)N with a high material quality represents a huge challenge due to the big differences in the material properties (especially the lattice constant) and the optimum growth conditions of the different binary compounds. Historically, the mastering of the MOVPE alloy formation limitations was the key to the realization of GaN based opto-electronic devices. Still, the MOVPE growth process significantly determines the material properties and quality and its mastery is of great importance for the realization of efficient GaN-based devices. Hereafter, crucial aspect of the (Al,In,Ga)N laser diode heterostructures growth are discussed.

The breakthroughs of the GaN technology was the achievement of p-doping using magnesium (Mg) [21, 22]. Due to the high activation energy of the acceptor of around 170 meV in GaN [23] and its passivation through the formation of Mg-H complexes [24] high Mg concentrations are required in order to realize sufficient p-type conductivity as well as low resistance p-type contacts. However, a high Mg concentration can cause compensation [25] of the holes and deteriorate the crystal perfection of the p-doped material by formation of clusters and other defects [26]. In order to obtain p-type doped material with both a high conductivity and a high material quality the

optimum doping level and growth conditions resulting in a low compensation and a high Mg incorporation need to be determined.

The light emitting region of the LDs is embedded in a GaN waveguide core between AlGaN layers with a lower refractive index with respect to the effective index of the mode in the active region. This way the mode is vertically confined in theGaN waveguide core, guaranteeing a high optical intensity in the gain region of the device. The refractive index difference as well as the lattice mismatch strain in the heterostructure increase as the Al mole fraction of the cladding layer increases. Exceeding a critical AlGaN layer thickness and / or Al mole fraction layer cracking occurs [27] that massively disturbs the laser operation. The challenge regarding device realization is the optimization of the waveguiding structure, e.g. finding a good compromise between(Al,Ga)N layer thicknesses and Al mole fraction in the layers.

The active region consists of an InGaN/(In)GaN multiple quantum well (MQW) structure in order to confine the carriers in the InGaN QWs by /(Al,In)GaN barriers with a higher band gap energy. This way efficient radiative recombination is achieved. As a consequence of the different spontaneous and piezoelectric polarization of GaN and indium nitride (InN) [28] a non-vanishing dipole moment occurs resulting in high sheet carrier densities at the interfaces. The consequential electrical field strength is proportional to the gradient of the dipole moment at the interface. The electric field is perpendicular to the {0001} direction and spatially separates the holes and electrons in the quantum well when growing on the c-plane parallel to (0001). The separation of the carriers reduces the oscillator strength [29] and red-shifts the emission energy due to the quantum confined Stark effect [30].

Beside the oscillator strength, the crystal perfection of the active region, e.g. number of defects, interface roughness and material property uniformity, determines the material gain of the laser structure. The material quality in turn strongly depends on the In mole fraction in the solid of the active region [31] since the high lattice mismatch between InN and GaN [32] is a dominant driving force for material deterioration. The compressive strain of the InGaN forces defect formation or transition from layer by layer to 3D growth mode. Secondly, the low In incorporation efficiency at optimum GaN growth conditions of around 1000 °C requires low InGaN deposition temperatures of 700 °C. Because of the high In vapor pressure [33] and the high covalent radius of the In atom (1.44 Å) in comparison to the Ga atom (1.26 Å) the In is likely to desorb from the surface instead of being incorporated into the GaN. At low InGaN deposition temperatures the decomposition of the nitrogen precursor ammonia ($NH_3$) is reduced which causes the formation of point defects due to N deficiency in the layer [34]. Furthermore, the reduced mobility of the adducts on the growth surface at low growth temperatures prevents layer by layer growth. The challenge regarding InGaN growth is the determination of the best compromise between well thickness and In mole fraction in the solid and the optimization of the growth conditions for the best possible material quality.

## 1.3 Approach and organization of the work

The work focuses on the MOVPE growth and analysis of (In,Ga)N quantum well structures as well as the optimization and simulation of (Al,Ga)N waveguiding structures in order to improve the material properties as well as the modal gain of laser diodes emitting around 440 nm. Therefore, various sample structures and analysis methods are used. The growth and characterization parameters are described in chapter 2.

In chapter 3, the preparation and analysis of 15 nm and 120 nm thick InGaN single layers on GaN are discussed. Due to the high layer thicknesses the lateral and vertical distribution of the In can by determined by several methods. Additionally, the lower number of interfaces as well as the lower intrinsic fields strengths in the single layer structure, in comparison to MQW structures, simplifies the interpretation of the measurement results. The analysis and interpretation of the results reveal aspects of the In incorporation processes into GaN as well as fundamental InGaN material deterioration processes.

Next, described in chapter 4, InGaN layers are embedded into GaN barrier layers in order to form MQW structures. By varying the well width the indium gallium nitride (InGaN) /GaN heterostructure properties, e.g. In mole fraction in the solid, and their effect on the intrinsic field strength, the crystal perfection and luminescence efficiency are revealed. As a consequence of the increased structural complexity the exact determination of material properties is challenging and will be extensively described. The analysis of the influence of the QW width on the material quality and luminescence in the described experiments allows the specification of heterostructure parameters for the laser diode structures. Furthermore, by comparing the experimental results with theory the material parameters, used in the laser simulation later on, are adjusted.

In chapter 5, the influence of the MOVPE growth conditions, e.g. the growth temperature, on the material as well as luminescence properties of MQW structures is revealed. Furthermore, an experimental procedure is introduced that allows to correlate material properties, derived on MQW structures, with actual device properties. Using a multi-step epitaxy approach different heterostructures, e.g. MQWs, optical pumpable and current injection laser structures, are produced allowing for a valid comparison. The different structures contain identical active regions, which enables the determination of the material properties, e.g. the active region interface roughness, the In mole fraction in the solid and its spatial uniformity, and the device properties, e.g. threshold current density, output power and modal gain, at the same time. Unfortunately, the analysis of the results reveals a huge impact of the varied growth parameters on both the material quality and the optical confinement resulting in a simultaneous variation of the material gain and the modal gain.

In order to distinguish between the different effects on the device properties and enable growth optimization for laser heterostructures samples with identical modal gain but different material quality in the active region are prepared and analyzed (see chapter 6). Similar to chapter 5 the active region growth temperature is varied in

order to affect the material quality. But this time the In mole fraction in the vapor is adjusted in order to realize identical In mole fractions in the quantum wells and barriers and thus identical modal gain in all samples. Analyzing the MQWs as well as the optical pumpable structures, the correlation of low threshold power densities with different growth conditions or respectively material properties is revealed. Using the characterization method that is most sensitive to the desired material properties a growth optimization scheme for laser heterostructures is established.

The basic developments have been made using laser diodes emitting around 400 nm since this wavelength is used in Blue-Ray disc storage systems and thus allows for a comparison with the well documented state of the art. Secondly, the 400 nm LDs feature moderate In mole fraction in the QWs facilitating the preparation of active regions with a good material quality. In order to realize emission at longer wavelengths both the material but also waveguiding losses at longer wavelengths need to be reduced. The optimization of the heterostructure layout as well as the growth conditions for 440 nm LD structures is addressed in chapter 7.

Due to economic reasons the heterostructures were deposited on sapphire based GaN templates with a high defect density. In the first part in section 7.1, the growth on low defect GaN substrates is discussed in order to decrease the number of threading dislocations in the active region and thus increases the material gain. Transferring the growth to GaN substrates one has to deal with different wafer bow resulting in different surface temperatures across the wafer. This in turn results in a lateral non-uniformity of the material properties and thus device characteristics. Growth experiments as well as simulations of the wafer bow during MOVPE growth will be described in order to specify GaN substrate properties that result in an identical uniformity of the wafer surface temperature as on sapphire substrate.

Next, in section 7.2, the influence of the waveguiding design on the optical confinement of the optical mode is discussed. Using device simulation as well as optical pumpable laser heterostructure variations the optical confinement at longer wavelengths is improved. After increasing the modal gain, the influence of modifications of the active region heterostructure layout on the material quality or respectively material gain is revealed in section 7.3. Using the optimization scheme established before the growth conditions of the active region are improved. Applying the optimized active region growth conditions together with the optimized waveguiding structure a 440 nm laser heterostructure is grown on low defect density GaN substrate. After processing of the wafer to an broad area laser diode (BA-LD) lasing at 436 nm in pulsed mode will be shown.

# 2

# Experimental

This chapter provides an overview of the MOVPE growth process and introduces the different heterostructure layouts used for the experiments. Furthermore, the wafer processing and the analytical methods are explained.

## 2.1 MOVPE growth and heterostructure layout

All samples discussed in this work are grown on either a horizontal Aixtron AIX 200HT reactor with 1×2 inch configuration (Aix200-HT) or a horizontal Aixtron AIX 2400G3-HT planetary reactor with 11×2 inch configuration (Aix2400G3-HT). Both machines are equipped with a LayTec EpiCurveTT growth monitoring system, detecting the wafer reflectometry, curvature and satellite pocket temperature during growth. Additionally, a LayTec Pyro400 sensor is used for some experiments in order to determine the wafer surface temperature.

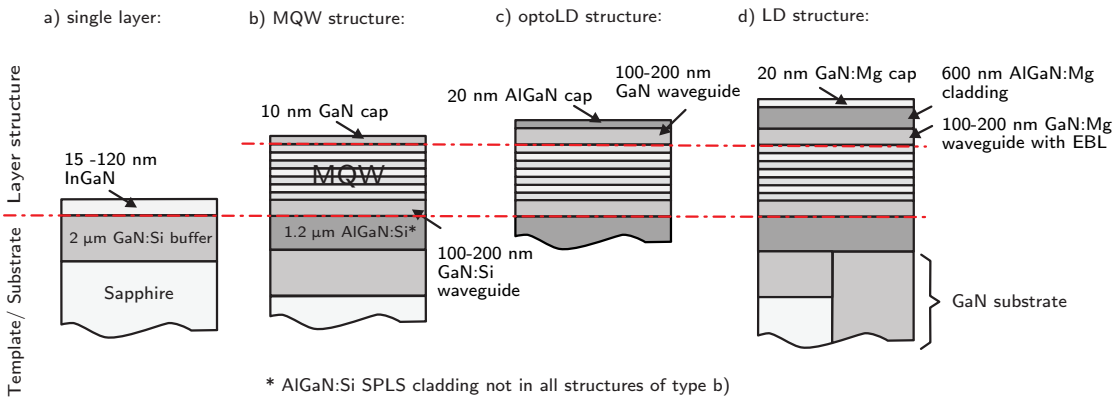


Figure 2.1: Schematic of the sample structures used in this chapter and in chapter 3.

In order to fit the requirements of the different characterization methods various heterostructure are grown. Fig. 2.1 gives an overview of the sample structures used for (Al,In,Ga)N material as well as device development within this work.

### 2.1.1 Sapphire-based GaN template growth

In general, sapphire is used as substrate for the deposition of the (Al,In,Ga)N layers. In order to compensate for the high lattice mismatch between sapphire and GaN an elaborate growth scheme is applied described in this section. Since the growth process is rather time consuming 11 sapphire wafer with a GaN layer on top are grown at the same time in the Aix2400G3-HT and used as templates for the different experiments later on.

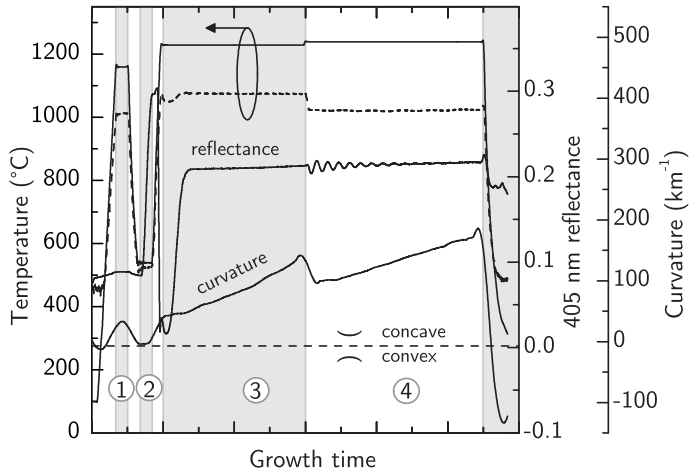


Figure 2.2: In-situ data showing $T_{\mathrm{proc}}$ (solid line), $T_{\mathrm{pocket}}$ (broken line), the reflectivity at 405 nm (green line) and wafer curvature (blue line) during MOVPE growth of a sapphire based GaN template ($T_{\mathrm{(Al)GaN:Si}}$) in the Aix2400G3-HT.

Fig. 2.2 shows the in-situ data monitored during the GaN template preparation by MOVPE. The red lines represent the process (solid line) and the pocket temperature (broken line) that are pyrometrically measured at the backside of the RF-heated susceptor and the frontside of the satellite, respectively. The temperature of the pocket is lower with respect to the process temperature since the RF-radiation is absorbed by the graphite in the susceptor which itself heats the satellites by radiation. The green and blue line correspond to the reflectance of the wafer at 405 nm and the curvature of the wafer, respectively. The reflectometry signals at 405 and 950 nm (not shown here) is used for process control and growth rate determination by fitting of the Fabry-Perot interferences.

The GaN growth scheme on sapphire was proposed by Nakamura et al. [35] and is based on the relief of lattice mismatch strain by a low temperature GaN nucleation layer. The threading of the consequential misfit dislocations from the sapphire/GaN interface is suppressed by an AlGaN/GaN short-period superlattice (SPSL) [36]. Since the effective index of the 240 × $Al_{0.12}Ga_{0.88}N$/GaN:Si SPSL (2.5 / 2.5 nm) has a lower refractive index with respect to the effective index of the mode it also works as a n-side cladding layer if the template is used for the growth of a laser structure emitting between 400 and 450 nm.

The growth process starts with a high temperature adsorbate desorption in hydrogen ($H_2$) environment followed by a nitridation of the sapphire using $NH_3$ (see (1) in Fig. 2.2). After that, a low temperature (LT)-GaN buffer is deposited using trimethylgallium (TMGa) additionally to $NH_3$ (2). Clearly, the reflectivity decreases as a consequence of the light scattering on the GaN 3D nuclei in the LT-GaN buffer. With increasing temperature the island coalesce resulting in an increase of the layer reflectance. In step (3) a 4 $\mu$m thick HT-GaN buffer layer is grown using TMGa and $NH_3$ followed by the deposition of a 1.2 $\mu$m thick AlGaN/GaN SPSL using additionally trimethylaluminum (TMAl) (4) before cool down. $Si_2H_6$ is injected during GaN and AlGaN growth in order to provide n-type conductivity. The n-doping level of the GaN buffer and the AlGaN SPSL layer are 3 and 1.5 $\times$ $10^{18}$ $cm^{-3}$. The growth pressures are 200 mbar during nucleation, 400 mbar for GaN:Si and 60 mbar for AlGaN/ GaN:Si SPSL growth. The AlGaN is grown at reduced pressure in order to reduce the precursor pre-reactions in the gas phase [37] and enhance the surface morphology and the material quality [38].

The curvature change during growth shown in Fig. 2.2 can be explained according to the epi-layer on substrate model proposed by Stoney [39]. During heating up to desorption temperature the curvature changes from -15 $km^{-1}$ (convex) to 50 $km^{-1}$ (concave). The change is attributed to the different temperatures at the frontside and the backside of the wafer (due to its limited thermal conductivity) and the consequential different thermal expansion. During the deposition of the 4 $\mu$m thick GaN:Si the curvature increases from 50 to 150 $km^{-1}$. The observed change can be explained by a decrease of the defect density as the GaN layer thickness increases [40]. The consequential decrease of the in-plane lattice constant increases the strain and therefore the wafer curvature [41]. The curvature increases during deposition of the 1.2$\mu$m thick AlGaN/GaN:Si SPSL by $\sim$60$km^{-1}/\mu$m in comparison to $\sim$12$km^{-1}/\mu$m for GaN:Si. The higher curvature change is due to the additional AlGaN lattice mismatch strain. During cool down to room temperature the wafer curvature changes from concave to convex due to the higher thermal expansion of the sapphire in comparison to the (Al,Ga)N epi-layer [42].

### 2.1.2 (In,Ga)N sample growth

The fundamental InGaN growth conditions are determined by low indium (In) incorporation in GaN at high temperatures [43] and in $H_2$ environment [44]. Due to this the growth is conducted at temperatures between 700 °C and 900 °C and in $N_2$ environment. TMIn and triethylgallium (TEGa) are used as group III and $NH_3$ as group V precursor. The reactor pressure amounts to 200 (Aix200-HT) and 400 mbar (Aix2400G3-HT) for InGaN growth, depending on the used machine.

InGaN bulk layer structures (see sample type a) in Fig. 2.1) are deposited on differently oriented GaN templates in order to determine the layer growth rate and the vertical and lateral In mole fraction distribution in the layer. The In distribution in thin layer is investigated on InGaN /(In)GaN MQW structures of type b). Efficient luminescence is observed and investigated since the holes and electrons are spatially

confined in the band gap minima of the quantum wells increasing the probability of a radiative recombination. The MQW is capped with 10-50 nm GaN in order to reduce surface effects on the recombination.

### 2.1.3 Device heterostructure growth

Optically pumpable laser heterostructures of type c) in Fig. 2.1 are realized by adding a 100 - 200 nm thick GaN wave guiding layer and a 20 nm thick $Al_{0.2}Ga_{0.80}N$ cap on top of the MQW described above. The growth temperatures of the waveguide and the cap are 900 °C in order to prevent the deterioration of the active region underneath. The AlGaN cap provides a band offset and reduces the recombination of the optically generated carriers in surface states.

The current-injection LD heterostructures of type d) feature a 100 - 200 nm p-type doped GaN:Mg waveguide including a $Al_{0.20}Ga_{0.80}N$:Mg electron blocking layer (EBL). Due to the higher band gap energy the AlGaN EBL prevents the electron overflow from the active region to the p-type contact [45]. On top of the p-GaN waveguide a 120× $Al_{0.12}Ga_{0.88}N$/ GaN:Mg SPSL cladding and a 20 nm GaN:Mg cap layer are deposited. The growth pressure is 250 mbar for the (Al)GaN:Mg growth, biscyclopentadienylmagnesium ($Cp_2Mg$) is used as Mg source. The doping levels in the EBL, waveguide and cladding layer are 1-2×$10^{17}$ $cm^{-3}$. The p-doping level is a compromise between low p-type conductivity for low doping levels and high compensation trough defects [25] and absorption by sub-band gap states [46] at high doping level. The p-doping level of the cap is 5×$10^{17}$ $cm^{-3}$ in order reduce the semiconductor-metal contact resistivity.

## 2.2 Sample characterization methods

The surface of both InGaN single layer and MQW samples is inspected by light microscopy using a Zeiss Axiotron II optical microscope featuring Nomarski contrast or a JEOL 840A scanning electron microscope (SEM). To obtain quantitative information about the surface morphology, e.g. $r_{rms}$ roughness, the samples are investigated by atomic force microscopy (AFM) using a Topometrix Explorer AFM featuring contact mode or a Digital Nanoscope III AFM system featuring tapping mode. It is possible to investigate a full 2 inch wafer using the Topometrix Explorer, whereas the Digital Nanoscope III exhibits a better height resolution due to the tapping mode operation.

The layer growth rate is determined using different methods depending on the layer thickness. The observation of the Fabry-Perot oscillations obtained by the EpiCurveTT sensor during growth is particularly suited for thick layers. Since 75 nm of GaN are necessary in order to obtain a full 405 nm reflectometry oscillation, primarily the GaN buffer and the AlGaN cladding layer thickness are characterized by this method. InGaN or AlGaN single layers with thicknesses between 10 and 100 nm or MQW structures are analyzed using a PANalytical X'Pert high resolution x-ray diffraction (HR-XRD) system. Additionally to the thickness the composition of the

layers can be fitted by comparing the $\Omega - 2\Theta$ scans around the (0002) or (0006) reflection with simulations of the heterostructure using dynamical diffraction theory [47]. Mapping around asymmetric reflections, e.g. reciprocal space mapping (RSM) around $(10\bar{1}5)$, additionally allows the determination of the layer relaxation. Furthermore, the layer thickness and composition of thin InGaN and AlGaN layers (also in MQW structures) close to the surface are analyzed by high resolution x-ray reflectometry (HR-XRR). The layer thickness and composition are fitted using dynamical theory of X-ray reflection with a matrix approach [48].

The luminescence properties are determined by photoluminescence (PL) and low temperature cathodoluminescence (LT-CL). The PL is measured by excitation with a continuous wave (CW) helium cadmium (HeCd) laser emitting at 325 nm or a 378 nm CW LD. The latter is used to resonantly excite the InGaN quantum wells and not the GaN layers or the quantum barriers with low In mole fraction in the solid. The excitation power densities of both systems can be varied between 0.1 and 100 $\mathrm{W/cm^2}$ resulting in an excess charge carrier density in the quantum wells between $10^7$ to $10^{12}\,\mathrm{cm^{-2}}$ (also depending on the effective recombination time). The sample temperature can be varied between 10 and 300 K in a closed cycle helium cryostat in order to enable temperature-dependent photoluminescence (TD-PL) measurements. The luminescence is detected with a spectrometer with linear response to the detected light power.

Furthermore, time-resolved photoluminescence (TR-PL) measurements are conducted at 10 K by using 200 ps pulses from a 405 nm LD for excitation. The spectrally integrated time-dependent intensity is detected by a fast avalanche photo diode with a time resolution of 20 ps to enable single photon counting. The excitation pulse energy density was about 1 $\mathrm{nJ/cm^2}$.

For LT-CL investigations around 5.5 K a Zeiss Ultra55 scanning electron microscope equipped with a Gatan Mono-CL3 system is used. LT-CL spectra and monochromatic LT-CL images were acquired simultaneously with inspection of the surface by SE. Using an accelerating voltage and electron probe current of 5 kV and 200 pA the LT-CL excitation depth is about 120 nm. Secondly, LT-CL measurements at 80 K are conducted on an Oxford LT-CL system attached to the JEOL 840A SEM tool.

## 2.3 Device processing and characterization

The optically pumpable structures are scribed from the substrate side using a laser scriber and broken into 800 to 1500 $\mu$m long laser bars as shown in Fig. 2.3. The optical pumping experiments are carried out at room temperature using a 266 nm frequency quadrupled Nd:YAG laser. For resonant optical pumping a tunable dye laser based on the organic dye BiBuQ with an emission energy of 3.266 eV (380 nm) is used instead of the Nd:YAG excitation source. The Nd:YAG pump laser is operated in pulsed mode at a low 15 Hz repetition frequency and pulse widths of about 5 ns. This way a high pulse aspect ratio is obtained, leading to high pump powers and

Figure 2.3: Laser bars for optical pumping experiments with resonator length between 800 and 1500 $\mu$m on a gel pad.

minimal thermal stress on the sample. By focusing the light to a small area on the sample pump powers of several MW/cm$^2$ are achieved. The emitted light is detected by an optical-fiber CCD spectrometer. The intensity of the pump beam is reduced by a beam attenuator in order to enable measurements of the L-I characteristics. Further reading about the processing and characterization through optical pumping can be found elsewhere: [49].

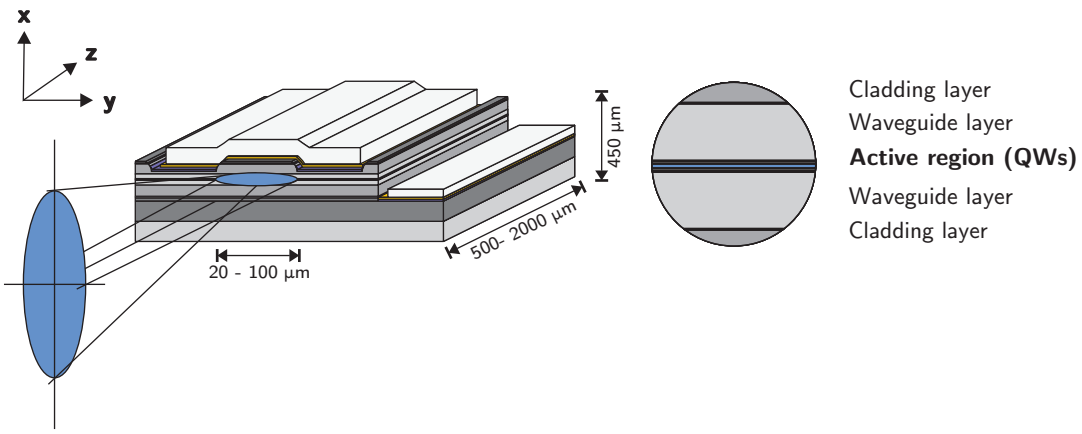


Figure 2.4: Schematic of broad area laser diode. The circle represents a magnification of the active region.

In order to fabricate broad area laser diodes (BA-LD), as outlined in Fig. 2.4, the wafers are processed as follows: First, the Mg-doping is activated through rapid thermal annealing. Next, the fabrication of the p-contacts follows in three steps: Pd/Au metalization of the whole surface, lithography and removal of the metal in the non-resist-covered areas (through sputtering or wet-chemical etching). Afterwards, the photo-resist is stripped and the contacts are annealed. Thick Ti/Au layers work as contact reinforcement and are processed as above (lithography, metalization, lifting).

Once the p-contacts are ready, the surface of the sample is locally etched to reach the n-conductive layers. This is done through plasma-etching with chlorine of the silicon nitride (or resist) mask. Finally, again with lift-off, the n-contacts are deposited in the etched areas. The laser facets are produced accordingly to the optically pumpable structures. The contact stripe width and cavity length of the gain guided laser diodes are between 10-40 and 800-1500 $\mu$m, respectively.

The BA-LDs are characterized by measuring the P-U-I characteristics in pulsed operation mode. The pulse length and repetition rate is 300 ns and 1 kHz, respectively. The emitted light is detected through a micro-lens using a gallium phosphide photo diode and CCD camera in order to determine the optical output power and the emission spectra, respectively.

## 2.4 Device simulation

Beside the growth and characterization of laser diode structures several device simulation tools are used in order to explain the measurements or predict the influence of heterostructure layout variations. With the quasi 2D semiconductor laser simulation program by H.Wenzel [50] (QIP) the internal field, the band structure and the oscillator strengths of the optical transitions of InGaN quantum well structures can be computed. The simulation is based on a self-consistent solution of the Poisson equation and an eight-band k·p Schrödinger equation. Charges due to polarisation fields, doping and free carriers are also considered.

The software SILENSe [51] provides simulations of band diagrams and spectra of nitride based LEDs and LDs. Additionally to QIP, the software includes a carrier transport model and can consider several nitrite-specific effects like high density of threading dislocations and Auger recombination. Complete device simulations are also done by the LASTIP [52] simulation tool, which allows the calculation of the operation of semiconductor lasers in two dimensions.

# 3

# Investigation of In incorporation in GaN

This chapter focuses on the description of the MOVPE growth and characterization of InGaN bulk layers in order to understand the In incorporation in GaN as well as InGaN crystal perfection deterioration mechanisms. Since an emission in the violet-blue wavelength region requires In mole fractions between 0.08 and 0.16 in the quantum wells of the emitters, $In_{0.10}Ga_{0.90}N$ layers are grown on sapphire based GaN substrates. By comparing the In mole fraction in 15 and 120 nm thick InGaN layer the vertical In mole fraction distribution and the influence of the layer thickness on the In incorporation are revealed. Aspects of the In incorporation mechanism are explained by comparing the In incorporation in differently oriented GaN . The findings of this chapter are the basis for the explanation of the investigated crystal perfection deterioration in MQW structures and LD heterostructures.

## 3.1 Sample and growth conditions variation

Two 15 and 120 nm thick nominally $In_{0.10}Ga_{0.90}N$ single layer were deposited on (0001) oriented GaN templates by solely varying the InGaN growth times between 5 and 50 min. The sample structure is similar to type a) in Fig. 2.1 and the set is denoted as $A_{\mathrm{d}}^{\mathrm{InGaN}}$. A second set ($B_{\tilde{\mathrm{n}}}^{\mathrm{InGaN}}$), consisting of three 120 nm thick InGaN layer grown on (0001), $(2\overline{1}\overline{1}2)$ and $(2\overline{1}\overline{1}0)$ oriented GaN templates, is prepared. (0001), non-polar m-plane $\parallel$ $(10\bar{1}0)$ and semi-polar r-plane $\parallel$ $(1\bar{1}02)$ oriented sapphire were used as substrates. Both sets were grown using the Aix200-HT reactor applying identical growth conditions, e.g. $T_{\mathrm{proc}}$=730 °C , reactor pressure ($p_{\mathrm{reactor}}$) = 200 mbar and molar fraction of indium in the gas phase ($x_{\mathrm{vapor}}^{\mathrm{In}}$) $\sim$ 0.35. The samples were investigated by HR-XRD, SEM, AFM, and LT-CL.

## 3.2 Determination of the structural properties

### 3.2.1 HR-XRD measurements

Due to the wider lattice constant of InN in comparison to GaN, InGaN is compressively strained when deposited on GaN. If the compression of the in-plane lattice constant ($a_{\parallel}$) of the InGaN results only in a strain of the out-of-plane lattice constant ($a_{\perp}$) the InGaN layer is called pseudomorphic. When the stress, correlated with the strain of the layer, exceeds a certain value the $a_{\parallel}$ of the InGaN is also strained. The ratio

of $a_{\parallel}$ of InGaN on GaN and intrinsic $a_{\parallel}$ of InGaN under no stress defines the layer relaxation (R). R ranges from R=0 for pseudomorphic material to R=1 for fully relaxed material.

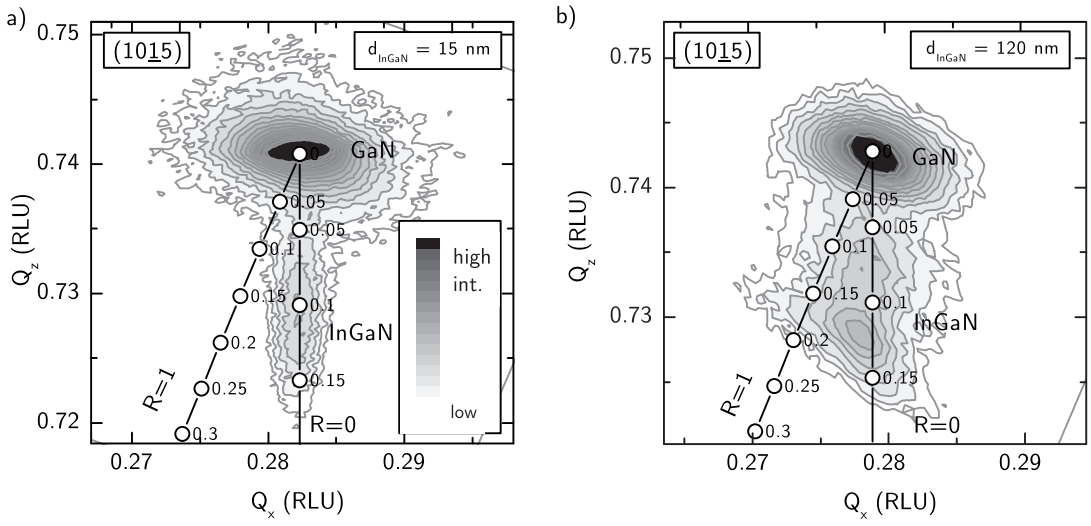


Figure 3.1: RSM around the $(10\bar{1}5)$ reflection of sample set $A_{\mathrm{d}}^{\mathrm{InGaN}}$. The InGaN layers are deposited using identical growth conditions but different deposition times. The corresponding InGaN layer thicknesses are 150 nm (a) and 120 nm (b), respectively. The open circles represent the $x_{\mathrm{solid}}^{\mathrm{In}}$ of pseudomorphic (R=0) or of relaxed (R=1) InGaN, respectively.

Knowing the strain of a InGaN layer $x_{\mathrm{solid}}^{\mathrm{In}}$ and R can be calculated by taking into account the intrinsic lattice constants and the elastic properties of the materials. In order to determine $a_{\parallel}$ and $a_{\perp}$ HR-XRD RSMs were conducted on set $A_{\mathrm{d}}^{\mathrm{InGaN}}$. Fig. 3.1 shows the RSM around the $(10\bar{1}5)$ reflection for the 15 nm (a) and the 120 nm (b) thick InGaN layers. Clearly, the GaN layer peaks with the highest intensity and the InGaN layer peaks with a lower intensity, corresponding to a lower layer thickness, can be distinguished. The analysis of the peak positions allows the calculation of $a_{\perp}$ and $a_{\parallel}$ of the GaN and InGaN layer and thus the In mole fraction in the solid in the samples according to Fewster [53]. Superimposed to the color plot, the calculated peak positions of pseudomorphic (R=0) and fully relaxed InGaN (R=1) with different In mole fraction in the solid are shown.

First the RSM of the 15 nm thick InGaN layer (see Fig. 3.1 a) is discussed: The InGaN layer peak is shifted towards smaller values for $Q_{\mathrm{z}}$ with respect to the GaN layer peak but exhibits no shift in $Q_{\mathrm{x}}$ direction. The identical $Q_{\mathrm{x}}$ corresponds to an identical $a_{\parallel}$ of the InGaN and GaN and therefore indicates pseudomorphic growth. The smaller value for $Q_{\mathrm{z}}$ correspond to a strained $a_{\perp}$ correlated with an In mole fraction of around 0.09. The wide extension of the InGaN layer peak in $Q_{\mathrm{z}}$-direction is due to scattering on a crystalline object that is restricted in one dimension (z) and extended in the other two (x,z) [54].

By comparing the In mole fraction in the solid of the 15 and 120 nm thick InGaN layer (see Fig. 3.1 b) the variation of the In incorporation as the layer thickness increases is revealed. The intensity peak of the 120 nm thick InGaN layer is shifted

towards smaller values for $Q_x$ and $Q_z$ with respect to the intensity peak of the 15 nm thick InGaN layer. The smaller value for $Q_z$ corresponds to an increase of the average In mole fraction in the solid to 0.12 as the layer thickness increases. The shift of the InGaN peak towards smaller values for $Q_x$ is due to a relaxation of R=0.3 of the InGaN $a_{\parallel}$ with respect to those of the GaN layer underneath.

### 3.2.2 SIMS measurements

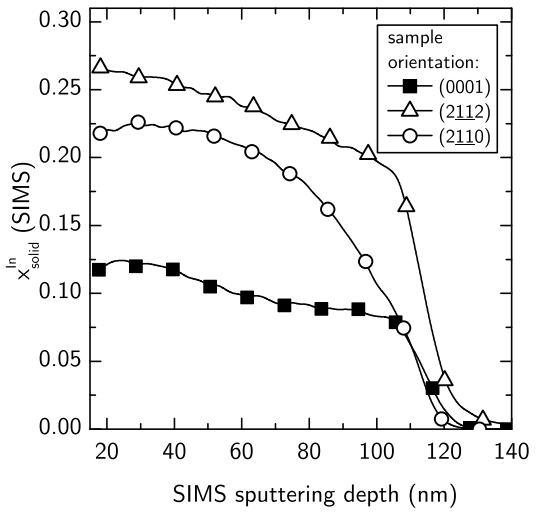


Figure 3.2: SIMS measurement on the nominally 120 nm thick InGaN layers of set $A_d^{InGaN}$ and $B_{\tilde{n}}^{InGaN}$. The atomic In concentration is estimated by comparison of the measured CsIn concentration with the signal strength of calibration samples.

In order to directly examine the variation of the In mole fraction in growth direction, secondary ion mass spectroscopy (SIMS) was conducted on the 120 nm thick InGaN samples. The solid black squares in Fig. 3.2 represent the In mole fraction profile of the 120 nm thick InGaN layer of set $A_d^{InGaN}$. The profile exhibits a distinct increase of the atomic In concentration as the layer thickness exceeds 60 nm. The increase of the In mole fraction in the solid can be explained by a reduction of the lattice mismatch of $a_{\parallel}$ ($\epsilon_{xx}$) as the relaxation sets in [55]. Using an approach proposed by People and Bean [56], the critical layer thickness for pseudomorphic growth ($h_{crit}$) of $In_{0.09}Ga_{0.91}N$ is calculated to $\sim$ 65 nm. While the cause of the layer relaxation is the high $\epsilon_{xx} \simeq$ -0.01 in the early stage of the InGaN layer growth, the relaxation mechanism is not fully understood. In general, the strain release is related to the onset of plastic relaxation, e. g. the formation of dislocations above $h_{crit}$ [56, 57]. In the arsenide material system a dislocation glides from the free surface to the heterointerface. Since this has not been observed in the InGaN layer with different relaxation states [58], the different relaxation mechanisms are investigated and discussed later on in this chapter.

### 3.2.3 Spectrally resolved CL measurements

In order to correlate material and luminescence properties, necessary for the characterization of the emitter later on, spectrally resolved LT-CL measurements were conducted on sample set $A_d^{InGaN}$. Therefore, the samples were cooled down to 80 K and investigated using the Oxford LT-CL system attached to the JEOL 840A SEM.

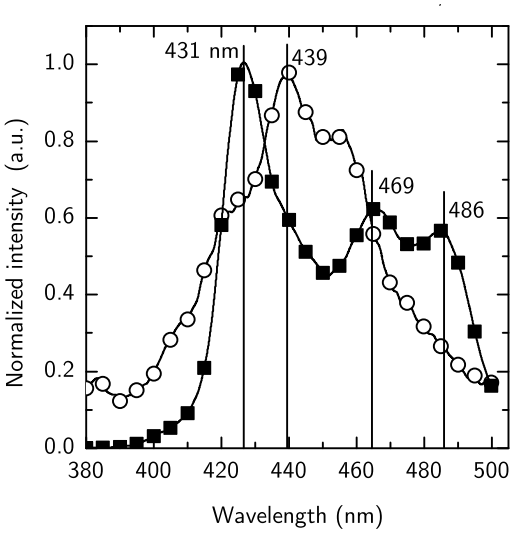


Figure 3.3: Normalized LT-CL spectra of the sample of set $A_{\mathrm{d}}^{\mathrm{InGaN}}$ with 15 (open circles) or 120 nm (squares) thick InGaN layer. The spectra were derived by spatial integration over a $20\times20\,\mu$m area, the acceleration voltage was 12 kV, the electron current 10 nA.

Fig. 3.3 shows the LT-CL spectra of the samples of set $A_{\mathrm{d}}^{\mathrm{InGaN}}$. The spectrum of the 15 nm thick InGaN exhibits a single peak at 439 nm with a FWHM of $\sim$ 50 nm. The spectrum is superimposed by Fabry-Perot oscillations, which are identified by their periodicity. On the other hand the spectrum of the 120 nm thick InGaN layer features multiple peaks at 431, 469 and 486 nm, associated with luminescence from regions with a different $x_{\mathrm{solid}}^{\mathrm{In}}$ or R. The spectral widening of the band edge luminescence of relaxed InGaN layers was also observed by Pereira et al. [59]. According to their work, the luminescence with different energies originates from relaxed and coherently InGaN regions.

In order to quantitatively correlate the emission wavelengths with the determined material properties, the transition energies of bulk InGaN is calculated. According to Pereira et al. [60] the band gap energy of fully relaxed material ($E_{\mathrm{g}}^{\mathrm{rlx}}$) in relation to the band gap energy of fully strained material ($E_{\mathrm{g}}^{\mathrm{abs}}$) for InGaN with $x_{\mathrm{solid}}^{\mathrm{In}} < 0.3$ is described as follows:

$$E_g^{\mathrm{rlx}}(\mathrm{InGaN})\,[eV] \simeq E_g^{\mathrm{abs}} - \epsilon_{\mathrm{zz}}^{\mathrm{InGaN}} \times \frac{dE_g^{\mathrm{GaN}}}{d\epsilon_{\mathrm{zz}}} \tag{3.1}$$

Identical to our experiment Pereira et al. [60] investigated the luminescence of 75 to 500 nm thick InGaN layer deposited on GaN with $x_{\mathrm{solid}}^{\mathrm{In}}$ <0.25. The best fit to their experimental data reveals $E_g^{\mathrm{rlx}}(\mathrm{InGaN})\,[eV] \simeq 3.39 - 3.57\,x_{solid}^{In}$. The $x_{\mathrm{solid}}^{\mathrm{In}}$ dependency of $E_{\mathrm{g}}^{\mathrm{rlx}}$ can be used to calculate the actual band gap energies of the coherent and relaxed material. A linear interpolation of the gap deformation potential $\frac{dE_g}{d\epsilon_{\mathrm{zz}}}$ of GaN [61] and InGaN [62] is used. Applying the formula 3.1 the nominal peak wavelengths of set $A_{\mathrm{d}}^{\mathrm{InGaN}}$ are calculated to 421 nm ($x_{\mathrm{solid}}^{\mathrm{In}}$ =0.09, R=0) and 436 nm ($x_{\mathrm{solid}}^{\mathrm{In}}$ =0.12, R=0.3) for the 15 and 120 nm thick InGaN layer, respectively.

First, the red-shift of 10 nm between the measured LT-CL wavelengths and the calculated wavelength for the 15 nm thick InGaN layer is discussed: Beside the inaccuracy of the HR-XRD measurement, the red-shift and the wide FWHM $\sim$ 50 nm of the LT-CL can be explained by a spatial separation of the electrons and holes in the presence of an electrical field, which is not included in the calculations. Such

a field is caused by variations of the piezoelectric and spontaneous polarization in growth direction (see also Sec. 4.3) as well as charged surface states. The charges are located at the GaN / InGaN interface and surface of the sample, respectively. The electrical field strengths and thus the red-shift increases as the distance between the sheet charges decreases. An influence of the intrinsic fields on the luminescence is therefore more likely for thin InGaN layer.

In the case of the 120 nm thick InGaN layer the calculated wavelength based on the HR-XRD and SIMS measurements (Fig. 3.1 and 3.2) is in good agreement with the LT-CL luminescence wavelength. The luminescence with the highest intensity (see Fig. 3.3) originates from the partially relaxed bulk material with $x^{\mathrm{In}}_{\mathrm{solid}}$ =0.12 (R=0.3). The 469 or 486 nm luminescence originate from material with an In mole fraction in the solid of 0.16 and 0.18 (assuming R=0.3) or 0.21 and 0.23 (R=1) according to Equ. 3.1. Since the quantitative HR-XRD and SIMS measurements represent only the average $x^{\mathrm{In}}_{\mathrm{solid}}$ of a certain volume, deviations of the In mole fraction within a small volume are not resolved. Furthermore, efficient recombination could be observed from these sections with a small volume and a low band gap because the carriers relax into the potential minima and recombine there at the LT-CL measurement temperature of 80 K. In order to localize the material with the lower band gap or respectively increased In mole fraction in the solid spatially resolved LT-CL measurements are conducted and discussed in the next section.

## 3.3 Investigation of the spatial uniformity of the material properties

### 3.3.1 Spatially resolved CL measurements

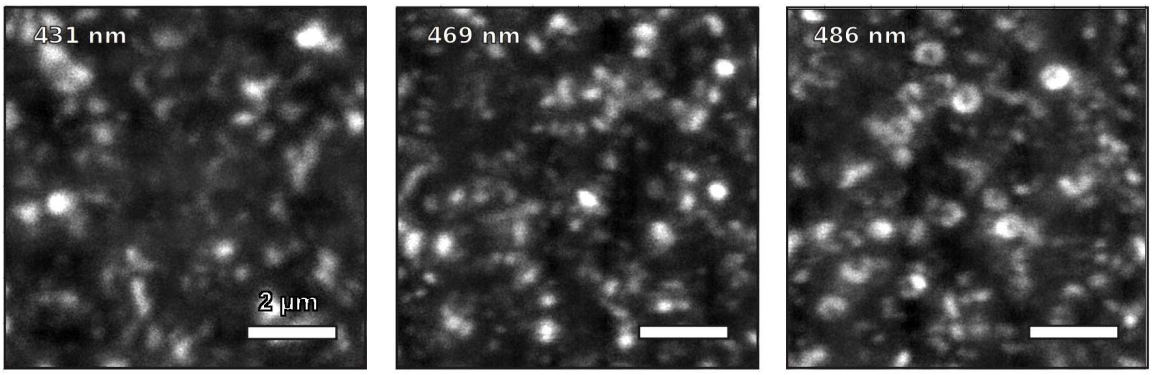


Figure 3.4: Monochromatic LT-CL images of the sample of set $A^{\mathrm{InGaN}}_{\mathrm{d}}$ with the 120 nm thick InGaN layer measured at 80 K. The detection wavelength is noted in the upper left corner of each picture. The acceleration voltage and current was 12 kV and 0.5 nA, respectively.

Using the Oxford LT-CL system spatially resolved LT-CL measurements were conducted at 80 K. Fig. 3.4 shows the monochromatic LT-CL images of the 120 nm thick

InGaN layer of set $A_{\mathrm{d}}^{\mathrm{InGaN}}$. The local brightness corresponds to the intensity of the emission with a distinct wavelength. The wavelengths are noted in the upper left corner of each image and are identical with the intensity peaks in the LT-CL spectrum in Fig. 3.3. Clearly, the 431, 469 and 486 nm luminescence originates from different circular shaped areas with a diameters between 0.2 and 0.5 $\mu$m.

A possible explanation for lateral variation of the luminescence wavelength are spatial In mole fraction non-uniformities in the solid. Such non-uniformities are associated with several growth irregularities. Wu et al. and Kawaguchi et al. [63, 64] report on a higher In incorporation at the pyramid sidewalls of v-shaped pits [65] in comparison to (0001) GaN. Although this would explain the locally increased In mole fraction, the area of the defect sidewalls had to be rather large with respect to the defect-free surface. Otherwise the emission from the defect-free material (nominally 436 nm) would dominate the spectrum. In order to examine the surface of the samples the morphology of set $A_{\mathrm{d}}^{\mathrm{InGaN}}$ was investigated by SEM and AFM.

### 3.3.2 AFM and SEM measurements

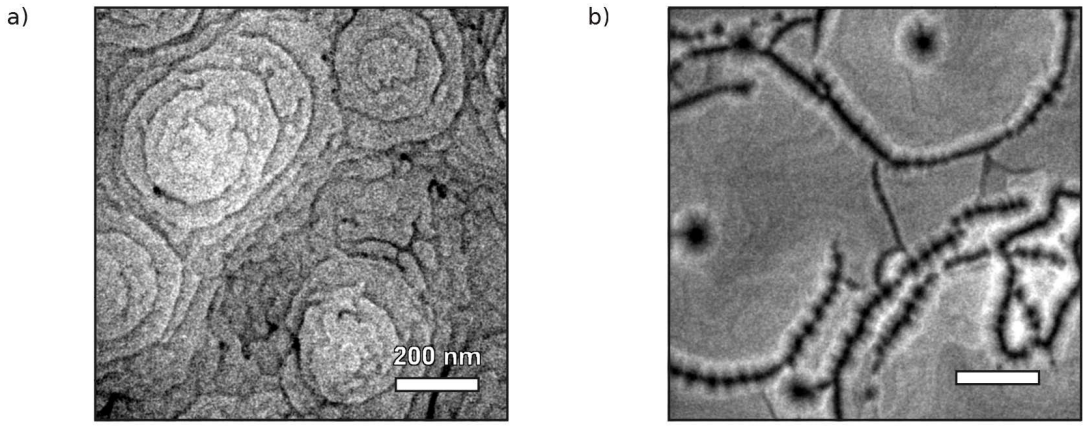


Figure 3.5: SEM images of the samples of set $A_{\mathrm{d}}^{\mathrm{InGaN}}$ with 15 (a) or 120 nm (b) thickness, respectively. The average structure height is 10 nm and 39 nm for the 15 and 120 nm thick InGaN layer as has been revealed by AFM. The acceleration voltage was 10 kV.

Fig. 3.5 shows the SEM morphology contrast for the samples of set $A_{\mathrm{d}}^{\mathrm{InGaN}}$. Both samples exhibit circular three-dimensional (3D) structures. Additionally, v-shaped defects can be seen on the surface of the 120 nm thick InGaN layer. The defects are circularly aligned with a single defect located in the center. The diameter of the islands increases from around 0.8 $\mu$m to 1.5 $\mu$m as the InGaN layer thickness increases from 15 to 120 nm. AFM measurements ($10\times10$ $\mu$m area: not shown here) reveal a average height of 10 nm ($r_{\mathrm{rms}}$=2.8 nm) and 39 nm ($r_{\mathrm{rms}}$=14 nm) for the 15 and 120 nm thick InGaN layer, respectively.

Assuming a flat surface at the start (shown later on) and an average spiral height of the 15 nm thick InGaN layer the transition from 2D to 3D growth starts after a few mono layers (ML)s. The alignment of the islands around v-shaped defects suggests

a promotion of 3D growth by the defects. V-shaped defects are generated from pure screw or mixed type threading dislocations TDs [65]. Their Burgers vector ($\vec{b}$) has a component normal to the surface that represents a non-vanishing edge. Depending on the growth regime 3D structures can evolve from such an edge. The BFC model [66] distinguishes the growth regimes by the ratio of the diffusion length of an ad-atom ($x_s$) and the distance of the growth steps (l). In a regime of local supersaturation ($x_s \ll l$) only adatoms which are deposited close to a step or edge are incorporated. As a consequence the steps wind up in spirals and considerably enhance the growth rate around the TDs [66, 19]. Local supersaturation is promoted by the InGaN growth conditions, e.g. by the low growth temperatures and the fast In desorption. Due to both effects an atom that hits the growth surface far from an edge more likely desorbs than reaching an incorporation site.

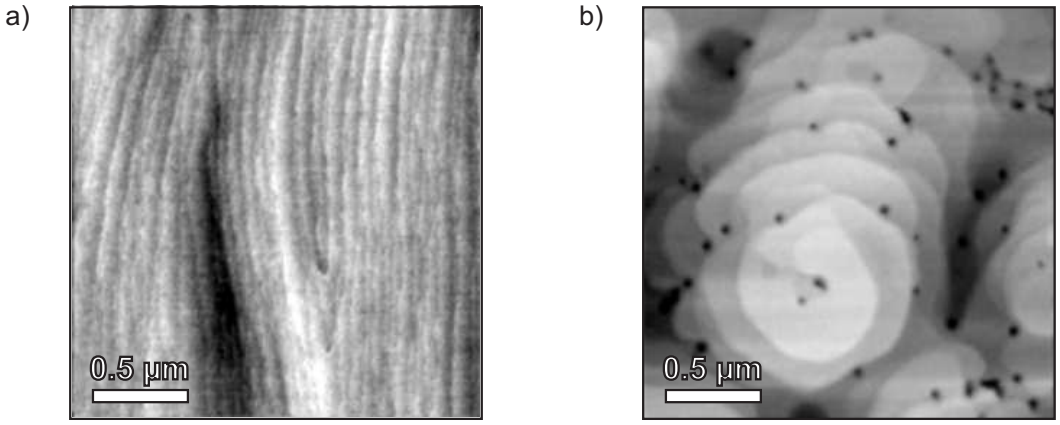


Figure 3.6: a) AFM surface morphology of a GaN template (sample $A^{\mathrm{GaN}}_{\mathrm{templ.}}$). The height axis corresponds to 2 nm. b) AFM surface morphology of a 100 nm thick InGaN layer with $x^{\mathrm{In}}_{\mathrm{solid}} = 0.02$ (sample $A^{\mathrm{InGaN}}_{\mathrm{spiral}}$) showing spiral growth. The height axis corresponds to 12 nm.

To get a better impression of the surface morphology a 100 nm thick InGaN layer with an In mole fraction of 0.02 was deposited on a GaN template (sample $A^{\mathrm{InGaN}}_{\mathrm{spiral}}$). The In mole fraction in the solid was reduced with respect to set $A^{\mathrm{InGaN}}_{\mathrm{d}}$ in order to enable AFM measurements that resolve the growth edges. Fig. 3.6 shows a typical GaN surface morphology of an 1.2 $\mu$m GaN template (a) in comparison to the InGaN layer (b). Clearly, the alignment of the growth fronts changed from parallel on the GaN template to circular on the $In_{0.02}Ga_{0.98}N$ layer. The growth steps curl around a threading dislocation and form a growth spiral. As a consequence the $r_{\mathrm{rms}}$ roughness increases to 2 nm for InGaN in comparison to 0.4 nm for the GaN template.

## 3.4 Investigation of defects and material deterioration mechanisms

Surface roughening and spatial variations of the luminescence or respectively the In mole fraction in the solid deteriorate the crystal perfection of the InGaN layer. In

order to clarify the material deterioration mechanism the origin of the defect and their influence on the spatial distribution of the In in the layer is discussed in the following.

### 3.4.1 Origin of defects

The TDs originate from the hetero-interface in the sapphire-based GaN templates. Due to the large lattice mismatch between substrate and the GaN epi-layer mosaic structures are formed, e.g. tilted and twisted small crystallites [67, 68, 69]. According to Metzger et al. [70] the tilt of (0001) sapphire based GaN layers gives rise to screw TDs with $\vec{b}$=[0001], while the twist is connected to edge TDs with $\vec{b}=\frac{1}{3}[11\bar{2}0]$.

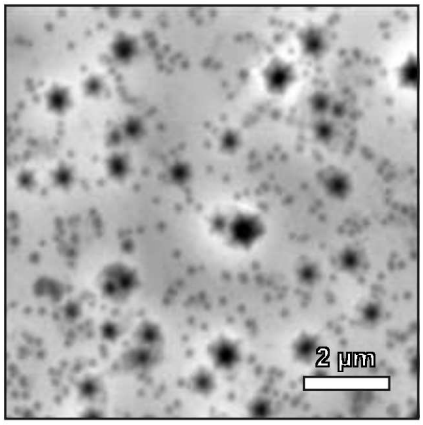


Figure 3.7: SEM image of a sapphire based GaN template ($A'^{\mathrm{GaN}}_{\mathrm{templ.}}$). The sample was treated with 450°C hot KOH for 15 min [71] to selectively etch the dislocations. The etch pits with the different diameters are associated with edge and screw type TDs.

In order to reveal the TD density of the used GaN templates, defect selective etching [71] was conducted on a $A'^{\mathrm{GaN}}_{\mathrm{templ.}}$. Fig. 3.7 shows a SEM-picture of the etched surface. The threading points of the dislocations are decorated because of the etch rate anisotropy. The density of etch pits is around $5\times10^7$ cm$^2$ (wide diameter) and $4.6\times10^8$ cm$^2$ (small diameter). Their density (mean free path: 0.4 - 1 $\mu$m) correlates good with the density of spirals found in Fig. 3.5 indicating the pinning of the growth edges by the threading points of the screw type dislocations.

### 3.4.2 Interplay between threading dislocations and spatial In mole fraction variations

The LT-CL measurements suggest strong spatial variations of the In mole fraction in the 120 nm thick InGaN layer. Directly correlating the different wavelengths ($\lambda_{\mathrm{CL}}$) found in the sample the In mole fraction in the solid ranges from $x^{\mathrm{In}}_{\mathrm{solid}} = 0.12$ (R=0,$\lambda_{\mathrm{CL}}$=431 nm) to 0.23 (R=1, $\lambda_{\mathrm{CL}}$=486 nm). Different to the observations of Pereira et al. [59], who correlated the multi-peak luminescence with the vertical gradient of the In mole fraction in the solid in their samples, the LT-CL measurements suggest that the multi-peak luminescence is due to lateral In mole fraction variations correlated with the 3D surface structure. According to [72] the increased In mole fraction at the spiral side surfaces can be qualitatively explained when considering the elastic energy as well as the surface energy of the different surfaces. Due to the

high In-N bond length the incorporation of an In atom into GaN increases the energy of the system. As a consequence, the In incorporates at sites where the total energy change has a minimum.

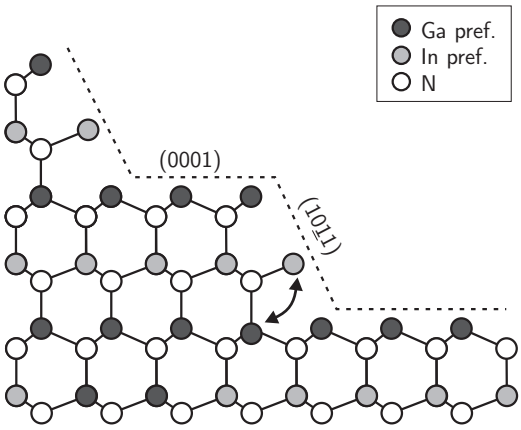


Figure 3.8: Stick and ball model of a surface step on a (0001) GaN after [73]. The arrow indicates the interchange of In atoms between bulk and lower coordinated surface sites.

On (0001) GaN the surface steps form (10$\bar{1}$0) facets (see Fig. 3.8). Calculations [73] show that the surfaces energy of this facet is reduced by 15 meV/Å with respect to the (0001) surface (125 meV/Å) due to the different bond configuration. As a consequence of the long In-N bond length it is energetically beneficial for the In atom to incorporate at sites with a low surface energy. Furthermore, the In atoms segregate from the bulk to sites with lower bond coordination on the surface. Therefore, the In mole fraction locally increases in the topmost layer. This can explain the experimentally determined red-shift of the luminescence with respect to the expected wavelength of the InGaN bulk material.

Besides a different atomic surface and bond configuration the stress differs on the different orientations due to the anisotropy of the elasticity in the GaN material system. In order to understand how the orientation of the incorporation sites affects the In incorporation, the elastic energy is calculated for several surface orientations.

Fig. 3.9 displays the bond configuration of the hexagonal unit cell and the surface orientation of the samples of set $B_{\tilde{n}}^{\mathrm{InGaN}}$. To understand the orientation- or respectively $\theta$-dependency of the In incorporation the strain energy ($W(\varphi,\theta)$) is calculated. $W(\varphi,\theta)$ represents the energy that is necessary to strain the cells [74] e.g. by the incorporation of In.

$$W(\varphi,\theta) = \sum_{\mathrm{i,j}} \left( \left(c_{\mathrm{ij}}(\epsilon(\varphi,\theta))\right)_i \left(\epsilon(\varphi,\theta)\right) \right)_j \tag{3.2}$$

Transforming Hooke's law into cylindrical coordinates allows to calculate the independent $\epsilon_{\mathrm{ij}}$ as a function of the cylindrical angles $\varphi$ and $\theta$ according to Romanov et al. [75]. The $\epsilon_{\mathrm{ij}}$ as a function of the cylindrical angle $\theta$ are plotted in Fig. 3.10 (top).

Using the material parameters from [76] $W(\varphi,\theta)$ is calculated as a function of the polar angle $\theta$ (see Fig. 3.10 bottom). Clearly, $W(\varphi,\theta)$ exhibits a minimum for $\theta$ around 60° close to the angle of the (10$\bar{1}$0) growth edges of around 61°.

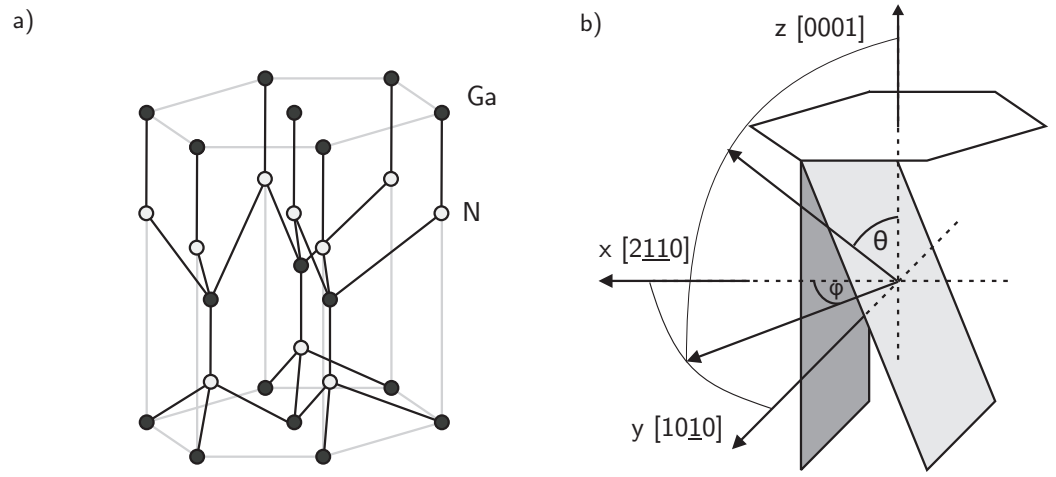


Figure 3.9: a) Hexagonal unit cell of GaN. The solid and open circles represent the position of the Ga or N atoms, respectively. b) Schematic of the (0001) (white), $(2\overline{1}\overline{1}2)$ (light grey) and $(2\overline{1}\overline{1}0)$ (grey) oriented surfaces of sample set $B_{\tilde{n}}^{\mathrm{InGaN}}$. The corresponding angles in spherical coordinates are $\theta = 0$, 58.4 and 90 ° and $\varphi$=0.

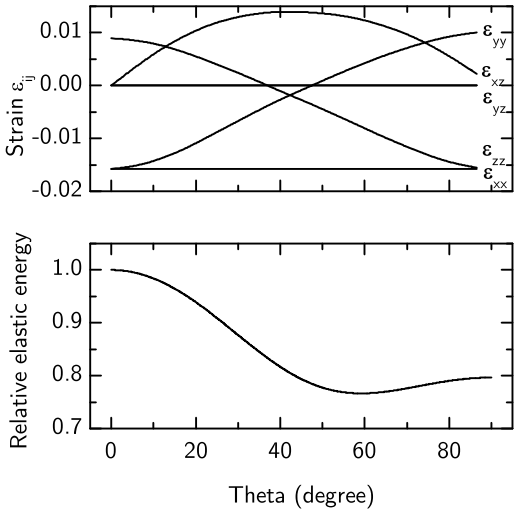


Figure 3.10: $\theta$-dependency of the elastic strains (top) and $W(\varphi, \theta)$ (bottom) for InGaN with $x_{\mathrm{solid}}^{\mathrm{In}} = 0.15$. $W(\varphi, \theta)$ is displayed relatively to $W(\varphi, \theta)$ for $\theta = 0°$. The angle $\varphi$ is 0.

In order to prove the higher In incorporation on a surface with $\theta > 0$, the In mole fraction in the solid of differently oriented InGaN layers was analyzed. The corresponding $\theta$ angles between the (0001), semi-polar plane ∥ $(2\overline{1}\overline{1}2)$ or non-polar a-plane ∥ $(2\overline{1}\overline{1}0)$ surfaces in set $B_{\tilde{n}}^{\mathrm{InGaN}}$ and the (0001) surface are 0, 58 and 90° (see Fig. 3.9 b)).

Fig. 3.2 displays the atomic In concentration profiles of set $B_{\tilde{n}}^{\mathrm{InGaN}}$ derived by SIMS. The slopes of the profiles show a slight increase of the measured atomic In concentration with increasing layer thickness but a distinct decrease after 100 nm, pointing to an identical InGaN growth rate. Hence, growth rate related effects on the In mole fraction in the solid [77] can be neglected. In comparison to a maximum In mole fraction in the solid of around 0.12 on the (0001) oriented sample, $x_{\mathrm{solid}}^{\mathrm{In}}$ is remarkably increased to 0.2 and 0.25 on the $(2\overline{1}\overline{1}0)$ and $(2\overline{1}\overline{1}2)$ oriented surface, respectively. The experimentally determined In mole fractions in the solid qualitatively correspond to

the $W(\varphi,\theta)$ calculated above; the surface orientation in set $B_{\tilde{n}}^{\mathrm{InGaN}}$ with the lowest $W(\varphi,\theta)$ shows also the highest In incorporation.

Quantitatively, the In mole fraction of 0.25, determined for the $(2\bar{1}\bar{1}2)$ oriented sample, corresponds well to the longest LT-CL wavelength measured for the (0001) oriented sample of set $A_{\mathrm{d}}^{\mathrm{InGaN}}$ if assuming R=1. The finding suggests that the long wavelength luminescence originates from such facets, that exhibit a higher In incorporation with respect to (0001) surfaces. Beside the micro-facets of the v-shaped defects the growth edges exhibit this distinct angle correlated with a minimum of the elastic energy.

The qualitative estimation and the quantitative determination of the In incorporation on the different surfaces support the high affinity of In to incorporation at $(10\bar{1}0)$ facets with a lower coordination and a lower elastic energy of the bonds. Taking the aspect ratio of the spirals into account, the step spacings at the sidewall can be calculated to 52 Å(15 nm thick InGaN ) or 9 Å(120 nm), respectively. Typical step spacing for 2D layer by growth of InGaN and GaN are between 40 nm [78] and 60 nm - 100 nm [79, 80]. Due to the high step density the total number of preferred In incorporation sites is higher at the spiral sidewalls explaining the long wavelength emission from this regions.

## 3.5 Summary and Conclusion

15 and 120 nm thick InGaN single layers were analyzed in order to investigate the In incorporation mechanism into the GaN. It was shown that the In mole fraction in the solid increases with increasing layer thickness after lattice mismatch relaxation above a critical thickness sets in. A second crystal quality deterioration mechanism, beside the variation of the In mole fraction in growth direction, is the strong spatial non-uniformity of the In incorporation. The In mole fraction in the solid is locally increased at the sidewalls of 3D spirals on the growth surface. The spirals evolve due to pinning of the edges at threading dislocations and are promoted by the InGaN growth regime, e.g. the high desorption rate of ad-atoms and the low velocity of the species.

While layer thickness non-uniformities are explained straightforward by 3D growth, the spatially non-uniform In incorporation in the top most layer was investigated more closely. It turned out that due to the long InN bond length with respect to GaN the In preferably incorporates at sites with lower bond coordination and higher bond elasticity. Such sites are the sidewalls of the 3D spirals, where winded growth edges provide a high density of $(10\bar{1}1)$ surfaces. The increase of In incorporation as the elastic energy of the surface decreases was qualitatively proved for the InGaN deposition on differently oriented GaN.

In conclusion, the investigation of the InGaN layer growth enables the understanding of the In incorporation as well as fundamental InGaN material deterioration mechanisms, e.g. lattice mismatch relaxation, spatial layer thickness and In mole fraction non-uniformities. The findings will be used in the next chapters in order to

increase the material quality of InGaN quantum well and barrier layers.

# 4

# Growth and characterization of InGaN quantum structures

The optical characteristics of (Al,In,Ga)N LDs are primarily determined by the structural properties as well as the crystal perfection of the InGaN layer in the active region. In order to control the device characteristics the influence of the MQW layout, e.g. well and barrier dimensions, on the luminescence properties and the crystal perfection of the active region are revealed.

Beside the material quality degradation mechanisms discussed in chapter 3 the deterioration of the crystal perfection of quantum structures due to segregation effects [81, 82] are additionally analyzed. When growing on polar orientations strong intrinsic fields occur in the quantum structures that reduce the luminescence efficiency. Therefore the effect of the intrinsic field in the quantum structures on the optical properties such as radiative recombination [83, 84], internal quantum efficiency [85, 86] is discussed.

## 4.1 Sample and growth conditions variation

| Set | QW no. | $T_G$ (°C) | $d_{cap}$ (nm) | $t_{QW}$ (s) | $d_{well}$ (nm) | $d_{bar}$ (nm) | $x^{In}_{solid}$ | 10 K-$\lambda_{PL}$ (nm) |
|---|---|---|---|---|---|---|---|---|
| $A^{d_{bar}}$ | 5 | 775 | 0 | 60 | 2.1 | 7.3 | | |
| | | | | | | 10.0 | | |
| $B^{d_{QW}}$ | 4 | 775 | 40 | 40 | 1.4 | 7.3 | 0.13 | 444 |
| | | | | 60 | 2.1 | | 0.15 | 470 |
| | | | | 80 | 2.8 | | 0.17 | 491 |
| | | | | 100 | 3.8 | | 0.17 | 513 |
| $C^{d_{QW}}$ | 3 | 750 | 10 | 30 | 1.1 | 7.3 | 0.13 | 422 |
| | | | | 45 | 1.7 | | 0.14 | 439 |
| | | | | 60 | 2.1 | | 0.16 | 466 |

Table 4.1: Varied growth parameters and the structural properties of the samples of set $A^{d_{bar}}$, $B^{d_{QW}}$ and $C^{d_{QW}}$ derived from HR-XRR and HR-XRD measurements assuming a rectangular In mole fraction profile in the QWs. $d_{cap}$, $d_{well}$ and $d_{bar}$ represent the thicknesses of the cap on top of the active region, the QWs thickness and the barriers thickness. $t_{qw}$ is the QW growth time and $x^{In}_{solid}$ the QW In mole fraction. The remaining growth parameters were identical for all samples. The last column displays the peak luminescence wavelengths determined by PL at 10 K.

Several sets of MQW structures of type b) in Fig. 2.1 were prepared. A first set $A^{\mathrm{dbar}}$ consists of 5-fold InGaN/ GaN MQW structures where only the quantum barrier growth time was varied. Using identical growth conditions, a second set ($B^{\mathrm{dQW}}$) was prepared where only the QW growth times were varied. A third set of MQW structures denoted as set $C^{\mathrm{dQW}}$ with varying QW thickness was produced using the active region growth conditions of set $A^{\mathrm{dbar}}$ and $B^{\mathrm{dQW}}$ but a lower growth temperature for the QWs. In the case of set $C^{\mathrm{dQW}}$ the number of QWs was reduced to three and a 1.2 $\mu$m thick $Al_{0.12}Ga_{0.88}N$/GaN SPSL was included in the sapphire-based GaN template. Further information about the heterostructures can be found in Tab.4.1.

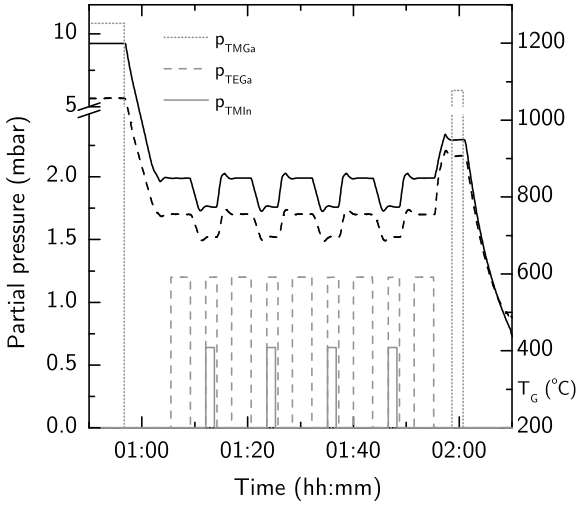


Figure 4.1: Growth scheme showing group III precursor partial pressures and temperatures for the sample with $t_{\mathrm{QW}} = 100\,\mathrm{s}$ of set $B^{\mathrm{dQW}}$. The thick black lines represent the temperatures measured on the backside of the susceptor (solid line) and the front side of the satellite (broken line).

All MQW samples were grown in the Aix2400G3-HT on (0001) oriented sapphire based GaN templates. Besides the noted parameter, identical growth conditions, e.g. $p_{\mathrm{reactor}}$=400 mbar, $x^{\mathrm{In}}_{\mathrm{vapor}}$ =0.35 for quantum well growth, were used. Fig. 4.1 depicts the transients of the growth temperatures and the group III partial pressures for a sample of set $B^{\mathrm{dQW}}$. In all sets the GaN quantum barrier growth temperature was increased by 75 K with respect to the QW growth temperature in order to improve the barrier material quality. In order to protect the QWs two MLs of n.i.d. GaN are deposited before the growth temperature is increased during a growth interruption. A 10 to 40 nm thick GaN capping layer was grown on top of the active region (not in set $A^{\mathrm{dbar}}$) in order to reduce surface effects on the recombination mechanism during PL measurements.

## 4.2 Accurate determination of the QW properties

### 4.2.1 Experimental approach

The structural properties of the sample sets were characterized by HR-XRD on sample set $A^{\mathrm{dbar}}$, $B^{\mathrm{dQW}}$ and $C^{\mathrm{dQW}}$, since the thickness of the layers in the MQW and their composition cannot be determined unambiguously from a single HR-XRD scan [87]. First, the growth rate of the quantum barriers was determined by HR-XRD measurements on sample set $A^{\mathrm{dbar}}$ where only $t_{\mathrm{bar}}$ are varied. The influence of $t_{\mathrm{bar}}$ on the MQW

periodicity can clearly be seen in the $\Omega - 2\Theta$ scans at the (0002) reflection shown in Fig. 4.2. The data can be fitted by making several assumptions. First, the profile of the indium molar fraction is assumed to be rectangular. Although other HR-XRD data will later be used to quantify the non-abruptness of the well/barrier interfaces, a more complicated model for the indium profile is not reasonable here because the peak positions in Fig. 4.2 are only sensitive to the MQW period ($d_{\mathrm{QW}} + d_{\mathrm{bar}}$) and the average indium content of the QWs [87]. Secondly, the growth rate is assumed to be constant. This rate is referred to as the barrier growth rate although it will be shown later on that parts of this nominally binary GaN layer contain In. Since the In content is low, it does not have a significant impact on the rate with which the barrier thickness increases. Additionally, the growth of the barriers takes place in the supply limited regime. Therefore, no time dependence of the rate at a given Ga supply is to be expected.

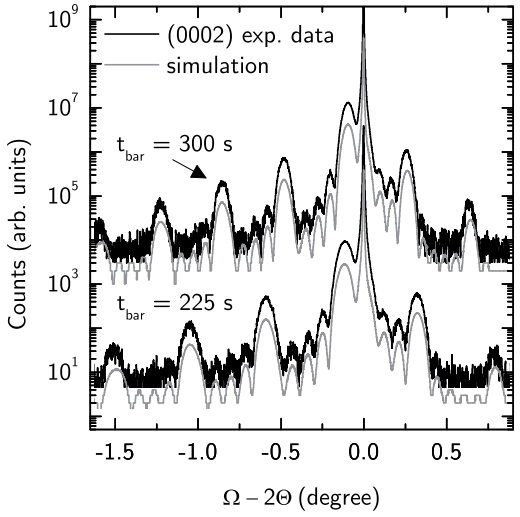


Figure 4.2: HR-XRD $\Omega - 2\Theta$ scans of the (0002) reflection for samples of set $A^{\mathrm{dbar}}$. The grey line represents the simulation of the experimental data (black line).

Next, sample set $B^{\mathrm{dQW}}$ with varied quantum well growth time ($t_{\mathrm{QW}}$) was analyzed. Since the samples are capped with 40 nm n.i.d. GaN the MQW layer peaks of the $\Omega - 2\Theta$ scans are superimposed by the capping layer fringes (see Fig. 4.3). Therefore, HR-XRR was additionally measured on this set. Fig. 4.4 a) depicts the influence of the QW growth time on the HR-XRR patterns of the samples of set $B^{\mathrm{dQW}}$. The black lines correspond to the experimentally determined reflection pattern whereas the grey lines represent their simulations. The reflection pattern features characteristic peaks correlated with the sum $d_{\mathrm{QW}} + d_{\mathrm{bar}}$. Plotting $d_{\mathrm{QW}} + d_{\mathrm{bar}}$ as a function of $t_{\mathrm{QW}}$ reveals a linear dependence as can be seen in Fig. 4.4 b). Regression to $t_{\mathrm{QW}} \rightarrow 0$ yields a MQW period of 7.2 nm i.e. the barrier thickness. From the barrier growth rate, which was derived from sample set $A^{\mathrm{dbar}}$, a barrier width of 7.3 nm is expected. The good agreement of the two values shows that the data evaluation of the sample set $A^{\mathrm{dbar}}$ was correct, particularly the assumed constancy of the barrier growth rate was reasonable. It should be noted that for the linear extrapolation shown in Fig. 4.4 b) the well growth rate needs to be constant. This assumption seems to be justified considering the error bars of the data points. We estimate the uncertainty of the

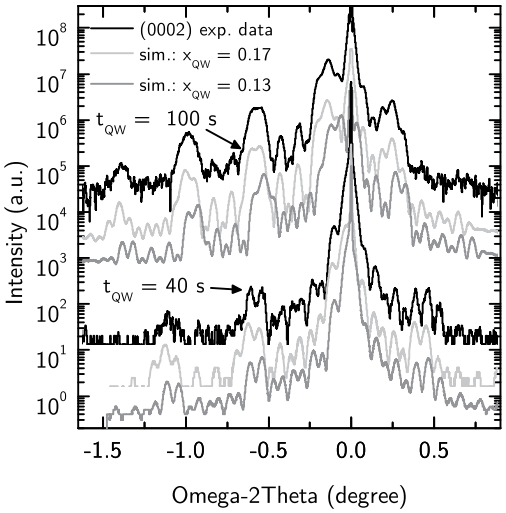


Figure 4.3: $\Omega - 2\Theta$ scans of the (0002) reflection (black line) for the samples with $t_{\mathrm{QW}} = 40$ and 100 s representatively for set $B^{\mathrm{dQW}}$. The thin grey and dark grey line show the simulation of the experimental data assuming abrupt interfaces and $x^{\mathrm{In}}_{\mathrm{solid}} = 0.17$ or $x^{\mathrm{In}}_{\mathrm{solid}} = 0.13$, respectively.

derived barrier width to 0.4 nm if a linear extrapolation is used. The slope of the linear fit in Fig. 4.4 b) corresponds to a QW growth rate of around 130 nm/h (± 5 nm/h). Once again, the growth rate here means the rate of the layer thickness increase during QW growth time.

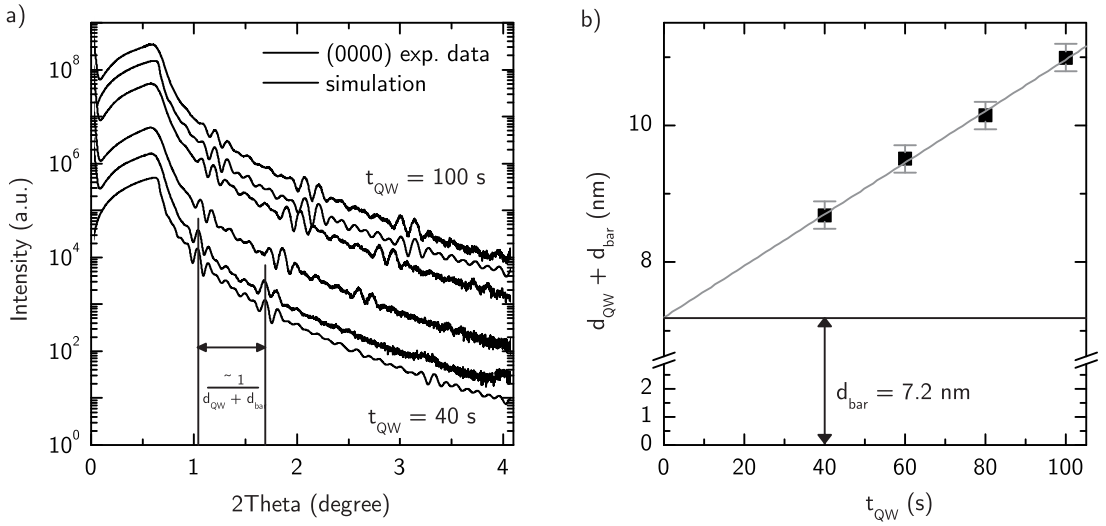


Figure 4.4: a) HR-XRR patterns (black line) for all samples of set $B^{\mathrm{dQW}}$. The thin grey lines represent the simulation of the experimental data for $t_{\mathrm{QW}} = 40$ and 100 s. b) Linear fit of the sum $d_{\mathrm{QW}} + d_{\mathrm{bar}}$ derived from the HR-XRR measurements. The error bars correspond to a $d_{\mathrm{QW}} + d_{\mathrm{bar}}$ variation of ± 0.2 nm.

In a first approach a rectangular In mole fraction profile in the QWs is assumed to estimate the layer thicknesses of the QWs and barriers and the QW In mole fraction ($x^{\mathrm{In}}_{\mathrm{solid}}$ ). Since $d_{\mathrm{QW}}$ is known for each sample from the HR-XRR simulations, $x^{\mathrm{In}}_{\mathrm{solid}}$ can be determined by fitting the HR-XRD $\Omega - 2\Theta$ scans at the (0002) reflection of the samples of set $B^{\mathrm{dQW}}$. In Fig. 4.3 the $\Omega - 2\Theta$ scans for the samples with $t_{\mathrm{QW}} = 40$ s and 100 s of set $B^{\mathrm{dQW}}$ are plotted together with simulations using different values for $x^{\mathrm{In}}_{\mathrm{solid}}$ . Clearly, the experimental data of the sample with $t_{\mathrm{QW}} = 40$ s is fitted best with a lower In mole fraction whereas the $\Omega - 2\Theta$ scan of the sample with $t_{\mathrm{QW}} = 100$ s is

fitted best with a higher $x^{\mathrm{In}}_{\mathrm{solid}}$ or strain.

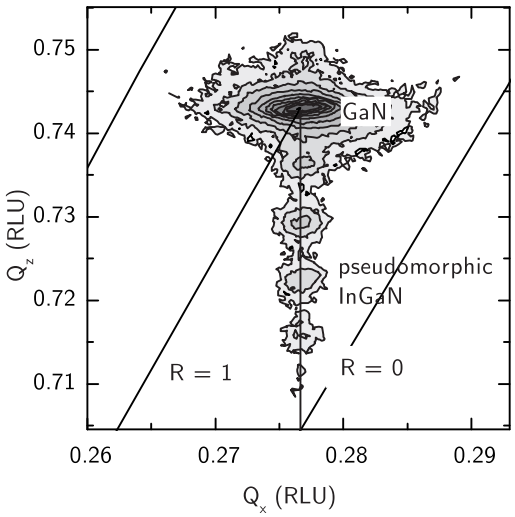


Figure 4.5: Reciprocal space mapping around the $(10\bar{1}5)$ reflection of the sample of set $B^{\mathrm{dQW}}$ with $t_{\mathrm{QW}} = 100$ s showing pseudomorphic growth of the InGaN QWs. $Q_{\mathrm{z}}$ and $Q_{\mathrm{x}}$ are the reciprocal coordinates in reciprocal lattice units (RLU). The black line denoted with R=0 and R=1 represent the layer peak positions of fully strained and fully relaxed material, respectively.

Since no relaxation of the InGaN QW layer is observed in the reciprocal space mapping around the $(10\bar{1}5)$ reflection for the sample with the highest $t_{\mathrm{QW}}$ of set $B^{\mathrm{dQW}}$ (see Fig. 4.5) and the QW growth rate is assumed to be constant as discussed above, the increase of the strain with increasing $t_{\mathrm{QW}}$ can directly be correlated with an increase of the In mole fraction in the QWs. The structural parameters of the QWs derived from the HR-XRR and HR-XRD measurements, when assuming a rectangular In mole fraction profile, are noted in Tab. 4.1.

In order to qualitatively explain the $t_{\mathrm{QW}}$-dependency of $x^{\mathrm{In}}_{\mathrm{solid}}$, the influence of the QW interface abruptness on the incorporated In in the QW is discussed. A non-intentional grading of the In mole fraction in the QW can occur due to In surface segregation effects during active region deposition. Segregation in MQW structures is well known for the growth of ternary compounds [88] and has also been confirmed on InGaN MQW structures by RHEED [89] or TEM investigations [81, 90]. As described in Sec. 3.4.2 the segregation process is driven by a reduction of the surface energy when In atoms segregate from the bulk to sites of lower N coordination such as surface step edges or vicinal micro facets. This results in a reduced In concentration in the first ML of the InGaN QW on the one hand and an increase of the In concentration of the topmost MLs and the surface on the other hand. Additionally to this, In from the gas phase is found to accumulate on the surface within a few seconds [91] forming a metallic ad-layer, which enhances the indium incorporation [92]. The time-delayed accumulation plus the surface segregation of In can explain the grading of the In mole fraction at the barrier/well interface whereas the incorporation of excess indium from the surface into the overgrown GaN barrier results in an In mole fraction grading of the well/barrier interface.

### 4.2.2 Theoretical description of the In segregation

The cause of the In segregation has been described in Sec. 3.4.2. In this section the effect on the vertical In mole fraction distribution is discussed. To model the local

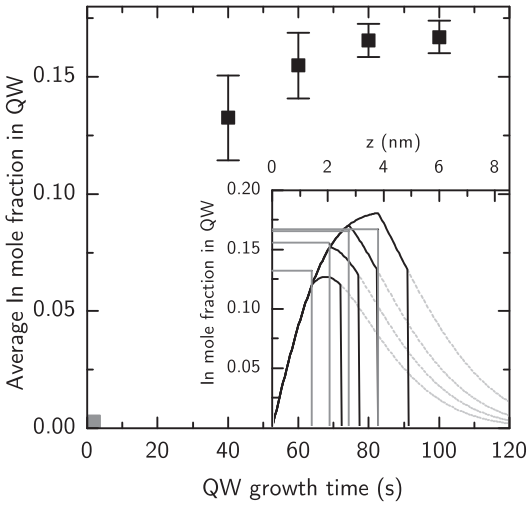


Figure 4.6: The squares represent the average In mole fraction in the QWs of set $B^{\mathrm{dQW}}$ revealed by HR-XRD when assuming abrupt interfaces. The inset shows the $x^{\mathrm{In}}_{\mathrm{solid}}$ profile that is used for fitting the $\Omega - 2\Theta$ scans (dark grey line). The black line represent simulated local In mole fraction profiles when assuming equal segregation at barrier/well and well/barrier interface. Due to the growth interruption after several MLs the In is removed from the surface. The broken grey lines correspond to $x^{\mathrm{In}}_{\mathrm{solid}}$ profiles without growth interruption.

In mole fraction variation of the QWs in growth direction (z) the $t_{\mathrm{QW}}$-dependency of $x^{\mathrm{In}}_{\mathrm{solid}}$ for the samples of set $B^{\mathrm{dQW}}$ is analyzed (see Fig. 4.6). Since $x^{\mathrm{In}}_{\mathrm{solid}}$ is derived by assuming a rectangular In mole fraction profile it represents the average In mole fraction in the QWs. To fit a theoretical model of the indium distribution to the experimental data, the fraction of the MQW structure whose indium molar fraction is averaged needs to be defined. For non-abrupt well/barrier interfaces such a definition is not straightforward. Having in mind the limited number of experimental data points, the model should be kept as simple as possible. Therefore, the range of averaging was set equal to the time when the QW is grown plus the time available for segregation ($t_{\mathrm{seg}}$) until the barrier growth is interrupted for increasing the growth temperature. During the growth break the In desorbs from the surface, which prevents the incorporation of In in the subsequently grown layer. Moreover, the average indium content derived from the model for the indium distribution is made insensitive to the exact choice of the starting time of the averaging by assuming identical delays for the indium incorporation when switching on the indium flow and for the indium desorption from the surface when switching off the indium flow. Fitting the model then includes solely the variation of the indium distribution within the well and a part of the barrier of a given thickness. Based on a model proposed by Mayrock et al. [93] the parameters to be fitted are the In segregation constant ($\tau_{\mathrm{seg}}$) and the converging In mole fraction ($x_0$) when using the assumptions described above:

$$x(t) = \begin{cases} 0 & t < 0 \\ x_0\, erf(\frac{t}{\tau_{seg}}) & 0 \le t < t_{QW} \\ x_0\, erf(\frac{t_{qw}}{\tau_{seg}})[1 - erf(\frac{t-t_{QW}}{\tau_{seg}})] & t_{QW} \le t < t_{QW} + t_{seg} \\ 0 & t \ge t_{QW} + t_{seg} \end{cases} \tag{4.1}$$

By integrating x(t) from t=0 to $t_{\mathrm{QW}}$+$t_{\mathrm{seg}}$ the total amount of In in the QWs is calculated and compared with the experimentally determined total amount of In in each QW of set $B^{\mathrm{dQW}}$. The least square fit reveals a vertical segregation length of about 5 to 6 MLs. The value is in good agreement with the results of other groups [90, 94].

The inset in Fig. 4.6 displays the calculated $x(z)$ profiles for the samples of set $B^{\mathrm{dQW}}$ using the fitted parameters $\tau_{\mathrm{seg}}$ and $x_0$ for two different cases regarding the boundary conditions: If the barrier growth is interrupted the In desorbs from the surface, which limits the segregation to the amount of MLs deposited until the growth interruption (see black line). Without this limitation the local In mole fraction exhibits a slow decay as the barrier is grown (broken grey lines). It is noted that for thin wells with $d_{\mathrm{QW}} < 1.5\,\mathrm{nm}$ the model suggests a maximum indium molar fraction which is $< 80\%$ of the value achieved in thick wells due to a delayed In incorporation at the first barrier/well interface. Secondly, the well width increases while the barrier width decreases, due to segregation of In in the subsequently deposited barrier layer. The QW and barrier growth rates determined above therefore represent the thickness increase of the layers when In supply is switched on or off, respectively. After switching off the In supply the QW layer width is further increased by incorporation of In from the In-rich surface ad-layer. The findings are in good agreement with the results of Gerthsen et al. [95], who found higher QW thicknesses with respect to the nominal thickness for short QW growth durations. On the other hand, the average In mole fraction in the QW is lower in the used model with segregation compared to the average In mole fraction in the model with abrupt interfaces used for simulation of the HR-XRD data (see red lines in Fig. 4.6). Since the product of QW thickness and the average In mole fraction in the QW is equal for both models, their $\Omega - 2\Theta$ diffraction patterns is identical [87]. Hence, it is not possible to quantify the abruptness of the interfaces from the $\Omega - 2\Theta$ scans alone.

## 4.3 Influence of the structural properties on the luminescence

### 4.3.1 $d_{QW}$-dependency of the luminescence wavelength

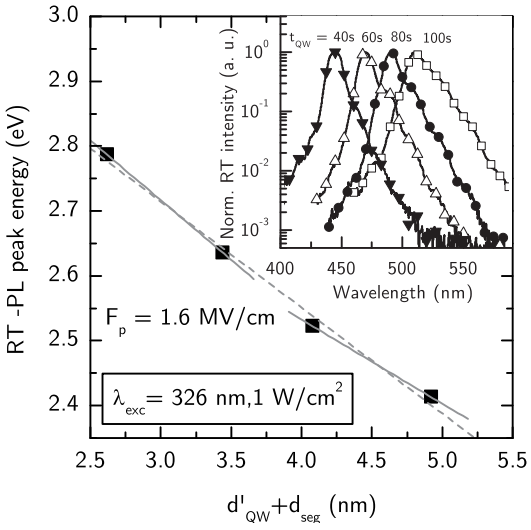


Figure 4.7: Linear fit the of the transition energies of set $B^{\mathrm{dQW}}$ reveals a $F_{\mathrm{pz}}$ of 1.6 MV/cm. The inset shows the $d_{\mathrm{QW}}$-dependency of the RT-PL spectra.

In order to obtain information on the luminescence properties, PL measurements were conducted on set $B^{\mathrm{dQW}}$. Fig. 4.7 shows the $d_{\mathrm{QW}}$-dependency of the PL peak en-

ergy and the PL spectra measured at RT. Hereafter, $d_{\mathrm{QW}}$ is considered as the nominal well thickness plus the distance that In segregates into the barrier ($d'_{\mathrm{QW}}$+$d_{\mathrm{seg}}$). The emission wavelength is red-shifted around 70 nm as the well thickness increases from around 2.5 to 5 nm. With increasing well thickness the separation of the carriers increases under the influence of the intrinsic fields. The analysis of the corresponding energy shift with changing $d_{\mathrm{QW}}$ allows the estimation of the intrinsic field strength. InvestigationS by Hangleiter et al. [96] revealed a linear $d_{\mathrm{QW}}$-dependency of the transition energy for $d_{\mathrm{QW}} > 2$ nm. Therefore, higher order effects, e.g. the $d_{\mathrm{QW}}$-dependency of the wave function quantization energy, the exciton binding energy or the electron mass, are neglected for fitting the experimental data. The linear fit of the data reveals an electrical field strength of around 1.6 MV/cm. Clearly, the slopes of the transition energy change is different for thin and thick QWs (see solid lines in Fig. 4.7). The difference can be explained by the decrease of the In mole fraction as $d_{\mathrm{QW}}$ decreases due to the incorporation delay described in Fig 4.6 in Sec. 4.2.2.

The piezoelectric polarization ($P_{\mathrm{pz}}$) in growth direction can be calculated using the elements of the piezoelectric tensor ($e_{\mathrm{ij}}$) according to Sec. 3.4.2:

$$P_{\mathrm{pz}} = e_{31}(\epsilon_{\mathrm{xx}} + \epsilon_{\mathrm{yy}}) + e_{33}\epsilon_{\mathrm{zz}} \tag{4.2}$$

The $P$ in growth direction is then the superposition of $P_{\mathrm{pz}}$ and the difference of the spontaneous polarization of the well and the barrier material:

$$P = P_{\mathrm{pz}} + (P_{\mathrm{sp}}^{\mathrm{QW}} - P_{\mathrm{sp}}^{\mathrm{barrier}}) \tag{4.3}$$

The material parameter $e_{\mathrm{ij}}$ and $P_{\mathrm{sp}}$ for InGaN are derived by linear interpolation of the parameters of InN and GaN [97]. In Fig. 4.8 the net polarization strength ($F_{\mathrm{p}}$) is plotted as a function of the In mole fraction in the solid of the quantum well. Under the influence of a field the wave functions are spatially separated. Due to the quantum-confined Stark effect (QCSE) [30] the luminescence is red-shifted as outlined in the lower right corner of the Fig. 4.8. Additionally, the transition probability is reduced in such QWs.

The theoretical net field strength is around 3 MV/cm for $x_{\mathrm{solid}}^{\mathrm{In}}$ =0.13 or 3.4 MV/cm for $x_{\mathrm{solid}}^{\mathrm{In}}$ =0.17, respectively. The discrepancy between the experimental and the theoretical value can be caused by several effects, e.g. the uncertainty of the material parameters, the screening of the intrinsic fields by free carriers or the non-abrupt interfaces between well and barrier. To achieve a better agreement between the theoretical calculations and the experiments, 50% polarization is assumed in the simulations (QIP,SILENSe,LASTIP) presented in this work.

Using the experimentally obtained field strength in the QWs the $d_{\mathrm{QW}}$-dependency of the RT-PL peak wavelength of a MQW as in the experiment is simulated using QIP. With respect to the experimentally determined blue-shift of 70 nm as $d_{\mathrm{QW}}$ decreases (see Fig. 4.7) the simulation predicts a lower blue-shift of 50 nm. The blue-shift becomes even smaller, if the QW width is increased by the distance the In segregates into the barrier ($d_{QW} + d_{seg}$). Assuming an identical interface roughness and spatial In mole fraction distribution in all samples the higher blue-shift in the experiment

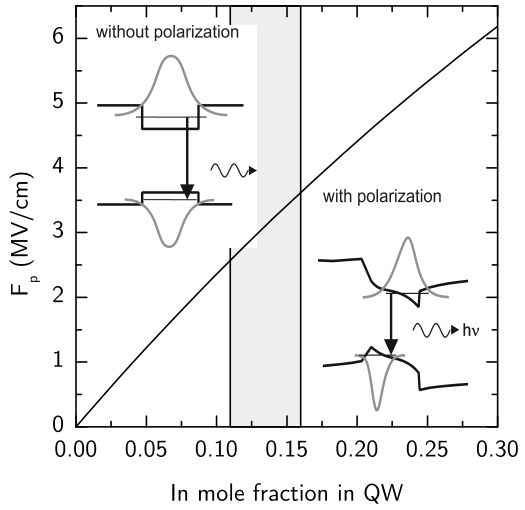


Figure 4.8: Net field strength in the QWs as a function of the In mole fraction in the solid after Romanov et al. [75]. The drawings outline the wave functions in the QW without (upper) and with (lower) field.

can be attributed to a decrease of $x^{\mathrm{In}}_{\mathrm{solid}}$ with decreasing $t_{\mathrm{QW}}$. A decrease of $x^{\mathrm{In}}_{\mathrm{solid}}$ from 0.17 to 0.13 as estimated above would contribute to an additional blue-shift of 16 nm and therefore supports the segregation reduced In mole fraction in the solid model described above.

### 4.3.2 Recombination dynamics

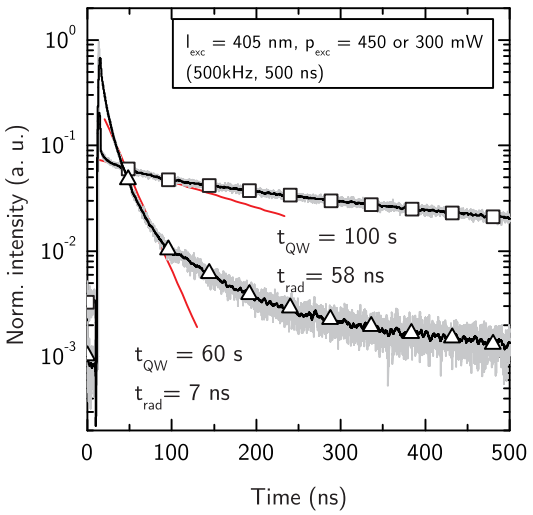


Figure 4.9: $t_{\mathrm{QW}}$-dependency of the time resolved PL transients measured at 10 K for the samples of set $B^{\mathrm{dQW}}$ with $t_{\mathrm{QW}}$ = 60 s and 100 s, respectively. The red lines represent the linear fit to the experimental data between 20 ns and 100 ns. A 405 nm LD was used for excitation with $P_{\mathrm{exc}}$=300 mW ($t_{\mathrm{QW}}$=60 s) or $P_{\mathrm{exc}}$=450 ($t_{\mathrm{QW}}$=100 s), respectively. The repetition rate was 500 kHz and the pulse length 500 ns.

The influence of the intrinsic fields on the luminescence is revealed by analyzing the recombination dynamics of sample set $B^{\mathrm{dQW}}$. Clearly, the TR-PL transients the in Fig. 4.9 changes as $t_{\mathrm{QW}}$ is varied. As a consequence of the intrinsic fields, the spatial separation of the wave functions and thus the $\tau_{\mathrm{rad}}$ increases as well width increases. Fitting the decay between 20 and 100 ns the $\tau_{\mathrm{rad}}$ is estimated to 58 ($t_{\mathrm{QW}}$ = 100 s) or 7 ns ($t_{\mathrm{QW}}$ = 60 s), respectively.

In order to qualify the crystal perfection of the samples with different QW growth times resulting in different thick QWs the TD-PL signal is additionally analyzed using Fig. 4.10: At low temperatures the carrier diffusion to non-radiative recombination

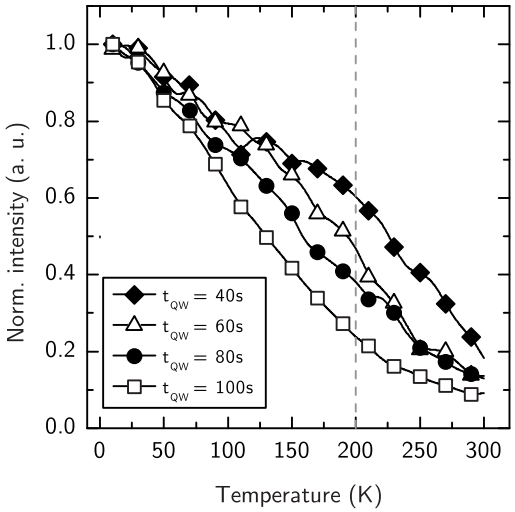


Figure 4.10: Temperature resolved PL measurements conducted on sample set $B^{\mathrm{dQW}}$. A 378 nm diode laser was used for excitation with an excitation power density of 20 W/cm$^2$.

centers in the QWs is limited. Hence, the luminescence is dominated by radiative recombination processes. Increasing the temperature up to 200 K the sample with the long $t_{\mathrm{QW}}$ exhibits the strongest decrease of the intensity. As a consequence of the long radiative carrier life time ($\tau_{\mathrm{rad}}$) the carriers increasingly recombine non-radiatively as the temperature increases resulting in a stronger decrease of the intensity.

Above 200 K the carriers are thermally activated and increasingly diffuse to non-radiative recombinations centers, e.g. threading dislocations and point defects. Clearly, the thick QWs show a lower decrease of the intensity as the temperature increases from 200  to room temperature. These QWs feature a higher In mole fraction in the solid and a higher total amount of In in the active region as has been shown above. Minsky et al. [98, 31] showed that these structural properties result in a higher spatial In mole fraction fluctuation and hence a higher localization of the carriers.

In summary, the ratio of the intensity at RT and 10 K was determined in order to reveal the material quality. The ratio provides information about the localization of the carriers in band gap fluctuations. Evidence was found that a higher localization of the carriers in band spatial gap non-uniformities in the wider wells reduces the intensity decay by non-radiative recombination as the temperature increases to RT. Furthermore, the strong decrease of the TD-PL signal between 200 K to RT suggests short non-radiative life times of the increasingly mobile carriers.

### 4.3.3 Investigation of lateral luminescence non-uniformities

In order to investigate the amount of spatial band gap non-uniformities LT-CL is measured on sample set $C^{\mathrm{dQW}}$. Beside the variation of the In mole fraction in growth direction described above in Sec. 4.2.2, lateral In mole fraction variations are observed in InGaN driven by a non-uniform In incorporation (see Sec. 3.4.2) or a lateral redistribution of In as has been observed by Queren et al. [99] for thin InGaN layers.

Fig. 4.11 a) shows the spatially resolved LT-CL peak wavelengths for the sample of set $C^{\mathrm{dQW}}$ with $t_{\mathrm{QW}} = 45$ s. The wavelength histogram (see Fig. 4.11 b)) features a symmetric single modal Gaussian distribution centered around 444 nm with a standard

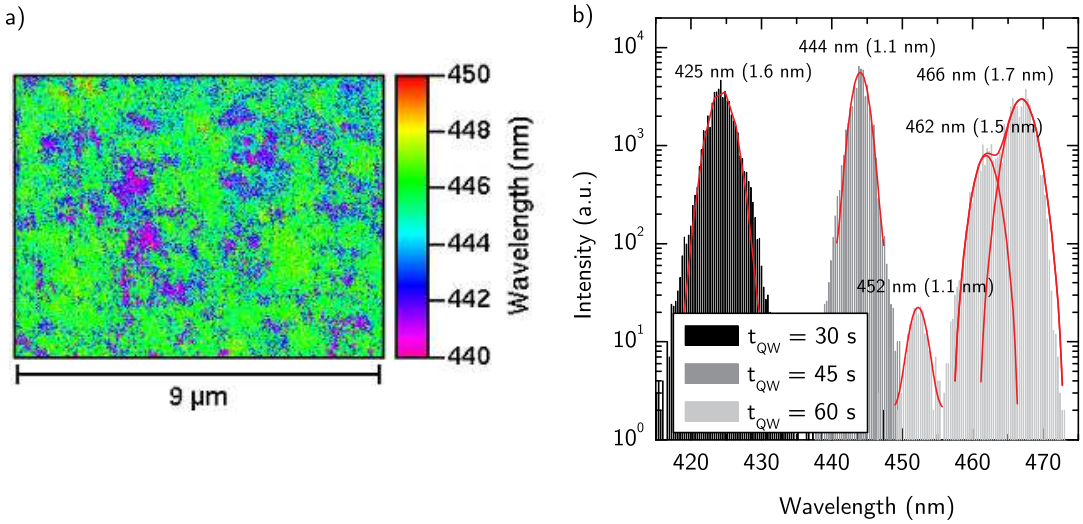


Figure 4.11: a) (Color online) Spatial variation of the local LT-CL peak wavelength of a sample of set $C^{\mathrm{dQW}}$ with $t_{\mathrm{QW}} = 45\,\mathrm{s}$. b) Distribution of the local LT-CL peak wavelengths for all samples of set $C^{\mathrm{dQW}}$. The peaks are labeled with the peak wavelength and the standard deviation.

deviation ($\sigma$) = 1.1 nm. Increasing $t_{\mathrm{QW}}$ to 60 s results in an increase of the spatial wavelength variation. The wavelength histogram features peaks at 452, 462 or 466 nm with $\sigma$ of 1.1, 1.5 or 1.7 nm, respectively. This effect is addressed in several publications and is explained with higher spatial In mole fraction fluctuations [98, 31, 99] or higher $d_{\mathrm{QW}}$ variations caused by interface roughening [100, 101] with increasing $d_{\mathrm{QW}}$. The increase of the lateral luminescence fluctuations as $t_{\mathrm{QW}}$ increases may contribute to an additional red-shift of the PL wavelength due to deeper localization states [83]. The increase of the band gap fluctuations as $T_{\mathrm{QW}}$ increases is in good agreement with the results of the TD-PL measurements above (see Sec. 4.3.2). The sample with the highest spatial band gap fluctuations exhibits the highest RT to 10 K intensity ratio of the PL but the strongest decrease of the intensity above 200 K. Both findings point to strong localization and short non-radiative life times of the carriers associated with a low crystal perfection of the material.

Interestingly, Fig. 4.11 b) shows an increase of the spatial wavelength variations when $t_{\mathrm{QW}}$ is reduced from 45 s to 30 s. Due to the low QW thickness of only four MLs a lateral variation of a single ML represents a high relative QW thickness fluctuation. Furthermore, the average In mole fraction of thin QWs is very sensitive to QW thickness fluctuations as can be seen in the inset of Fig. 4.6. Hence the increase of the spatial wavelength distribution found for the sample of set $C^{\mathrm{dQW}}$ with very short QW growth times can be explained by an increased $\Delta d_{\mathrm{QW}}/d_{\mathrm{QW}}$ and the resulting increase of the lateral In mole fraction variation in the QWs.

## 4.4 Summary and conclusions

In this chapter the growth and analysis of InGaN/GaN MQW structures was described. The exact determination of the In distribution in the structures and the

correlation with the luminescence properties enables the setup of active regions for laser structures later on. By varying the well width the growth and design limitations regarding this parameter in later laser heterostructure were evaluated. Thin $In_{0.15}Ga_{0.85}N$ wells with thicknesses below 1.5 nm and thick wells with thicknesses above 3.5 nm show increased spatial band gap variations due to well thickness or In mole fraction non-uniformities. The shift of the luminescence wavelength as the QW width varies allowed the determination of the intrinsic field strength due to piezoelectric and spontaneous polarization. The estimated value of 1.6 MV/cm will be used in the next chapters for device simulations with improved the accuracy.

Furthermore, the analysis of the quantum structures revealed that the average In mole fraction in the quantum well varies in growth direction on a small scale due to In segregation effects. Modeling the In mole fraction profile in the QWs suggests that the In mole fraction decrease is due to a delayed In incorporation at the barrier/well interface and segregation of In from the well into the barrier. A segregation length of about 2 nm was revealed as a measure for the In mole fraction variations in growth direction. This value also defines the limit of the quantum structure perfection or the interface abruptness, respectively.

# 5

# Influence of the growth parameters on InGaN material and LD device properties

In this chapter it is discussed how the MOVPE growth conditions affect the material properties. Therefore, MQW structures were grown at different temperatures and analyzed. As has been shown by many other groups, the MQW growth temperature has a great impact on the structural properties, e.g. In mole fraction [102] and distribution [103, 104], defect formation[65], as well the efficiency of MQW structures [105, 106] and laser devices [107, 108]. Later on devices are prepared that feature the same growth condition variations in the active regions as the MQW structures. The device characteristics are correlated with the MQW material properties in order to enable growth optimizations for laser heterostructures.

## 5.1 Sample and growth conditions variation

First, as set ($D^{\mathrm{T_{AR}}}$) of MQW samples of type b) in Fig. 2.1 is grown on 2 inch sapphire based (0001) GaN templates. The structures feature a 1.2 $\mu$m aluminum gallium nitride (AlGaN) cladding and a 100 nm wide waveguide layer underneath the 3× InGaN/InGaN:Si MQWs. The QWs are grown using similar precursor and growth conditions ($t_{\mathrm{QW}}$=90 s) as for set $B^{\mathrm{dQW}}$ and $C^{\mathrm{dQW}}$ in chapter 4 but different active region growth temperatures ($T_{\mathrm{AR}}$) between 850°C and 890°C. The barrier layers are grown at QW growth temperature using constant growth conditions except of the $Si_2H_6$ flux. Imaginary dividing the barrier layer into five parts, the fist two and the last two parts are non-intentionally doped. The center part is n-doped with $\sim 5{\times}10^{18}$ $\mathrm{cm^{-3}}$ using $Si_2H_6$ in order to improve the interface quality [109]. The samples were grown in the Aix2400G3-HT with $p_{\mathrm{reactor}} = 400$ mbar and $x^{\mathrm{In}}_{\mathrm{vapor}} = 0.3$ / 0.03 for well / barrier growth, respectively.

After growth, the wafers of set $D^{\mathrm{T_{AR}}}$ are quartered. The first quarter of each wafer was analyzed by HR-XRD, PL and SEM. The second and third quarter of every sample are finished to an optically or electrically pumpable LD structure (see type c) and d) in Fig. 2.1) by a further epitaxial step. The optically pumpable structures are denoted as set $D^{\mathrm{T_{AR}}}_{\mathrm{oLD}}$ and additionally feature a 100 nm GaN waveguide and an 20 nm $Al_{0.20}Ga_{0.80}N$ cap on top of the different MQWs. In order to complete the current injection laser structures (set $D^{\mathrm{T_{AR}}}_{\mathrm{LD}}$) 100 nm GaN:Mg with an $Al_{0.20}Ga_{0.80}N$:Mg EBL, a 120× $Al_{0.12}Ga_{0.88}N$/GaN:Mg SPSL and an 20 nm GaN:Mg cap are deposited on the

different MQW samples in the Aix200-HT reactor. The structures are processed to BA-LDs for opto-electrical characterization.

## 5.2 Determination of the structural properties of the MQW samples

The structural properties of set $D^{\mathrm{TAR}}$ were determined by HR-XRD as described in section 4.2. The analysis of the $\Omega - 2\Theta$ scans around the (0002) reflection revealed well and barrier thicknesses of 3.5 and 7.5 nm for all samples in set $D^{\mathrm{TAR}}$. While the In mole fraction of the barrier layers is around 0.02 for all samples, $x_{\mathrm{QW}}$ decreases from 0.13 to 0.07 as $T_{\mathrm{AR}}$ increases from 850 to 890°C. Since $x^{\mathrm{In}}_{\mathrm{vapor}}$ is identical for all samples the corresponding indium incorporation efficiency ($\nu_{\mathrm{In}}$) decrease from 0.37 to 0.19 as the temperature increases. $\nu_{\mathrm{In}}$ is given by the ratio of the molar fraction of indium in the solid and the vapor [110]. Due to the high In vapor pressure the desorption of In from the surface increases and thus the incorporation decreases as $T_{\mathrm{AR}}$ increases.

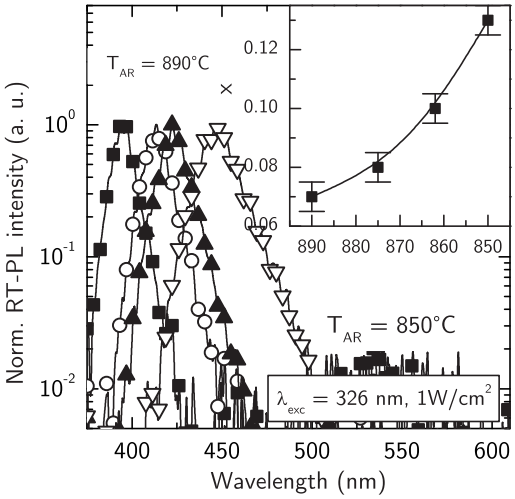


Figure 5.1: Normalized RT-PL spectra of the samples of set $D^{\mathrm{TAR}}$. The inset shows the $x_{\mathrm{QW}}$ as a function of the growth temperature.

Fig. 5.1 shows the normalized PL spectra at room temperature for set $D^{\mathrm{TAR}}$. As $T_{\mathrm{AR}}$ decreases the wavelength increases from 395 nm to 447 nm and the peak width increases from 14 to 24 nm. The red-shift is mainly due to two effects: The band gap energy decreases with increasing In mole fraction in the well. Secondly, the higher strain of the QW results in higher piezoelectric fields (see Fig. 4.8) and therefore a stronger red-shift and peak broadening as a consequence of the stronger QCSE. An overview of the structural and optical properties of set $D^{\mathrm{TAR}}$ can be found in Tab. 5.1.

## 5.3 Characterization of the crystal perfection of the MQW samples

### 5.3.1 PL recombination dynamics

As described in Sec. 4.3.2, the RT/10 K PL ratio is a measure for the amount of non-radiative recombination. For sample set $D^{T_{AR}}$ the RT/10 K PL ratios are noted in Tab. 5.1. All samples exhibit an identical RT/10 K PL ratio except for the sample grown at the lowest temperature. Since this samples also features a higher piezoelectric field $\tau_{rad}$ is lower due to the wider spatial separation of the carriers in the QW [105]. Thus, the coincidence of a higher RT/10 K PL ratio and the longer $\tau_{rad}$ points to significantly lower non-radiative recombination rates in these samples. Since the material quality of InGaN is known to deteriorate with increasing In mole fraction in the solid [111, 98] the increase of the RT/10 K PL ratio as $T_{AR}$ decreases can be explained again by higher localization of the carriers in band gap-fluctuations.

### 5.3.2 Spatial CL non-uniformities

Fig. 5.2 shows monochromatic LT-CL-mappings at 6 K of the sample grown at highest $T_{AR}$ (first row) and lowest $T_{AR}$ (second row) of set $D^{T_{AR}}$. The monochromatic wavelengths correspond to the wavelengths where the luminescence intensity has dropped by 50% on the short and long wavelength side of the spectra (left and right column) and the peak wavelength (center). Both samples show a circular luminescence distribution related to the growth spirals as has been observed for the thick InGaN layer in Sec. 3.4.2. Interestingly, the main contribution of the luminescence originated from different areas of the spirals as $T_{AR}$ changes (see the center column in Fig. 5.2 - corresponding to the peak wavelength and therefore the highest intensity). The sample grown at high $T_{AR}$ radiates mainly from the side surfaces of the spirals, whereas the highest luminescence intensity originates from the center of the spiral for low $T_{AR}$.

First, the luminescence distribution of the sample grown at high $T_{AR}$=890 °C is discussed: As can be seen in the first row of Fig. 5.2, the main luminescence originated from the side-surfaces of the spirals with an alleged locally increased In incorporation (see Sec. 3.4.2). Due to the locally reduced band gap energy the carriers diffuse from areas with a wider band gap to the side walls and recombine radiatively.

| $d_{well}$ (nm) | $d_{bar}$ (nm) | $x^{In}_{vapor}$ | $T_{AR}$ ( °C ) | $x^{In}_{solid}$ (well) | $\nu_{In}$ (well) | RT-$\lambda_{PL}$ (nm) | FWHM (nm) | RT/10 K PL int. |
|---|---|---|---|---|---|---|---|---|
| 3.5 | 7.5 | 0.29 | 850 | 0.13 | 0.37 | 457 | 13.8 | 0.28 |
| | | | 862 | 0.10 | 0.27 | 428 | 12.6 | 0.04 |
| | | | 875 | 0.08 | 0.21 | 416 | 11.4 | 0.04 |
| | | | 890 | 0.07 | 0.19 | 398 | 6.84 | 0.04 |

Table 5.1: Heterostructure properties and the varied growth parameters of the samples of set $D^{T_{AR}}$. The remaining growth parameters were identical for all sample sets. A 387 nm diode laser was used for excitation (20 W/cm$^2$) of the PL.

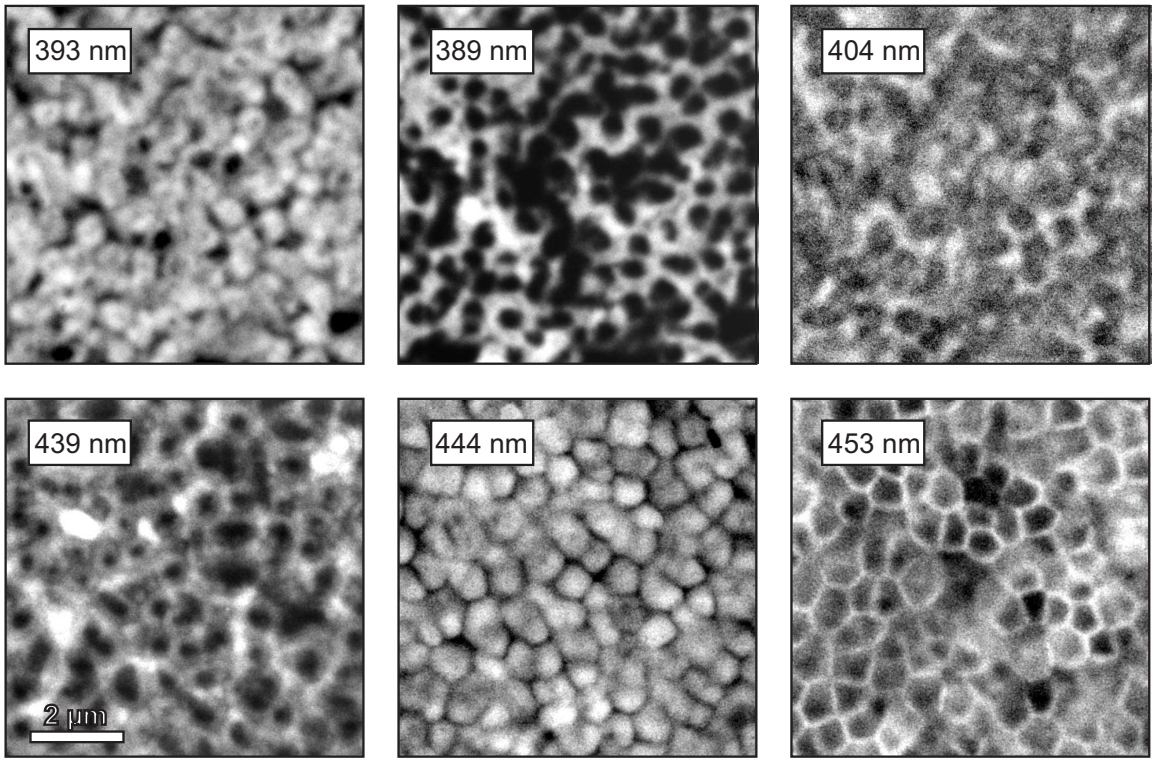


Figure 5.2: 10.000× monochromatic LT-CL images at 6 K of the sample grown at highest $T_{\mathrm{AR}}$ = 890 °C (first row) and lowest $T_{\mathrm{AR}}$=850 °C (second row) of set $D^{\mathrm{T_{AR}}}$. The measurement wavelengths are noted in upper left corner and represent the short wavelength slope (left column), peak wavelength (center column) and long wavelength slope (right column) of the MQW emission wavelength.

The sample grown at 850 °C exhibits the highest luminescence intensity from the center of the spirals (see second row in Fig. 5.2). Different from the bulk InGaN layers in chapter 3, in the MQW samples the carriers are vertically confined in the QW. The evolution of a spiral represents a locally increased growth rate or well thickness, respectively. As shown in section 4.3 the band gap is reduced as $d_{\mathrm{QW}}$ increases and more carriers are confined in this region. In contrast to the sample grown at 890 °C, the local increase of the growth rate (or respectively the spiral height) has to be higher in order to explain the luminescence from the center of the spirals. This assumption is supported by the fact that at low $T_{\mathrm{AR}}$ the mobility of the adatoms on the surface is lower. According to section 3.3.2 the spiral formation is enhanced in this growth regime.

In summary, the LT-CL measurements reveal different carrier localization regions for the different $T_{\mathrm{AR}}$. At high $T_{\mathrm{AR}}$ the luminescence originates from local band gap minima correlated with a higher In mole fraction in the sidewalls of the growth spirals. As the height of the spirals increases at low $T_{\mathrm{AR}}$, the highest LT-CL intensity is measured in the center of the spirals. In this case, the increased well thickness in the center of the spiral corresponds to a locally strong reduced band gap where carriers are efficiently confined.

## 5.4 Lasing of heterostructures

### 5.4.1 Gain measurements of the optical pumpable laser structures

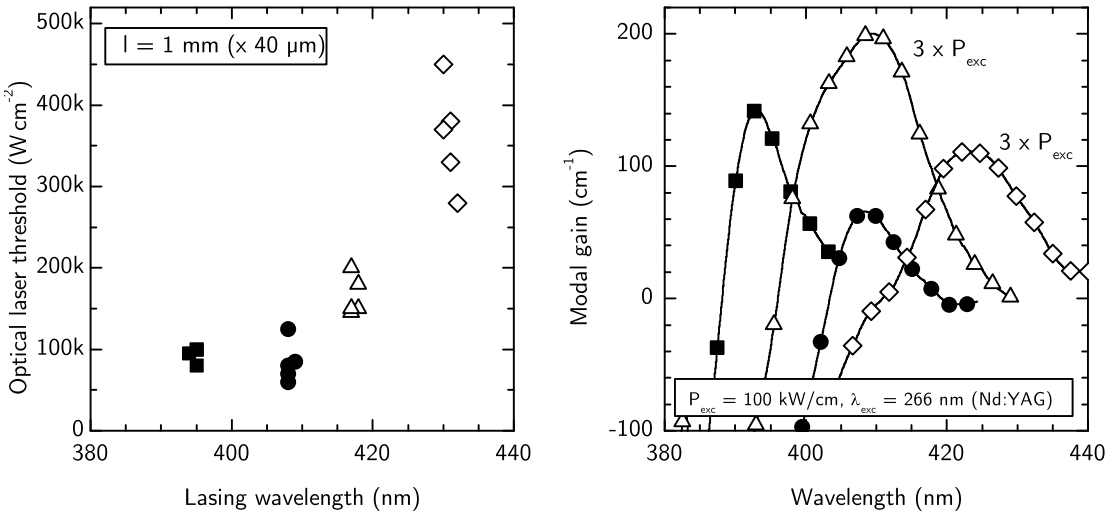


Figure 5.3: a) Optical threshold power densities as a function of the emission wavelength for sample set $D_{\mathrm{LD}}^{\mathrm{T_{AR}}}$. b) Net gain spectra. The samples were excited using a Nd:YAG laser with $P_{\mathrm{exc}}$=100 (filled symbols) or 350 kW/cm$^2$ (open symbols). The cavity width is 40 $\mu$m and the length is 1 mm.

Fig. 5.4 shows the optical threshold power density ($i_{\mathrm{th}}$) as a function of the emission wavelength at threshold (a) and the gain spectra (b) of the samples of set $D_{\mathrm{LD}}^{\mathrm{T_{AR}}}$. Clearly, $i_{\mathrm{th}}$ increases as $T_{\mathrm{AR}}$ decreases. The higher threshold is due to a lower peak gain for the samples grown at low $T_{\mathrm{AR}}$. In comparison to the low excitation PL spectra (see Fig. 5.1) the peak gain shows a significant blue-shift. The shift is due to band-filling, band gap renormalization and the diminishment of the QCSE at high excitation. All spectra show a strong decrease to shorter wavelengths due to absorption above the band edge. On the longer wavelength side where the material is transparent wavelength-dependent wave guiding losses occur.

### 5.4.2 Opto-electric characterization of the current injection LDs

After processing the samples of set $D_{\mathrm{LD}}^{\mathrm{T_{AR}}}$ to BA-LD $j_{\mathrm{th}}$ is determined. Fig. 5.4 shows the P-U-I characteristics of the samples. The sample grown at $T_{\mathrm{AR}}$=850 °C with the lowest optical gain in set $D_{\mathrm{oLD}}^{\mathrm{T_{AR}}}$ showed no lasing and is therefore not plotted. The emission wavelengths at the threshold were 396, 408 and 418 nm for $T_{\mathrm{AR}}$ = 890, 875 and 862°C, respectively. The results regarding wavelengths and $j_{\mathrm{th}}$ trends are in good agreement with the findings of the optical pump experiments. From the optical pumping experiments it is therefore possible to gain device data without the high processing effort of a current injection LD. This method is therefore used in the following section to optimize the growth conditions in order to improve the LD device characteristics.

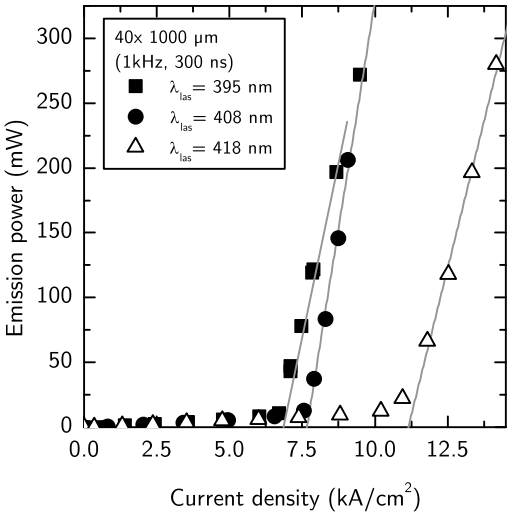


Figure 5.4: L-I characteristics of the current injection BA-LD of set $D^{\mathrm{T_{AR}}}_{\mathrm{oLD}}$. The emission wavelengths are noted in the box. The $T_{\mathrm{AR}}$ are accordingly to the figures above. The pulse rate and width was 1 kHz and 300 ns, respectively. The resonator width and length 40 and 1000 $\mu$m.

## 5.5 Correlation of material properties and device characteristics

The distinct broadening of the gain spectra as $T_{\mathrm{AR}}$ decreases indicates a deterioration of the crystal perfection of the active region. Although the low excitation PL spectra shows only single peaks for all samples of set $D^{\mathrm{T_{AR}}}$ (see Fig. 5.1), the gain spectra for the samples grown at low $T_{\mathrm{AR}}$ show distinct shoulders. These features suggest locally separated recombination centers with different transition energies as observed by LT-CL (Fig. 5.2). The wavelength shift between the center and the edge of the spirals corresponds well with the distance of the peaks in the gain spectra.

The increase of the gain can not solely be correlated with the higher perfection of the quantum wells at higher temperatures. Moreover, the variation of the structural properties in the sample affect the material as well as the modal gain and thus $i_{\mathrm{th}}$. The intrinsic field strength decreases and thus wave function overlap increases as the $T_{\mathrm{AR}}$ increases. The consequential increase of the oscillator strength [29] in turn corresponds to a higher material gain. Additionally, the confinement of the optical mode differs due to the different emission wavelengths in these structures. In general, the confinement decreases as the difference of the refractive index ($n$) between the GaN wave guiding and the surrounding AlGaN cladding layer decreases.

Fig. 5.5 shows $n$ as a function of the wavelength for AlGaN with different $x^{\mathrm{Al}}_{\mathrm{solid}}$. Clearly, the difference between the $n$ of GaN and AlGaN decreases as the wavelengths increases. The inset shows the simulated optical confinement factor ($\Gamma$) for the a heterostructure layout in set $D^{\mathrm{T_{AR}}}_{\mathrm{oLD}}$ using SILENSe. $\Gamma$ decreases as the wavelengths of the laser increases due to increased leakage of the mode into the substrate. The strong decrease of $\Gamma$ as the wavelengths decreases is due to more efficient absorption in the p-type doped layer [46] of the heterostructure.

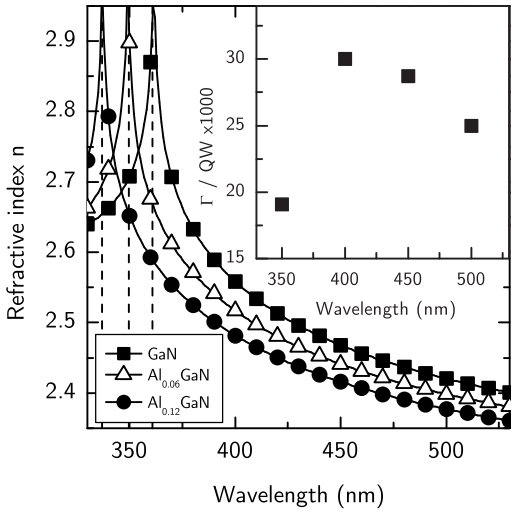


Figure 5.5: Calculation of the refractive index for AlGaN with $x^{\mathrm{Al}}_{\mathrm{solid}} = 0$, 0.06 and 0.12 after Wenzel et al. [76]. The inset shows $\Gamma$ for the LD heterostructure design as used in set $D^{\mathrm{T_{AR}}}_{\mathrm{oLD}}$. $\Gamma$ has been calculated using as 1D LD simulator.

## 5.6 Summary and conclusions

The influence of the growth temperature on the structural properties and the crystal perfection of the active region as well as LD device characteristics was investigated. Increasing $T_{\mathrm{AR}}$ results in a decrease of the In mole fraction in the quantum wells. As a consequence the emission shifts blue and the material perfection increases. LT-CL investigations suggest lower band gap fluctuations caused by thickness and In mole fraction non-uniformities in the QWs as the temperature increases.

Using a multi-step epitaxial approach it was possible to prepare different heterostructure with identical active regions. Device characterization of optically pumped and current-injection laser reveled an decrease of the gain and an increase of the laser threshold as $T_{\mathrm{AR}}$ decreases. Unfortunately, the conducted experiments allow no direct correlation of the higher threshold with the deteriorated active region material quality. Simulations showed that wavelength dependent waveguide losses result in different modal gain in the samples. Additionally, the intrinsic fields and therefore the oscillator strength varies from sample to sample as a consequence of the different In mole fraction in the quantum wells. In order to clarify the influence of the material quality on the device characteristics a set with identical oscillator strength and modal gain but different material quality is produced and analyzed in the next chapter.

# 6

# Correlation of the active region material perfection with device characteristics

In order to correlate the crystal perfection of the active region with LD characteristics, samples with identical heterostructure layout but a different crystal perfection are produced. In contrast to the previous series, the identical emission wavelength and quantum well layout result in an identical oscillator strength and modal confinement. Since the investigations in chapter 5 revealed a huge influence of the growth temperature on the material quality, the samples were prepared using different $T_{\mathrm{AR}}$. In order to keep the In mole fraction and $d_{\mathrm{QW}}$ constant the In mole fraction in the vapor was adjusted depending on $T_{\mathrm{AR}}$. According to the approach in chapter 5 different MQW and optical pumpable laser structures were grown in order to analyze the influence of $T_{\mathrm{AR}}$ on the material as well as device characteristics.

## 6.1 Sample and growth conditions variation

First, a set $E^{\mathrm{TMIn}}$ of MQW structures of type b) in Fig. 2.1 was grown in the Aix2400G3-HT. $E^{\mathrm{TMIn}}$ consists of different 5× $In_{0.09}Ga_{0.91}N/In_{0.02}Ga_{0.98}N$(:Si) MQW sample with identical quantum well width ($d_{\mathrm{QW}}$) and quantum well (QW) In mole fraction ($x_{\mathrm{QW}}$) but grown using different growth conditions. $T_{\mathrm{AR}}$ was varied between 760°C and 840°C and $x^{\mathrm{In}}_{\mathrm{vapor}}$ between 0.16 and 0.53. Due to minor changes in the growth rate and the enhanced indium segregation from the QW into the barrier at high $T_{\mathrm{AR}}$, the QW growth time had to be adjusted in order to maintain a constant QW thickness. The growth was immediately terminated after the last $In_{0.02}Ga_{0.98}N$(:Si) barrier, and the wafer was cooled to room-temperature in $NH_3$ atmosphere to freeze the surface morphology [112] for later measurements by AFM. $x_{\mathrm{QW}}$ and $d_{\mathrm{QW}}$ were determined by HR-XRD. The luminescence characteristics were analyzed by TD-PL and LT-CL. The varied growth condition of set $E^{\mathrm{TMIn}}$ are noted in Tab. 6.1.

In order to study the properties of the MQWs under conditions of stimulated emission, a series $E^{\mathrm{TMIn}}_{\mathrm{oLD}}$ of laser heterostructures for optically pumped lasing was grown at different $T_{\mathrm{AR}}$. The samples of type c) in Fig. 2.1 were produced using identical active region growth conditions as for set $E^{\mathrm{TMIn}}$. The active regions are identical to set $E^{\mathrm{TMIn}}$ except that the number of QWs was reduced to three. A current-injection laser diode ($E^{\mathrm{TMIn}}_{\mathrm{LD}}$) was later on produced (type d) in Fig. 2.1), using the growth conditions that resulted in the lowest optical threshold power. The growth

scheme and the layer added above the active region are identical to the structures described in section 5.1.

## 6.2 Investigation of the crystal perfection of the MQW samples

### 6.2.1 HR-XRD and PL characterization

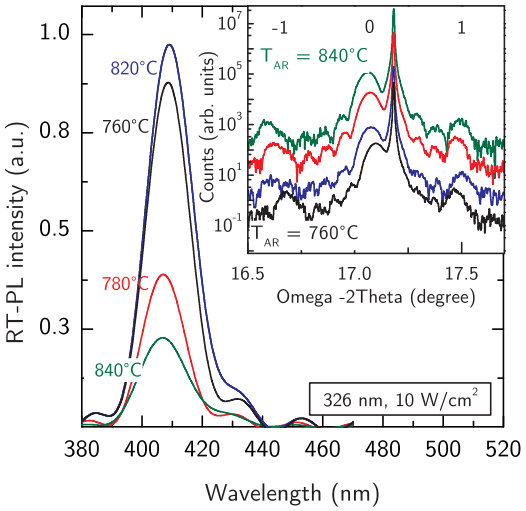


Figure 6.1: PL wavelength of sample set $E^{\mathrm{TMIn}}$ with constant $x^{\mathrm{In}}_{\mathrm{solid}}$. The inset shows the HR-XRD $\Omega - 2\Theta$ scans of the (0002) reflections of the samples with marked -$1^{st}$,$0^{st}$ $1^{st}$ order InGaN layer peak.

Fig. 6.1 displays the RT-PL spectra of sample set $E^{\mathrm{TMIn}}$. All samples show emission with peaks around 405 nm. The In mole fraction and the thickness of both the QWs and the barriers were derived from HR-XRD $\Omega - 2\Theta$ scans around the (0002) reflections on the samples of set $E^{\mathrm{TMIn}}$. The $\Omega - 2\Theta$ scans and their comparison with simulations are shown in the inset of Fig. 6.1. The $\Omega - 2\Theta$ scans exhibit an increasing fringe intensity with increasing $T_{\mathrm{AR}}$ indicating smoother interfaces and/or a superior periodicity. The different separation of the zero and first order super lattice peaks arise from variations of the barrier thicknesses. The maximum deviation of the average QW thickness between the different samples was calculated to be about 0.7 nm. The results are noted in Tab. 6.1.

| | $T_{\mathrm{AR}}$ | $x^{\mathrm{In}}_{\mathrm{vapor}}$ (well) | $x^{\mathrm{In}}_{\mathrm{solid}}$ (well) | $\nu_{\mathrm{In}}$ (well) | $d_{\mathrm{well}}$ (nm) | $x^{\mathrm{In}}_{\mathrm{vapor}}$ (bar.) | $x^{\mathrm{In}}_{\mathrm{solid}}$ (bar.) | $d_{\mathrm{bar}}$ (nm) | RT-$\lambda_{\mathrm{PL}}$ (nm) | RT/10 K (int.) |
|---|---|---|---|---|---|---|---|---|---|---|
| | | | ± 0.01 | | ± 0.5 | | ± 0.01 | ± 0.5 | | |
| 1 | 760 | 0.16 | 0.08 | 0.44 | 3.5 | 0.02 | 0.02 | 9.0 | 408.7 | 0.02 |
| 2 | 780 | 0.20 | 0.08 | 0.38 | 3.4 | 0.02 | 0.02 | 7.0 | 407.2 | 0.001 |
| 3 | 820 | 0.31 | 0.09 | 0.21 | 3.8 | 0.03 | 0.02 | 7.5 | 406.6 | 0.001 |
| 4 | 840 | 0.53 | 0.08 | 0.09 | 3.4 | 0.04 | 0.03 | 7.5 | 409.3 | 0.001 |

Table 6.1: Growth and structural parameters of set $E^{\mathrm{TMIn}}$ as obtained from HR-XRD and PL. $x^{\mathrm{In}}_{\mathrm{solid}}$, $d_{\mathrm{well}}$ and $d_{\mathrm{bar}}$ as well as their accuracies were derived from comparison of the measured and simulated $\Omega - 2\Theta$ scans.

The PL and HR-XRD measurements show only a small variation of the well width, the In mole fraction in the solid and the emission wavelength as $T_{\mathrm{AR}}$ is varied over a wide range. The measurements prove that the adjustment of the TMIn flux and QW growth times result in fairly identical heterostructure layouts in the sample series.

### 6.2.2 AFM characterization

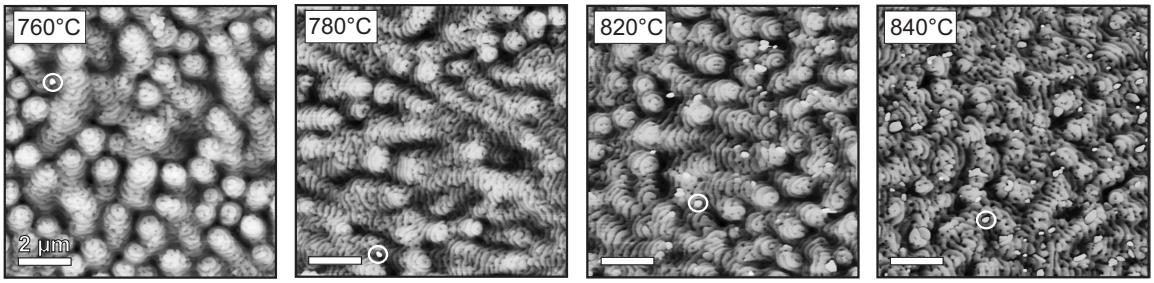


Figure 6.2: AFM images of the surface of the samples of set $E^{\mathrm{TMIn}}$. The white circles mark exemplarily indium droplets. The z-range is 25 nm for all pictures. $T_{\mathrm{AR}}$ is given for each image.

In order to reveal the influence of $T_{\mathrm{AR}}$ and the TMIn supply on the crystal perfection AFM measurements were conducted on set $E^{\mathrm{TMIn}}$. Fig. 6.2 shows the surface morphology of all samples as characterized by AFM topograms. The surface morphology is similar for all $T_{\mathrm{AR}}$ in set $E^{\mathrm{TMIn}}$. In every AFM topogram growth steps with a height of around 1.5 - 2 nm are noticeable. Clearly, the growth edges are wound in growth spirals as observed in section 3.3.2. Furthermore, all topgrams show a high density of dark spots and some white spots. The density of the dark spots is about $1 \times 10^9\,\mathrm{cm}^{-2}$ and correlates well with the threading dislocation density in the GaN template as determined by HR-XRD [70]. Thus, the dark spots most probably represent the decorated threading points of the dislocations. The small bright features change their shape under electron beam excitation in SEM and thus most likely contain excess indium accumulated on the surface.

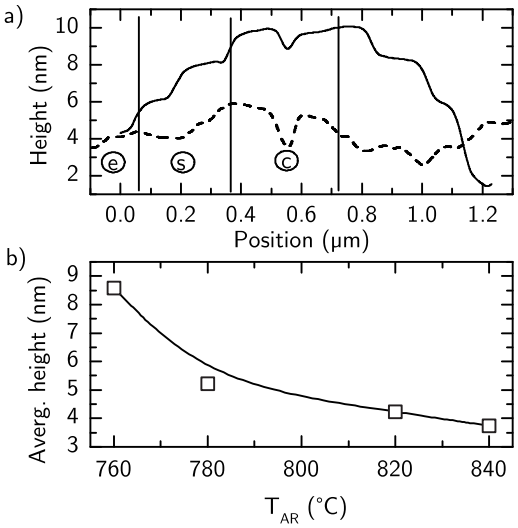


Figure 6.3: a) Height profiles of the growth spirals from sample with $T_{\mathrm{AR}}$ =760 and 840 °C with marked edge (e), side surface (s) and center (c) region. b) Average height of the structures of set $E^{\mathrm{TMIn}}$ derived from the images shown in Fig. 6.2.

Fig. 6.3 a) depicts AFM line scans across an average spiral for the samples grown at highest and lowest $T_{\mathrm{AR}}$ in set $E^{\mathrm{TMIn}}$. The section of the spiral, namely edge (e), side surface (s) and center (c), are marked. The pit in the center region of the spiral is due to decoration of the threading point of the spiral dislocation. As can be seen in Fig. 6.3 b) the average height of the spirals decreases with increasing $T_{\mathrm{AR}}$.

### 6.2.3 Correlation of morphological features with luminescence properties

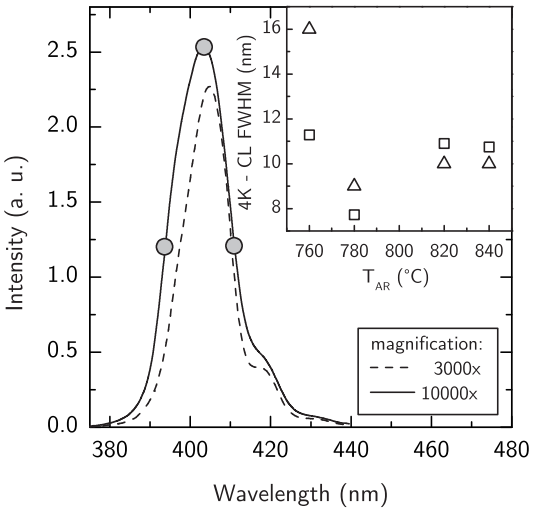


Figure 6.4: Spatially integrated LT-CL-spectra measured at 6 K for 3000× and 10000× magnification for a sample of set $E^{\mathrm{TMIn}}$ with $T_{\mathrm{AR}}$ = 760 °C with scanning LT-CL wavelengths marked. The inset shows the FWHM of the LT-CL-peaks of set $E^{\mathrm{TMIn}}$.

LT-CL measurements at 5.5 K were conducted on set $E^{\mathrm{TMIn}}$ to clarify the influence of the lateral growth rate non-uniformity observed by AFM on the luminescence. Spatially integrated LT-CL spectra were measured at 3000× and 10000× magnification and spatially resolved monochromatic LT-CL images were taken at the peak wavelength and at wavelengths on the high and low energy sides of the LT-CL peak at 10000× magnification (see Fig. 6.4). The inset in Fig. 6.4 summarizes the FWHM values of the LT-CL peaks measured at different magnifications. For the lowest $T_{\mathrm{AR}}$ the FWHM of the LT-CL peak derived from a small area (10000×: area of $8 \times 10\ \mu\mathrm{m}^2$) as well as from a larger area (3000×: area of $30 \times 26\ \mu\mathrm{m}^2$) is highest. A minimum can be found around 780 °C for low as well as high magnification.

Fig. 6.5 shows the scanning LT-CL images for a fixed wavelength for the samples grown at 760 °C and 840 °C of set $E^{\mathrm{TMIn}}$. All LT-CL images reveal a luminescence pattern that can be clearly correlated to morphological features, particularly to the growth spirals observed by AFM (compare Fig. 3.3.2 and Fig. 6.2). The shorter emission wavelength originates from the edge (e) or intersection of the spirals. The side surface (s) emits at the peak wavelength and, therefore, with the highest intensity, whereas the long wavelength part of the spectra originates from the center (c) of the spirals. Regions (c), (s), and (e) are also marked in Fig. 6.3 a). While the lateral distribution of the LT-CL intensity reproduces the pattern of the spirals that have formed during growth, features which could be related to surface pits seen in AFM and SE exhibit a very weak contrast.

AFM and SEM reveal that indium increasingly accumulates at the surface forming indium droplets as $T_{\mathrm{AR}}$ increases. Growth spirals occur at all temperatures with a density of about $3 \times 10^7\ \mathrm{cm}^{-2}$. Their heights are affected by $T_{\mathrm{AR}}$. The spiral height decreases and the terrace width increases with higher $T_{\mathrm{AR}}$ when $x^{\mathrm{In}}_{\mathrm{solid}}$ is kept constant. According to Sugahara et al. [113] the growth velocity of the adhesive mode increases linearly with the driving force $\Delta\mu$ to grow a crystal in the BFC model [66], whereas the velocity for the spiral mode increases with $(\Delta\mu)^2$ and therefore dominates in the low $T_{\mathrm{AR}}$ regime. The increased surface roughness with decreasing $T_{\mathrm{AR}}$ is consistent with the decreased fringe intensity seen in the HR-XRD $\Omega - 2\Theta$ scans (see inset in Fig. 6.1) also indicating rougher interfaces in the QWs grown at low $T_{\mathrm{AR}}$.

Analogous to section 5.3.1 the luminescence properties can be related to the morphology of the samples. Samples grown at low $T_{\mathrm{AR}}$ and $x^{\mathrm{In}}_{\mathrm{vapor}}$ resulting in high growth spirals show a more than 15 nm red-shifted luminescence of the spiral center with respect to the edge whereas samples with lower spirals exhibit a decreased red-shift of about 10 nm due to well thickness fluctuations. Fig. 6.4 shows that the FWHM of the LT-CL spectra does not change monotonically. The luminescence FWHM decreases with the average height of the growth spirals at low $T_{\mathrm{AR}}$ but increases again at high $T_{\mathrm{AR}}$ or high TMIn supply, respectively. At these growth conditions the indium incorporation in GaN is limited on the one hand. But on the other hand, surface diffusion of ad-atoms is thermodynamically promoted and furthermore enhanced due to the high surface concentration of indium acting as a surfactant [114]. Since spi-

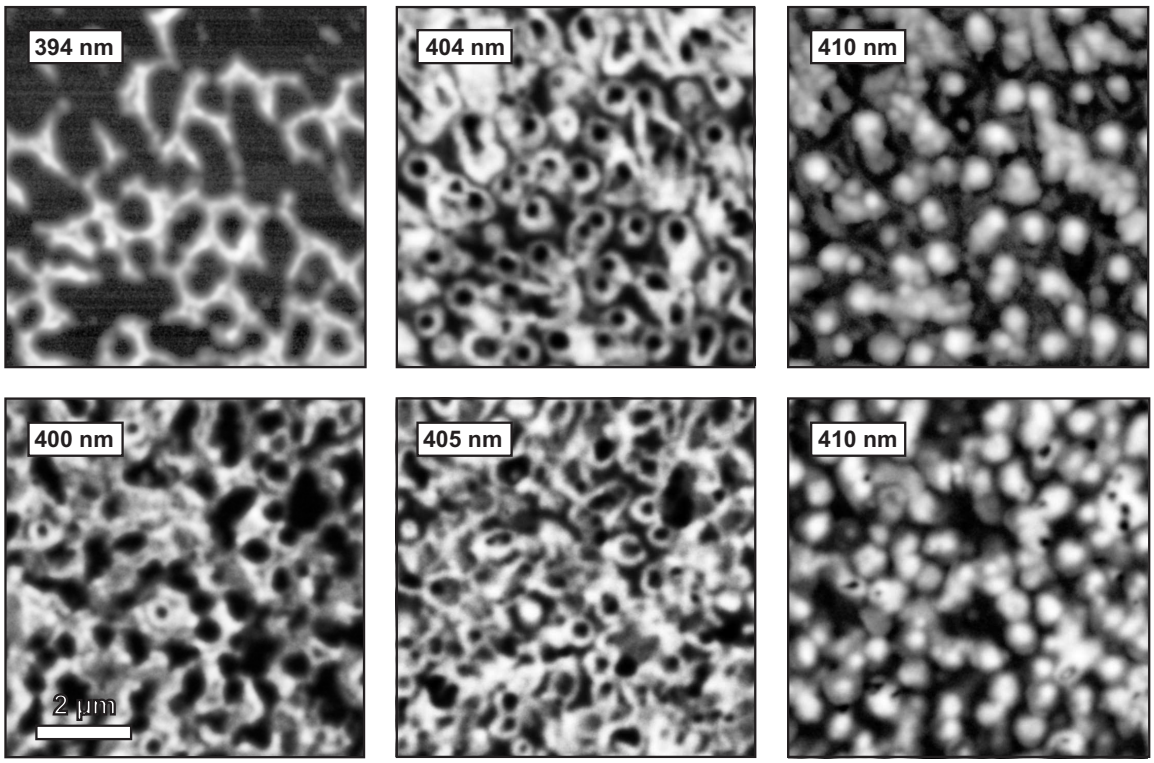


Figure 6.5: Scanning CL images at 5.5 K and fixed wavelength for samples grown at 760 °C (first row) and for 840 °C (second row) of set $E^{\mathrm{TMIn}}$. The wavelengths are noted in the upper left corners.

ral growth and therefore the QW thickness variations are reduced at high $T_{\mathrm{AR}}$, the results suggest that indium concentration fluctuations are causing the broadening of the luminescence at high $T_{\mathrm{AR}}$. This finding is in good agreement with the work of Musikhin et al. [115], who found a spatially inhomogeneous indium incorporation in InGaN films for high TMIn/ TMGa ratios. They showed by TEM that the regions with a higher indium concentration have a spatial extent of about 3 nm and their density increases with increasing TMIn supply.

## 6.3 Influence of the crystal perfection on lasing characteristics

So far, the influence of $T_{\mathrm{AR}}$ on the morphology of the active region and the spatial distribution of the luminescence was discussed. In order to reveal the influence of these parameters on the devices characteristics, optically pumped lasing was studied on the sapphire based samples of set $E_{\mathrm{oLD}}^{\mathrm{TMIn}}$.

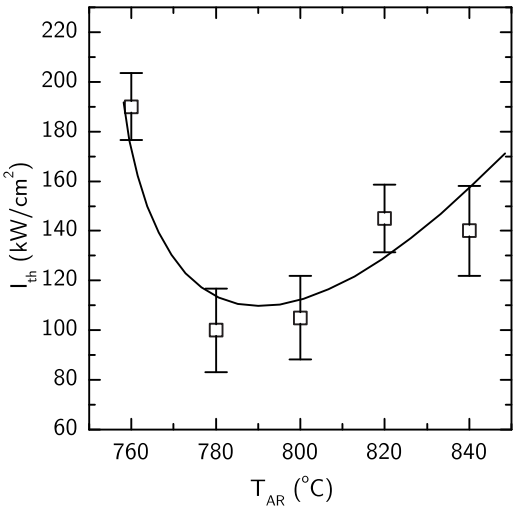


Figure 6.6: $i_{\mathrm{th}}$ for optically pumped lasing of 1000 $\mu$m long laser bars of set $E_{\mathrm{oLD}}^{\mathrm{TMIn}}$. The solid line is a guide for the eye.

Fig. 6.6 shows the threshold power density for stimulated emission measured at room temperature. The $i_{\mathrm{th}}$ is lowest for the MQW grown at 780 °C , whereas it is maximum for $T_{\mathrm{AR}}$ = 760 °C . These two temperatures were shown to be associated with the smallest LT-CL and 10K-PL peak FWHM (780 °C ) and the highest AFM surface roughness (760 °C ), respectively.

The concurrence of the spectrally narrowest luminescence peaks with the lowest lasing threshold suggests that the population density and thus the density of states is largest for the MQWs grown at 780 °C . It is noted that a medium temperature of 780 °C also provides small average height variations on the surface (see Fig. 6.3 a)) indicating low QW thickness variations. The increase of $i_{\mathrm{th}}$ for $T_{\mathrm{AR}}$ = 760 °C illustrates that $i_{\mathrm{th}}$ is strongly affected by the enhanced spiral growth resulting in spatial fluctuations of the luminescence. In contrast to a higher slope efficiency found in LED structures [116] and reduced non-radiative recombination (see Tab.6.1) , we found that an enhanced spiral growth of the active region results in a reduced LD

performance. Moreover, it is concluded that the RT-PL intensity is not a reasonable figure of merit to optimize the growth conditions of a MQW for optimum laser performance, whereas the LT-CL FWHM (see Fig. 6.4) follows the trend of the $i_{\mathrm{th}}$ fairly well.

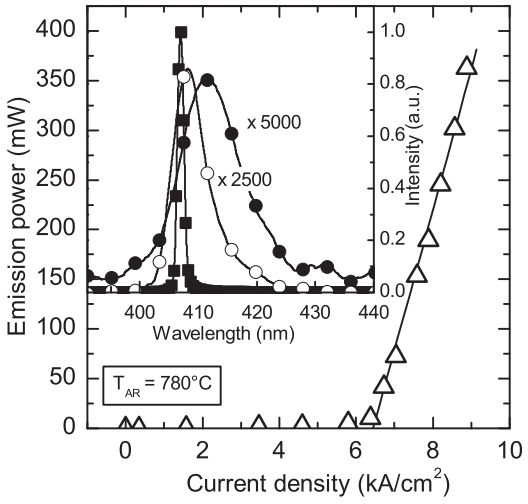


Figure 6.7: P-I characteristic of a sapphire based BA-LD with a 40 $\mu$m wide contact stripe fabricated from sample $E_{\mathrm{LD}}^{\mathrm{TMIn}}$. The growth temperature of the active region was 780°C. The optical output power was determined for a single uncoated facet. The inset shows the emission spectra taken below (circles), at (open circles) and slightly above (filled squares) the threshold, respectively.

The optimum $T_{\mathrm{AR}}$ of 780 °C obtained from the described studies was employed for the fabrication of laser diodes ($E_{\mathrm{LD}}^{\mathrm{TMIn}}$). Fig. 6.7 shows the P-I-characteristic of a laser diode, operated in pulsed mode with a pulse width of 300 ns and a repetition rate of 1 kHz. The inset in Fig. 6.7 shows the emission spectra taken below, at and slightly above the threshold. They exhibit a spectral narrowing of the emission above the lasing threshold. From the P-I-characteristic an onset of laser operation can be derived at a current density of about 6.5 kA/cm$^2$ for the 40 $\mu$m wide device when current spreading is neglected.

### 6.3.1 Summary and conclusions

By variation of $T_{\mathrm{AR}}$ and accordingly adjusting the TMIn supply during QW growth it was possible to realize samples with different material perfection of the active region but identical heterostructure layout and emission wavelengths around 400 nm. The experiments revealed a huge sensitivity of the crystal perfection to the varied growth conditions. Increasing the temperature and In mole fraction reduces interface roughness of the MQW since spiral growth is suppressed. The spatial band gap non-uniformities decrease up to a certain temperature. It is believed, that for very high temperatures the increase of spatial In mole fraction variations in the solid results in an increase of the band gap non-uniformities.

By reproducing the MQW sample as optically pumpable structures the influence of the material perfection of L-I-characteristics was revealed. The growth conditions that result in the lowest spectral width of the luminescence of the MQW sample also exhibit the lowest threshold for stimulated emission of the optically pumpable samples. It is assumed that this growth conditions provide the best compromise between the two counteracting trends of spatial well thickness variations and indium

concentration non-uniformities. The investigations in this section furthermore showed that band gap uniformity is crucial for highly efficient LDs emitting around 400 nm. It turns out that the spectral width of the luminescence is a good figure of merit when optimizing the growth conditions of the active region.

The achieved $i_{\mathrm{th}}$ of 6.5 kA/cm$^2$ for the sapphire based BA-LD is higher than the values published by the leading groups [117, 118, 119], which are in the 1.5-4 kA/cm$^2$ range. Although a direct comparison of the characteristics is not straight forward due to different device setups, e.g. cavity length and contact width, lower laser threshold power densities are in general realized by the growth on GaN substrates with lower defect densities and better cleaveability of the facets. A further reduction of the threading dislocation densities and thus the $i_{\mathrm{th}}$ is possible by epitaxial lateral overgrowth (ELO) growth technique [120] on both sapphire and GaN substrates. Beside the growth optimization of the InGaN quantum structures [121, 122, 123, 124, 125, 126] the adjustment of the heterostructure, e.g. spacing between MQW and EBL [127], EBL material [128], EBL doping [45], proved to have a major influence on the opto-electrical properties of the device. In order to optimize these parameter it is necessary to both simulate and prepare / characterize sets of current injection LDs.

# 7

# Extending the wavelength to 450 nm

In the previous chapters the influence of the epitaxial processes, the heterostructure layout and the growth parameter on the device characteristics of LDs emitting around 400 nm were discussed. It turned out that spatial homogeneity of the material parameters in the active region results in a high peak gain and therefore a low threshold current density of the device. The main cause for band gap non-uniformities are local variations of the quantum well growth rate and the indium incorporation due to spiral growth around threading dislocations. On sapphire based GaN templates the winding up of the growth edges locally increases the growth rate in the center of the spiral. Furthermore, the distances between the growth edges on the sidewalls of the spirals is reduced in comparison to the layer by layer growth mode. Due to the higher In incorporation at the growth edges the sidewalls exhibit a higher In mole fraction in the solid resulting in lateral thickness as well as In mole fraction non-uniformities. Experiments at different active region growth temperatures showed that the bandgap non-uniformities increase as the growth temperature decreases.

Red-shifting the LD emission to 450 nm requires a higher In mole fraction in the quantum wells in order to lower the band gap energy. A higher In mole fraction in the QW is achieved by a reduction of the active region growth temperature and is accompanied with a degradation of the crystal quality in the active layer as described above. Additionally, the piezoelectric field strength increases as the strain of the QW increases. As a consequence of the different piezoelectric properties of GaN and InGaN [28] the oscillator strength and therefore the material gain is reduced for high In mole fraction in the QWs. The third challenge at larger wavelengths is to maintain sufficient optical confinement of the mode. As the wavelength of the mode increases the difference of the refractive indices between the waveguiding and the cladding layer is reduced. As a consequence the optical mode is less confined and the modal gain is reduced.

In summary the following aspects need to be considered: First, how can the reduced material gain due to a lower crystal perfection of the active region and a lower overlap of the wave functions be compensated? Secondly, what heterostructure layout changes are necessary to realize sufficient modal gain at longer wavelengths? In the following section the improvement of the crystal perfection by transferring the growth to GaN substrates is addressed. Later on, it will be described how the waveguiding layout is adjusted in order to increase the modal gain. After that, the

active region heterostructure as well as growth condition modifications with the aim to improve the material peak gain are discussed.

To distinguish between the influence of heterostructure variations on the material as well as the modal gain the optimization scheme was changed in this chapter. In order to reveal the influence of heterostructure parameter variations on the device characteristics 1D self-consistent device simulations (SILENSe,LASTIP) were conducted first. After that the results were verified by preparing optically pumpable LD samples. Beside the determination of the device characteristics the material perfection was evaluated according to Sec. 6.2.3.

## 7.1 Transferring the growth process from sapphire-based templates to GaN substrate

Dislocations in GaN work as non-radiative recombination centers and therefore reduce the material gain of a LD structure. Moreover, it was shown in Sec. 3 that the threading points of the dislocations pin the growth edges and change the growth mode from layer by layer to spiral growth. The consequential lateral non-uniformity of the growth rate as well as In mole fraction of the QW was identified in Sec. 6 as a primary cause for the increase of the optical threshold power density. In order to reduce pinning of the growth edges at dislocations the growth is transferred from sapphire based GaN templates (TDD $\sim$ 1-10 $\times$ $10^9$ $cm^{-2}$) to GaN substrate (TDD $\sim$ 1-5 $\times$ $10^7$ $cm^{-2}$).

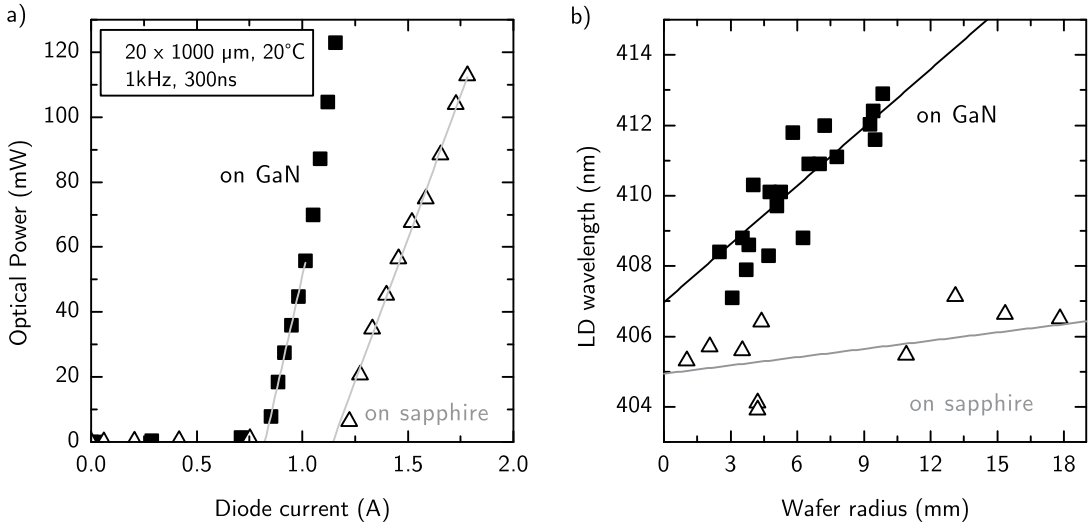


Figure 7.1: a) P-I characteristics of LD heterostructures deposited on either a GaN substrate or a sapphire-based GaN template (samples $F_{\mathrm{LD}}^{\mathrm{sapph./GaN}}$). b) Corresponding variation of the LD wavelength across the wafer.

When changing the substrate material one has to deal with the different material properties during epitaxy. For instance the different thermal expansion coefficients of the materials result in different wafer bowing behavior. This in turn changes the temperature distribution on the wafer surface. As shown in Fig. 5.1 $T_{\mathrm{AR}}$ affects the

emission wavelength by changing the In incorporation and distribution in the active region. The wavelength on the other hand influences the modal gain (see section 5.5) and hence the opto-electric device properties. Fig. 7.1 shows the P-I characteristics and the LD wavelength variation across the wafer for a GaN and a sapphire based LD. Whereas LDs on GaN substrate feature a lower threshold current and a higher slope efficiency the structure deposited on sapphire exhibits a lower spatial variation of the wavelength across the wafer. The wavelength shift across the wafer is determined among others by the spatially different In mole fraction in the QWs. Such non-uniformities occur due to local variations of the In supply or the In incorporation into InGaN. On the supply side optimized flow conditions [129, 130] and nitrogen as carriers gas [131] are commonly used to achieve a homogeneous composition across the wafer. The interplay of precursor depletion in the gas phase and averaging by wafer rotation in a planetary reactor [132] provides a homogeneous supply across the wafer. Once the In is on the growth surface the incorporation is determined by the temperature on the wafer surface as has been discussed in Sec. 5.

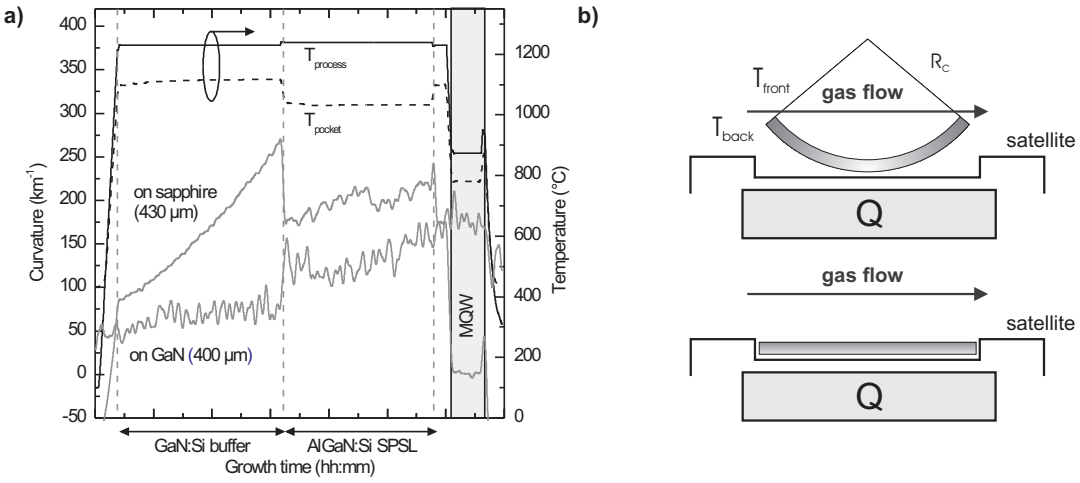


Figure 7.2: a) Curvature and temperature transients during deposition of the n-side and the AR a 405 nm LD heterostructure grown on different substrates (samples $G^{\text{sapph./GaN}}$). b) Schematic of the different bowed wafer in the satellite during deposition of the active region.

Fig. 7.2 a) shows the curvature and temperature transients during the growth of the n-side and the AR of 405 nm LD heterostructures. The sample structure of type b) in Fig 2.1 involves a tensily stressed AlGaN cladding layer underneath the AR to confine the optical mode. In an epi-layer on substrate system as described by Stoney [39], the stress results in a concave wafer curvature, if a flat substrate is used at the start. As a consequence of the non-uniform thermal coupling of the curved wafer with the hot satellite the surface temperature decreases at the edges (see Fig. 7.2 b)). On a GaN wafer in this regions the In mole fraction in the QWs is enhanced and the corresponding emission wavelength is red-shifted. As shown in Fig. 7.2 a) the sapphire wafer curvature during active region growth can be fairly low as the tensile stress from the AlGaN cladding layer is partially compensated by the thermally induced compression of the substrate during cool down to the AR growth

temperature. The effect can be utilized to maximize the yield, e.g. the number of identical devices grown by a single run, during the growth of sapphire based LEDs.

In order to reveal the influence of the substrate material on the surface temperature quantitatively the wafer curvature ($\kappa$), $T_{\mathrm{pocket}}$ and $T_{\mathrm{surface}}$ are directly measured during growth. The results are correlated with the PL distribution across the wafer obtained after growth. Furthermore, the effects of the growth conditions on vertical and lateral temperature profiles are studied with the aim to improve the lateral wavelength homogeneity on a GaN substrate.

### 7.1.1 Sample variation

First, a sample $H^{\mathrm{sapph.}}$ of type b) (see Fig 2.1) that corresponds to the n-side of a laser structure was grown in the Aix2400G3-HT. Since $H^{\mathrm{sapph.}}$ features all layers that define the stress state and hence the curvature during AR deposition this structure is used to investigate the influence of growth parameters on the vertical and lateral surface temperature profiles during QW deposition. Employing the optimized growth conditions, that result in a homogeneous surface temperature distribution, sample $H^{\mathrm{sapph.}}$ was reproduced both on a sapphire and a GaN substrate with an AR on top. The complete structure additionally features a 200 nm thick GaN:Si wave guide and a MQW consisting of two 1.75 nm thick $In_{0.15}Ga_{0.85}N$ QWs separated by 4.5 nm thick $In_{0.05}Ga_{0.95}N$ barriers. In order to prevent surface effects on the PL measurements the AR was capped with 10 nm n.i.d. GaN. The structures are denoted as $I^{\mathrm{sapph.}}$ and $I^{\mathrm{GaN}}$, respectively.

### 7.1.2 Determination of the wafer surface temperature

Using the EpiCurveTT sensor on the Aix2400G3-HT machine only the pocket temperature and the wafer curvature is measured. Since GaN and sapphire are transparent for the 950 nm emission used for the pyrometric temperature determination, the temperature of the emitting satellite is determined rather than the wafer temperature. Using the effect that GaN absorbs and hence also emits at growth temperature at wavelengths upto 400 nm, the temperature of the GaN surface can be determined by measuring the pyro-radiation in this wavelength region. In order to detect the 400 nm pyro-radiation the growth experiments were repeated with a Pyro400 system mounted instead of the EpiCurveTT system detecting at 950 nm.

The in-situ temperature and curvature transients of sample $H^{\mathrm{sapph.}}$ are shown in Fig. 7.3. Since a template is used the curvature changes from -50 $\mathrm{km}^{-1}$ convex to 15 $\mathrm{km}^{-1}$ concave when heating up to GaN growth temperature. The change can be attributed to two effects, the different temperatures at the frontside and the backside of the wafer and the different thermal expansion coefficients of the materials of this layer-on-substrate system. Since the wafer is heated from the backside, the temperature difference between the frontside and the backside of the wafer increases as the temperature increases. For example, the curvature of the plain sapphire wafer changes by $\sim$30 $\mathrm{km}^{-1}$ during heating for the template production (not shown here).

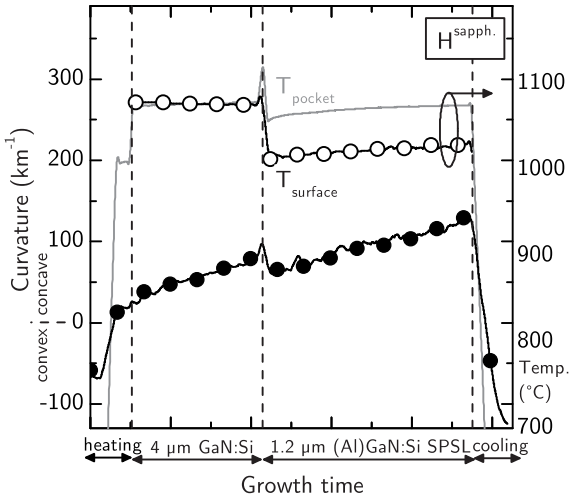


Figure 7.3: Curvature (filled circles) and temperature (open circles) of sample $H^{\text{sapph.}}$ measured during growth. The grey line represents the temperature of the pocket.

The curvature increase is even higher if a GaN epi-layer, with a lower thermal expansion coefficient in comparison to sapphire, is on top of the sapphire. During the deposition of the 4 $\mu$m thick GaN:Si the curvature increases from 15 to 90 km$^{-1}$. This effect is due to the different in-plane GaN lattice constants in the template and the silicon-doped GaN:Si buffer in sample $H^{\text{sapph.}}$ [41]. During deposition of the GaN:Si buffer only a small offset between the wafer surface temperature and the temperature of the pocket is measured. When changing to AlGaN cladding layer growth conditions the difference between $T_{\text{surface}}$ and $T_{\text{pocket}}$ increases. For AlGaN deposition the reactor pressure is reduced from 600 mbar for GaN growth to 60 mbar to minimize parasitic pre-reactions between TMAl and $NH_3$ in the gas phase [37]. The curvature change during deposition of the 1.2 $\mu$m thick AlGaN(:Si) SPSL increases to $\sim$60 km$^{-1}/\mu$m in comparison to $\sim$12 km$^{-1}/\mu$m for GaN:Si growth. The higher curvature change is due to the lattice mismatch between the AlGaN and the GaN. According to Brunner et al. [41] the curvature change corresponds to an aluminum mole fraction of 0.06. HR-XRD RSM around the $(10\bar{5})$ reflection of sample $H^{\text{sapph.}}$ (not shown here) confirms that the AlGaN is pseudomorphically grown with an average aluminum mole fraction of $\sim$0.06.

### 7.1.3 Influence of growth conditions on the wafer surface temperature

In order to examine the influence of the growth conditions on the wafer surface temperature more closely, sample $H^{\text{sapph.}}$ was heated in a separate experiment. At reactor pressures of 400, 200, 100, and 50 mbar the satellite rotation flow and the total flux were accordingly varied by a factor of two. As can be seen in Fig. 7.4 a) a decreasing reactor pressure as well as an increasing satellite rotation flow reduce the pocket temperature due to a change of the satellite flight height. Changing the total flux by a factor of two was found to have no influence on the pocket temperature. Interestingly, the wafer curvature is lower at higher temperatures. $\kappa$ decreases from 50 to 30 km$^{-1}$ as the reactor pressure or respectively temperature increases. This effect can be explained by a lower vertical temperature gradient in the wafer at

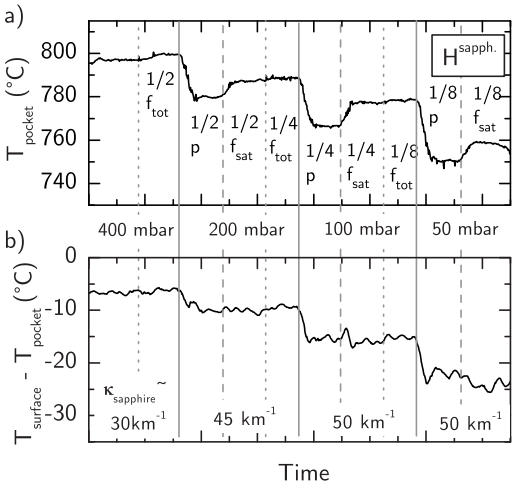


Figure 7.4: a) Transient of the wafer pocket temperature of sample $H^{\text{sapph.}}$ when changing the growth conditions. The grey lines represent the reduction by a factor two of the total flux ($f_{\text{tot}}$ - dotted line), the $p_{\text{reactor}}$ (solid line) or the satellite rotation flux ($f_{\text{sat}}$ - dashed line), respectively. b) Temperature difference between the wafer surface and the pocket corresponding to the transients shown in a). The temperatures are measured in the center of the wafer or satellite, respectively.

higher reactor pressures. As can be seen in Fig. 7.4 b) the wafer surface temperature is affected even stronger than the pocket temperature by the change of the reactor pressure. E.g. decreasing the reactor pressure from 400 mbar to 50 mbar decreases the pocket temperature by 50 K but the wafer surface temperature decreases by 75 K.

Since the difference between pocket temperature and wafer surface temperature is not affected when changing the satellite rotation or total flux, the variations shown in Fig. 7.4 b) can not be attributed to different satellite flight heights or cooling by the carrier gas, respectively. Rather, the reduced thermal conductivity of the gas at low reactor pressure decreases the thermal coupling of the wafer backside with the hot satellite. Since the wafer is transparent for the thermal radiation and the contact area between wafer and satellite is rather small, heat radiation and conduction are negligible. For a 2 inch wafer a curvature of $30\,\text{km}^{-1}$ corresponds to a bow of around $10\,\mu$m. Furthermore, due to the wafer bow and the roughness of the pocket or respectively the wafer backside, the wafer has only punctuated contact with the satellite. A good estimation of the gap between the satellite surface and the backside of the wafer is $10\,\mu$m. At a low reactor pressure of 50 mbar the Knudsen number (ratio of mean free-path length to characteristic reactor dimension determined by the wafer-satellite gap) is as high as 0.6 in comparison to 0.07 at 400 mbar. In this regime the thermal conductivity and molecular viscosity of the gas between satellite and wafer backside decrease as the pressure decreases. As a consequence of the reduced thermal conductivity the wafer temperature decreases with respect to the temperature of the pocket at low reactor pressures.

### 7.1.4 Improvement of the lateral surface temperature uniformity

In order to investigate which growth conditions result in the highest spatial temperature uniformity temperature line scans across the wafer $H^{\text{sapph.}}$ were measured at 400 mbar reactor pressure at various temperatures. Here it was exploited that the wafer translates under the viewport such that the pyrometry signals at 950 and 400 nm can be measured across the pocket. Fig. 7.5 shows the line scans of the wafer

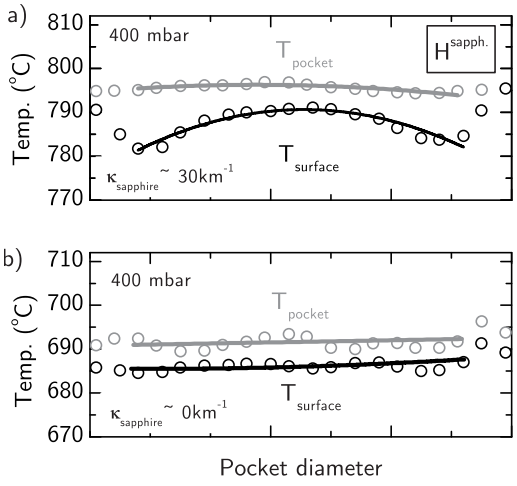


Figure 7.5: Pocket temperature (grey line) and the wafer surface temperature (black line) across the wafer of sample $H^{\text{sapph.}}$ at MQW growth conditions but at different temperatures. The curvature of the wafer is 30 $\text{km}^{-1}$ (a) or 0 $\text{km}^{-1}$ (b), respectively. The solid lines in (a) and (b) are guides to the eye.

surface and the pocket temperature for sample $H^{\text{sapph.}}$ at MQW growth conditions but different temperatures. The wafer curvature corresponding to Fig. 7.5 b) is 0 $\text{km}^{-1}$ resulting in an almost uniform temperature distribution across the wafer. Raising the reactor temperature by 100 K reduces the uniformity of the surface temperature as shown in Fig. 7.5 a). In this latter case the wafer curvature has increased to 30 $\text{km}^{-1}$ due to the higher thermal expansion coefficient of the sapphire substrate with respect to the epi-layer. The concave bow reduces the thermal coupling of the wafer edge to the hot susceptor which reduces the surface temperature in this area by 10 K.

### 7.1.5 Reducing the wafer curvature of GaN substrates

Since the wafer curvature has been shown to strongly affect the temperature uniformity of the wafer surface and as consequence the wavelength uniformity across the wafer a strategy to reduce the wafer bow for GaN substrate is needed. On a GaN substrate the curvature can not be tuned by the growth temperature because of the small differences of the thermal expansion coefficients between substrate and epitaxial layer. The reactor pressure has been shown to affect the wafer curvature in the range of some 10 $\text{km}^{-1}$. This effect is far too small to compensate wafer curvatures between 100 and 150 $\text{km}^{-1}$ during AR deposition on 400 to 300 $\mu$m thick GaN substrates.

An alternative method to reduce the wafer curvature is the usage of higher substrate thicknesses and strain compensating InGaN layer. Fig. 7.6 shows the influence of the GaN substrate thickness on the wafer bow. Using a simulation based on the models by Brunner et al. and Feng et al. [41, 133] the substrate thickness dependency of the wafer curvature is calculated. As shown in the simulations in the inset of Fig. 7.6 the wafer curvature during AR deposition is very sensitive to the substrate thickness. Increasing the substrate thickness from 250 $\mu$m to 1 mm the wafer curvature is nearly zero during AR growth.

The experimental data in the inset of Fig. 7.6 correspond to a heterostructure with a 200 nm thick $In_{0.02}Ga_{0.98}N$ wave guiding layer in order to compensate for the tensile stress coming from the $Al_{0.12}Ga_{0.88}N$ / GaN:Si SPSL cladding layer. By this

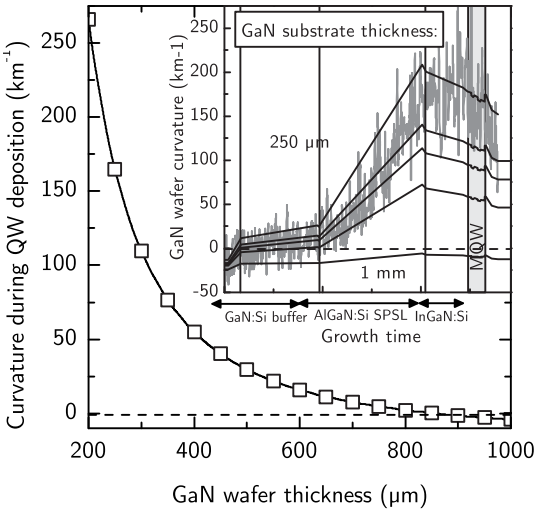


Figure 7.6: Simulation of the GaN substrate thickness dependency of the wafer curvature during AR deposition. The inset shows simulated wafer curvature transients for the deposition of the n-side of the LD structure including the AR with a stain compensating InGaN wave guiding layer. The grey line corresponds to experimental data (300 $\mu$m thick GaN).

the wafer curvature is theoretically reduced by 50 km$^{-1}$ depending on the substrate thickness.

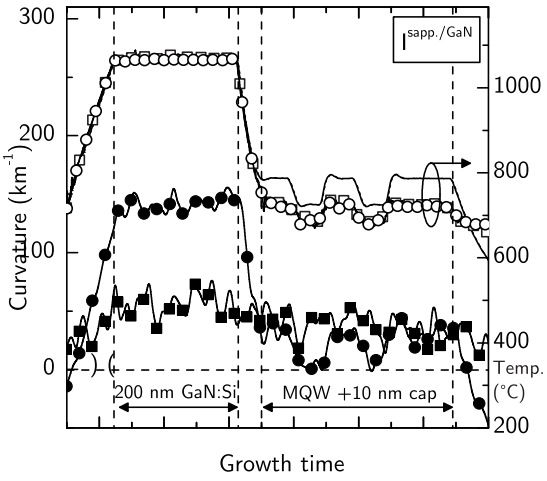


Figure 7.7: Curvature and temperature of samples $I^{\text{sapph.}}$ and $I^{\text{GaN}}$ measured during growth. The temperatures of the pockets are identical (grey line) while the surface temperature on the sapphire wafer (open circles) is higher than that on the GaN wafer (open squares). Curvature transients for the sapphire based (filled circles) and the GaN substrate based wafer (filled squares) are shown at the bottom of the graph. Both wafers are nearly flat at QW growth temperature.

Another approach to circumvent the non-vanishing curvature on the GaN substrate is the epitaxy on as delivered convexly pre-curved substrates. To obtain a flat wafer during active region deposition the pre-curvature needs to be in the range of the curvature change during layer deposition prior to active region deposition. To predict the wafer curvature the model mentioned above is used. Fig. 7.7) shows the curvature and surface temperature transients during growth of samples $I^{\text{sapph.}}$ and $I^{\text{GaN}}$. Sample $I^{\text{GaN}}$ is grown on a convexly 150 km$^{-1}$ pre-bowed GaN whereas sample $I^{\text{sapph.}}$ is grown on a sapphire based GaN template using an initially flat sapphire substrate. At a reactor pressure of 400 mbar a QW deposition temperature was used at which the sapphire wafer is almost flat (see Fig. 7.5 b)). Since the pre-curvature of the GaN substrate is compensated in sample $I^{\text{GaN}}$ by the deposition of the tensily stressed AlGaN, both wafers are almost flat during deposition of the QWs (see Fig. 7.7). Due to the spatially uniform temperature profile the In incorporation in the QWs is very homogeneous across the wafer. To quantify the uniformity PL line scans

across the wafer are measured (see Fig. 7.8). By using a convexly pre-curved substrate the standard deviation of the wavelengths across the 2" wafers is reduced to approximately 3.5 nm at 500 nm for both substrates. In contrast the deposition of a 405 nm LD strcuture on flat substrates results in a standard derivation of around 15 nm on the GaN substrate.

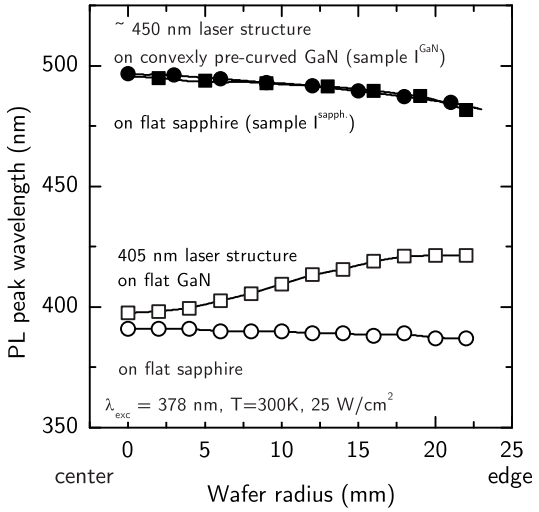


Figure 7.8: Wafer radius dependency of the RT-PL peak wavelength for samples $I^{\text{sapph.}}$ on a flat sapphire substrate (full circles) and $I^{\text{GaN}}$ on a convexly pre-curved GaN substrate (full squares). The excitation wavelength was $\lambda_{exc}$ = 378 nm (25 W/cm). The open symbols correspond to samples ($G^{\text{sapph./GaN}}$) with initially flat GaN (open squares) and sapphire substrate (open circles), respectively.

### 7.1.6 Summary and conclusions

Transferring the growth from sapphire-based GaN templates to GaN substrates one has to deal with a different wafer bow during AR deposition. The wafer curvature has a strong impact on the wavelength homogeneity of InGaN based light emitters due to the strong temperature dependence of the In incorporation. Using in-situ curvature measurements and pyrometry the lateral and vertical temperature distribution across the wafer and on wafer bow on sapphire and GaN substrates was quantitatively determined. In order to improve the temperature uniformity across the wafer one has to increase the reactor pressure. Total flow and satellite rotation were found to have no impact on the lateral temperature uniformity. To compensate for the strain of the AlGaN cladding layer higher GaN substrate thicknesses, pre-curved GaN substrates proved favorable. A convex pre-curvature in the range of the curvature change until active deposition is required for a lateral uniform luminescence distribution on GaN substrate. A model is used to predict the substrate and heterostructure dependent wafer bow during active region deposition. By this it is possible to determine the appropriate wafer pre-curvature and choose a wafer from the as-delivered differently pre-curved substrates.

## 7.2 Adjustment of waveguiding for blue LDs

The emission of LDs is red-shifted by increasing the In mole fraction in the QWs as described in chapter 5. Beside the issue of the InGaN material deterioration the

decrease of the modal gain due to less confinement of the optical mode at longer wavelengths was described (see section 5.4).

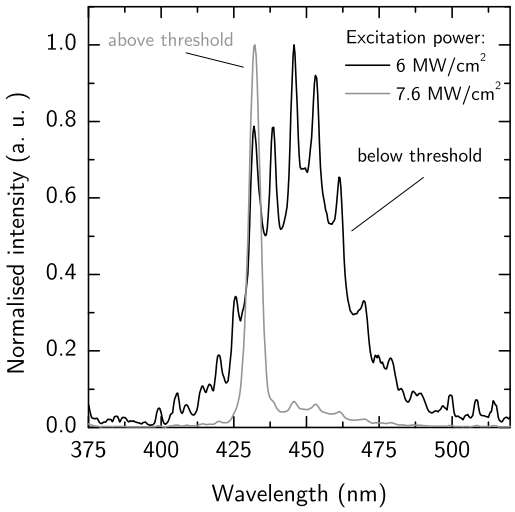


Figure 7.9: Emission spectra from optical pumping below and above the optical threshold power for amplified stimulated emission in optically pump-able laser structure $J_{\mathrm{I}}^{450\,\mathrm{nm}}$.

Fig. 7.9 shows the luminescence spectra of an early optical pumpable laser structure emitting in the blue wavelength region ($J_{\mathrm{I}}^{450\,\mathrm{nm}}$). The cladding and wave guiding structure of this optically pumpable structure is identical with the 405 nm laser layout. Clearly, the spectrum below the optical threshold power density shows multiple fringes corresponding to multiple vertical modes in the structure. Above threshold the structure emits at a blue-shifted wavelength associated with lower wave guiding losses. The high optical threshold power density of about 8 MW/cm$^2$ in comparison to around 150 kW/cm$^2$ for the 405 nm structure also indicates insufficient gain in the structure.

In this section the focus is on the optimization of the wave guiding structure in order to reduce the mode leaking into the substrate. It will be discussed how the cladding and wave guiding layers derived from the 405 nm laser heterostructure need to be adjusted in order to realize low optical threshold power densities at wavelengths around 450 nm.

### 7.2.1 Influence of cladding layer aluminum content and thickness

The amplification of a planar wave when passing through an absorbing material with an optical absorption coefficient ($\alpha$) is described by the gain $g$=-$\alpha$. Because only a part of the vertical intensity pattern of the optical mode overlaps with the gain region of the laser, $g_{\mathrm{mod}}$=$\Gamma g$ is defined. The intensity of the mode is reduced due to several effects. In the case of nitride based materials such waveguiding losses are primarily due to modes leaking into the underlying GaN buffer layer (see Sec. 5.4) and sub-band gap absorption in the p-type doped layer [46]. In order to quantify the mode leakage, the optical gain as a function of the n-cladding layer thickness and aluminum (Al) mole fraction in the solid is simulated.

Fig. 7.10 shows $g_{\mathrm{mod}}$ in dependence of the Al mole fraction and the thickness for the standard 405 and 450 nm structure with identical wave guiding layer and cladding

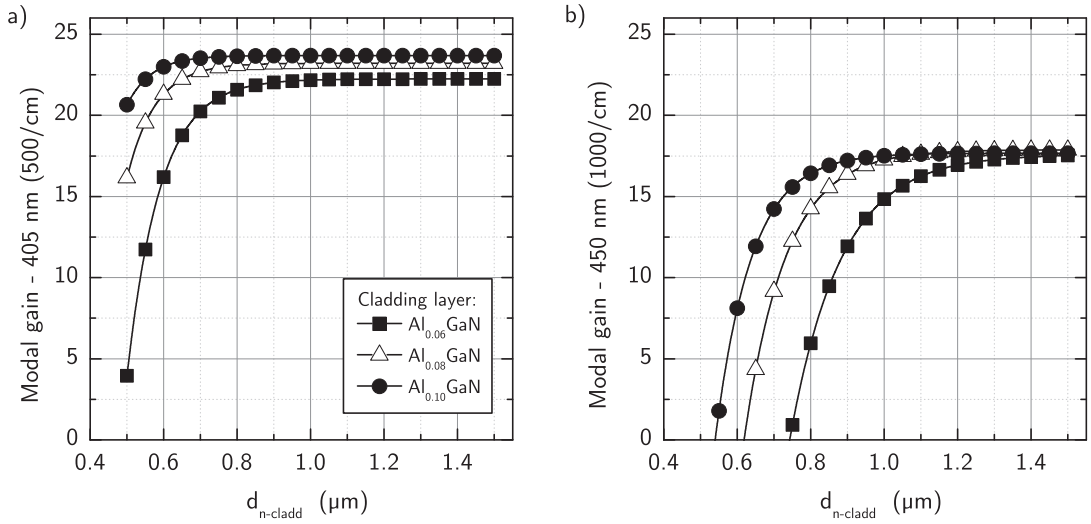


Figure 7.10: Simulation of $g_{\mathrm{mod}}$ for the standard 405 nm wave guiding structure for emission wavelength of 405 (a) or 450 nm (b) as a function of the cladding layer thickness and Al mole fraction in the solid. A different material gain of 500 and 1000 $\mathrm{cm}^{-1}$ was used in order to compensate the influence of the different well width (see Tab. 7.1) of the 405 (3.5 nm) or 450 nm (1.75 nm) structure on $g_{\mathrm{mod}}$, respectively.

layer. The active region of the 450 nm structure has In mole fractions in the QWs of 0.15 and 0.05 in the barriers. The well thickness in the simulation was adjusted to 1.75 nm in order to increase the oscillator strength.

First the simulation of $g_{\mathrm{mod}}$ for the 405 nm structure is discussed: The modal gain exhibits a strong sensitivity to the Al mole fraction in the solid for thin n-cladding layer thicknesses. Such structures exhibit a non-vanishing electric field strength of the mode in the buffer layer. The leakage of the mode is reduced as the Al mole fraction in the solid and hence the refractive index difference between the GaN waveguiding and the cladding layer increases (see Fig. 5.5). The improved confinement of the mode results in a higher electric field strength in the active region and therefore higher modal gain of the structure. For n-cladding layer thicknesses above 0.8 $\mu$m the intensity of the mode in the buffer is negligible. Such structures do not significantly benefit from an increase of the Al mole fraction in the solid .

To quantitatively compare the modal gain of the 450 and 405 nm structure an identical material gain was assumed for both structures. Additionally, $g_{\mathrm{mod}}$ was normalized to the well width in order to eliminate the well-width dependency of the modal gain. Clearly, the 450 nm structure exhibits a lower modal gain for all Al mole fractions and thicknesses of the cladding layer. For 450 nm emission wavelength the intensity of the mode in the cladding layer is higher than for 405 nm emission. The corresponding lower intensity in the AR is due to a lower effective refractive index difference between cladding and wave guiding layer (see Fig. 5.5) at this wavelength. Secondly, the structures show a high sensitivity to the Al mole fraction in the solid for n-cladding layer thicknesses up to 1.2 $\mu$m. Due to the high intensity of the mode in the cladding layer mode leakage occurs for smaller thicknesses. In order to achieve an identical $\Gamma$ using an Al mole fraction in the cladding layer of 0.06 and 0.10 the

| | | **405 nm** | | | | **450 nm** | | | |
|---|---|---|---|---|---|---|---|---|---|
| | Mat. | x | y | d (nm) | Dop. ($cm^{-3}$) | x | y | d (nm) | Dop. ($cm^{-3}$) |
| Cap | GaN | | | 20 | $5\times10^{17}$ | | | 20 | $5\times10^{17}$ |
| CL | AlGaN | 0.12 | | 2.5 600 | $2\times10^{17}$ | 0.12 | | 2.5 600 | $2\times10^{17}$ |
| | GaN | | | 2.5 | $2\times10^{17}$ | | | 2.5 | $2\times10^{17}$ |
| WGL | GaN | | | 80 | $2\times10^{17}$ | | | 80 | $2\times10^{17}$ |
| EBL | AlGaN | 0.2 | | 10 | $2\times10^{17}$ | 0.2 | | 10 | $2\times10^{17}$ |
| WGL | GaN | | | 10 | | | | 10 | |
| barrier | InGaN | | 0.02 | 7.5 | | | 0.05 | 7.5 | |
| well | InGaN | | 0.08 | 3.5 | | | 0.15 | 1.75 | |
| barrier | InGaN | | 0.02 | 7.5 | $-1\times10^{18}$ | | 0.05 | 7.5 | $-1\times10^{18}$ |
| well | InGaN | | 0.08 | 3.5 | | | 0.15 | 1.75 | |
| barrier | InGaN | | 0.02 | 7.5 | $-1\times10^{18}$ | | 0.05 | 7.5 | $-1\times10^{18}$ |
| well | InGaN | | 0.08 | 3.5 | | | 0.15 | 1.75 | |
| barrier | InGaN | | 0.02 | 7.5 | $-1\times10^{18}$ | | 0.05 | 7.5 | $-1\times10^{18}$ |
| WGL | GaN | | | 100 | $-5\times10^{17}$ | | | 100 | $-5\times10^{17}$ |
| CL | AlGaN | 0.12 | | 2.5 1200 | $-2\times10^{18}$ | 0.12 | | 2.5 1200 | $-2\times10^{18}$ |
| | GaN | | | 2.5 | $-2\times10^{18}$ | | | 2.5 | $-2\times10^{18}$ |
| buffer | GaN | | | 3000 | $-3\times10^{18}$ | | | 3000 | $-3\times10^{18}$ |
| 430 $\mu$m sapphire substrate | | | | | | | | | |

Table 7.1: Heterostructure layout for the 405 and 450 nm LD (first approach).

caldding layer thickness has to be 1.2 and 0.75 $\mu$m, respectively.

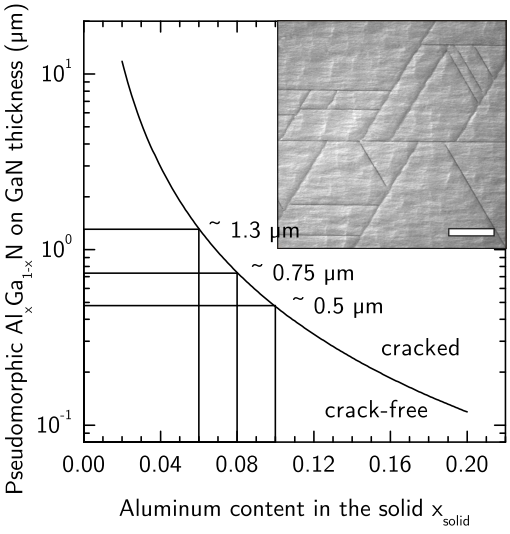

Figure 7.11: Calculation of the critical layer thickness for the onset of cracking as proposed by Einfeldt et al. [27]. The inset shows the light microscope picture of a 1.5 $\mu$m thick AlGaN layer with an Al mole fraction in the solid of 0.06 on a sapphire-based GaN template ($A_{\mathrm{AlGaN}}$). The length of the white bar corresponds to a distance of 100 $\mu$m.

To find the optimum combination of Al mole fraction in the solid and cladding layer thickness the influence of those parameters on the heterostructure is discussed. Pseudomorphic AlGaN grown on GaN cracks above a critical layer thickness, which decreases with increasing Al mole fraction in the solid, as a consequence of the lattice mismatch between AlN and GaN [134]. The cracks (seen inset in Fig. 7.11) prevent the wave propagation in the cavity and provide parasitic current paths and therefore

make laser operation impossible.

Einfeldt el al. [27] investigated the tensile strain relaxation by crack formation in epitaxially grown $Al_xGa_{(1-x)}N$ on sapphire-based GaN templates. Fig. 7.11 shows the calculated critical AlGaN layer thickness on GaN . By comparing the relief of strain energy with the increase in the surface energy a critical thickness for AlGaN layer cracking is estimated. Using this approach the critical thickness of $Al_{0.06}Ga_{0.94}N$ and $Al_{0.10}Ga_{0.90}N$ can be calculated to around 1.3 and 0.5 $\mu$m, respectively. According to Fig. 7.10 b) 0.75 $\mu$m $Al_{0.10}Ga_{0.90}N$ are necessary to achieve the optical confinement of an 1.2 $\mu$m $Al_{0.06}Ga_{0.94}N$ cladding layer. Since 0.75 $\mu$m $Al_{0.10}Ga_{0.90}N$ are cracked cladding layers with an Al mole fraction of 0.10 are not suitable. For this reason a thicker cladding layer with a lower Al mole fraction in the solid is more suitable.

### 7.2.2 Adjustment of the waveguide layer

Due to the AlGaN layer cracking at high Al mole fractions the improvement of the mode guiding by adjusting the cladding layer is limited. Therefore, the influence of the waveguide layer composition and thickness on the modal gain of LD structures emitting around 450 nm is analyzed.

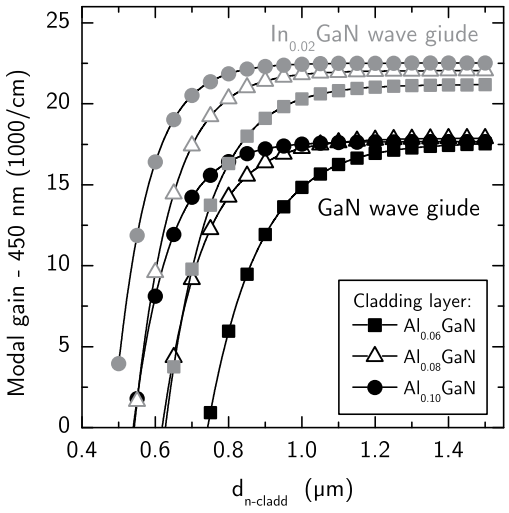


Figure 7.12: Simulation of the cladding layer Al mole fraction in the solid and thickness dependency of 450 nm LD structures with n-side $In_{0.02}Ga_{0.98}N$ (grey symbols) or GaN (black symbols), respectively. A material gain of 1000 $cm^{-1}$ was assumed.

In a first approach the modal confinement is increased by adjusting the refractive index of the waveguide layer. Therefore, 450 nm LD structures with $In_{0.02}Ga_{0.98}N$ or GaN n-side waveguides are simulated. As can be seen in Fig. 7.12 the higher refractive index of the $In_{0.02}Ga_{0.98}N$ waveguides results in an increase of the modal gain.

A second approach to increase the modal gain of LDs emitting around 450 nm is the increased the waveguide thicknesses. On the one hand the vertical extension of the mode increases as the thickness increases. Consequentially, the intensity of the electric field in the quantum wells and therefore $\Gamma$ decreases as can be seen in Fig. 7.13 a). On the other hand the intensity of the electric field in the cladding layer drops as the distance of the cladding to the gain region increases. As a consequence of the decreased electric field strength in the cladding layer the mode leakage and the absorption losses decrease and the modal gain increases.

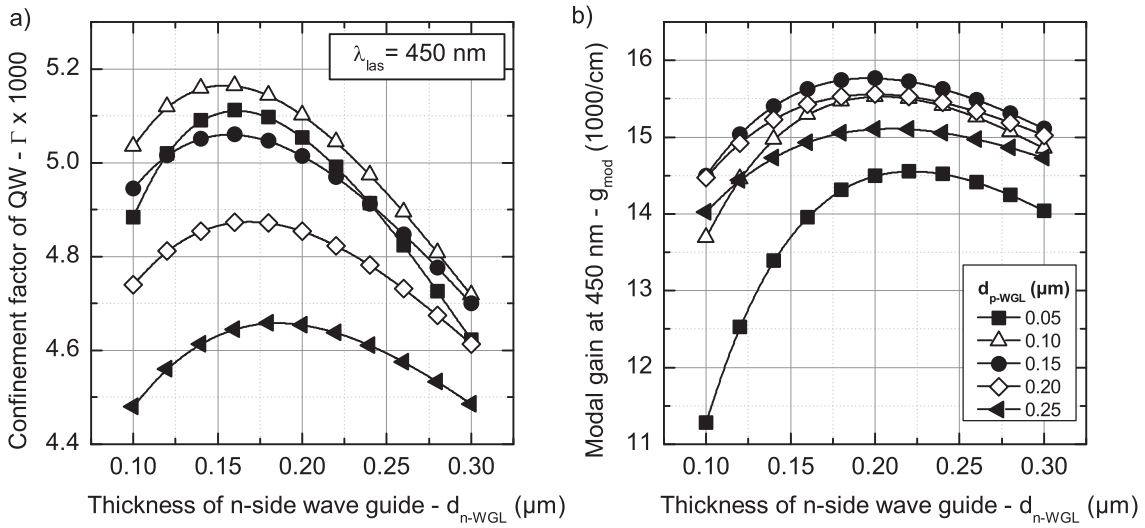


Figure 7.13: a) n- and p-side waveguide thickness dependency of the confinement factor of the first QW of a LD structure emitting around 450 nm. b) Corresponding modal gain.

Fig. 7.13 b) shows that an optimum waveguide thickness exists due to the two effects that are working in opposite direction as described above. In the case of a heterostructure layout as described in Tab. 7.1 the modal gain is highest for a n- and p-side waveguide thickness of 200 and 150 nm, respectively. The ratio of the thicknesses also depends on the doping level and therefore the absorption in the p-type doped layer. Since the absorption coefficients are quite uncertain for p-type doped AlGaN the accurate thickness ratio needs to be experimentally determined by the preparation and characterization of LD structures.

**Experimental verification of the simulated structure variations**

Two optical pumpable laser structures (type (c) in Fig. 2.1) with 100 nm ($J_{\mathrm{I}}^{450\,\mathrm{nm}}$) or 200 nm ($J_{\mathrm{II}}^{450\,\mathrm{nm}}$) thick n-side waveguides were grown in the Aix2400G3-HT on sapphire based GaN templates. Additionally, to the mentioned samples with GaN waveguides a sample $J_{\mathrm{III}}^{450\,\mathrm{nm}}$ with an $In_{0.02}Ga_{0.98}N$ n-side waveguide was prepared. The active regions consist of 3× $In_{0.15}Ga_{0.85}N/In_{0.05}Ga_{0.95}N$ MQW with 1.75 and 7.5 nm thick quantum wells and barriers, respectively. For barrier growth $T_{\mathrm{proc}}$ was increased by 75 K with respect to the well in order to improve the crystal perfection of the material. The MQW growth scheme is identical to sample set $B^{\mathrm{dQW}}$ shown in Fig. 4.1. The heterostructure properties of samples $J_{\mathrm{I}}^{450\,\mathrm{nm}}$, $J_{\mathrm{II}}^{450\,\mathrm{nm}}$ and $J_{\mathrm{III}}^{450\,\mathrm{nm}}$ are noted in Tab. 7.2.

The samples were characterized by light microscopy, AFM, PL, HR-XRD and optical pumping experiments. The measurement results are summarized in Tab. 7.3. The PL was measured using the 378 nm diode laser with an excitation power density of around 20 mW/cm$^2$. The noted AFM $r_{\mathrm{rms}}$ values correspond to a 5×5 $\mu$m$^2$ area of the wafer surface. The roughness of the n-side waveguide was revealed by stopping the growth after the n-side waveguide deposition. One wafer was taken out of the reactor for AFM measurements whereas a second wafer was finished to the optical pumpable structures. For device characterization by optical pumping a 266 nm fre-

| | | $J_{\mathrm{I}}^{450\,\mathrm{nm}}$ | | | $J_{\mathrm{II}}^{450\,\mathrm{nm}}$ | | | $J_{\mathrm{III}}^{450\,\mathrm{nm}}$ | | |
|---|---|---|---|---|---|---|---|---|---|---|
| | Mat. | x | y | d (nm) | x | y | d (nm) | x | y | d (nm) |
| Cap | AlGaN | 0.2 | | 20 | 0.2 | | 20 | 0.2 | | 20 |
| WGL | GaN | | | 100 | | | 300 | | | 300 |
| AR | | 3× $In_{0.15}Ga_{0.85}N$ / $In_{0.05}Ga_{0.95}N$ MQW (1.75 / 7.5 nm) | | | | | | | | |
| WGL | InGaN | | | 100 | | | 200 | | 0.02 | 200 |
| CL | AlGaN | 0.12 | | 200×2.5 | 0.12 | | 240×2.5 | 0.12 | | 240×2.5 |
| | GaN | | | 200×2.5 | | | 240×2.5 | | | 240×2.5 |
| | | 3 $\mu$m GaN:Si buffer | | | | | | | | |
| | | 430 $\mu$m sapphire substrate | | | | | | | | |

Table 7.2: Heterostructure layout for samples $J_{\mathrm{I}}^{450\,\mathrm{nm}}$, $J_{\mathrm{II}}^{450\,\mathrm{nm}}$ and $J_{\mathrm{III}}^{450\,\mathrm{nm}}$.

quency quadrupled Nd:YAG was used for the excitation of a 40 × 1000 $\mu$m area on the wafer.

| | | $J_{\mathrm{I}}^{450\,\mathrm{nm}}$ | | $J_{\mathrm{II}}^{450\,\mathrm{nm}}$ | | $J_{\mathrm{III}}^{450\,\mathrm{nm}}$ | |
|---|---|---|---|---|---|---|---|
| | | value | | value | | value | |
| 10 K-$\lambda_{\mathrm{PL}}$ | (nm) | 464 | ±2 | 486 | ±2 | 490 | ±2 |
| 10 K-FWHM | (nm) | 25 | ±2 | 30 | ±2 | 30 | ±2 |
| $\lambda_{\mathrm{las}}$ | (nm) | 431 | ±5 | 457 | ±5 | 465 | ±5 |
| $i_{\mathrm{th}}$ | (MW/cm$^2$) | 7.6 | ±1 | 2.0 | 0.5 | 1.75 | ±0.5 |
| $r_{\mathrm{rms}}$ n-WGL | (nm) | 0.4 | | 0.4 | | 1.1 | |

Table 7.3: Characterization results for samples $J_{\mathrm{I}}^{450\,\mathrm{nm}}$, $J_{\mathrm{II}}^{450\,\mathrm{nm}}$ and $J_{\mathrm{III}}^{450\,\mathrm{nm}}$.

The AlGaN /GaN:Si SPSL was increased to 240 periods in samples $J_{\mathrm{II}}^{450\,\mathrm{nm}}$ and $J_{\mathrm{III}}^{450\,\mathrm{nm}}$ in contrast to 100 in sample $J_{\mathrm{I}}^{450\,\mathrm{nm}}$. The HR-XRD and light microscopy analysis revealed pseudomorphic AlGaN layer deposition without surface cracking for all samples (not shown here). To reveal the crystal perfection of the active region PL was measured on the samples. While the $\lambda_{\mathrm{PL}}$ varies between 465 ($J_{\mathrm{I}}^{450\,\mathrm{nm}}$), 486 ($J_{\mathrm{II}}^{450\,\mathrm{nm}}$) or 490 nm ($J_{\mathrm{III}}^{450\,\mathrm{nm}}$) the FWHM is around 30 nm for all samples. The variation of the $\lambda_{\mathrm{PL}}$ despite nominally identical deposition conditions is due to limited reproducibility over the long time span between the production of the individual samples. According to Sec. 6.2.3 the PL FWHM is a good figure of merit for the crystal perfection of the active region. Since the FWHM is similar for the samples with similar $\lambda_{\mathrm{PL}}$ but different n-waveguide In mole fraction in the solid the crystal perfection of the active region does not seem to be sensitive on the composition of the n-side waveguide.

Despite the similar behavior of the samples at low excitation during PL measurements the optical pumping experiments revealed major differences. First the differences between the samples with GaN waveguides $J_{\mathrm{I}}^{450\,\mathrm{nm}}$ (100 nm) and $J_{\mathrm{II}}^{450\,\mathrm{nm}}$ (200 nm) are discussed. Different to the spectrum in Fig. 7.9 the spectra below the threshold of sample $J_{\mathrm{II}}^{450\,\mathrm{nm}}$ exhibit no intensity fringes (not shown here). $i_{\mathrm{th}}$ is with

2 MW/cm$^2$ significantly lower in sample $J_{\mathrm{II}}^{450\,\mathrm{nm}}$ in comparison to 7 MW/cm$^2$ in sample $J_{\mathrm{I}}^{450\,\mathrm{nm}}$. The lower $i_{\mathrm{th}}$ at higher $\lambda_{\mathrm{las}}$ is in good agreement with the improved optical confinement due to the increase of the n-side waveguide layer thicknesses and the number of AlGaN/GaN:Si SPSL periods in structure $J_{\mathrm{II}}^{450\,\mathrm{nm}}$.

Next the influence of the waveguide composition is discussed. In contrast to the simulation the $In_{0.02}Ga_{0.98}N$ n-side waveguide in sample $J_{\mathrm{III}}^{450\,\mathrm{nm}}$ exhibits no substantial decrease of the optical threshold power density. $i_{\mathrm{th}}$ was determined to around 2 MW/cm$^2$; $\lambda_{\mathrm{las}}$ is slightly red-shifted to around 470 nm with respect to $J_{\mathrm{II}}^{450\,\mathrm{nm}}$. It is assumed that the low crystal perfection of the active region associated with the high PL FWHM limits the material gain in the investigated samples. For the 450 nm heterostructures described as follows GaN waveguides are used since the InGaN waveguide layer growth requires elaborate growth optimization.

## 7.3 Adjustment of the active region

It was shown in the previous section that an improvement of the optical confinement enables lower optical threshold power densities at longer emission wavelengths. Secondly, it turned out that the material gain of the active material prevents the laser operation at low power densities. In order to reduce $i_{\mathrm{th}}$ further the influence of the active region heterostructure layout on the modal as well as material gain is investigated.

### 7.3.1 Variation of the QW number

Since the threshold power density of a LD is proportional to the number of QWs, the reduction of the QW number helps to decrease the threshold power densities.

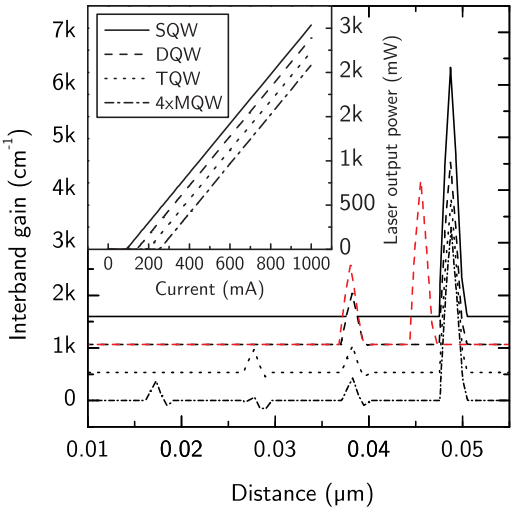


Figure 7.14: Simulated band to band recombination efficiency of 450 nm laser structures with different numbers of QWs. The inset displays P-I characteristics of blue LDs emitting around 450 nm with adjusted wave guiding layer. The line color corresponds to different laser structures with of 7.5 (black line) and 4.5 nm (red line) wide barrier layers.

Fig. 7.14 shows the influence of the QW-number and the band to band transition efficiency and the L-I characteristics (inset). The heterostructure design corresponds to $J_{\mathrm{II}}^{450\,\mathrm{nm}}$ in Tab. 7.1. According to the simulation the decrease of the QW number affects the device characteristics in several ways: First, by decreasing the QW number

the volume of the material that needs to be pumped and thus $i_{\mathrm{th}}$ is reduced. Secondly, the effective index of the mode decreases as the average In mole fraction in the active region is reduced. As a consequence the confinement factor and hence the modal gain is reduced. Thirdly, as can be seen in Fig. 7.14 the band to band gain varies strongly from QW to QW. The finding is due to a low mobility of the carriers (diffusion lengths are between 0.1 and 0.3 $\mu$m for electrons [135] and holes [136, 137] depending on the doping level and dislocation density of the GaN) and the resulting inefficient hole injection in the n-side QW. This QW contributes only little to the gain of the structure but affects the crystal perfection of the active region as shown in the following section.

**Experimental verification of the simulated structure variations**

| AR | | $J_{\mathrm{II}}^{450\,\mathrm{nm}}$ 3×$In_{0.15}GaN$/ $In_{0.05}GaN$ 1.75/7.5 nm | | $K_{\mathrm{II}}^{450\,\mathrm{nm}}$ 2×$In_{0.15}GaN$/ $In_{0.05}GaN$ 1.75/4.5 nm | | $K_{\mathrm{III}}^{450\,\mathrm{nm}}$($K'^{450\,\mathrm{nm}}_{\mathrm{III}}$) 2×$In_{0.15}GaN$/ $In_{0.005}GaN$/ 1.75/4.5 nm | |
|---|---|---|---|---|---|---|---|
| n-side WGL | | 200 nm GaN | | 200 nm GaN | | 200 nm InGaN | |
| 10 K-$\lambda_{\mathrm{PL}}$ | (nm) | 490 | ±2 | 490 | ±2 | 490 (490) | ±2 |
| 10 K-FWHM | (nm) | 30 | ±2 | 22 | ±2 | 22 (22) | ±2 |
| RT/10 K-PL | int. | 0.1 | ±0.02 | 0.03 | ±0.02 | 0.1 (0.1) | ±0.02 |
| $\lambda_{\mathrm{las}}$ | (nm) | 465 | ±5 | 464 | ±5 | 465 (455) | ±5 |
| $i_{\mathrm{th}}$ | ($\mathrm{MW/cm^2}$) | 2 | ±0.1 | 0.3 | | - (1.5) | ±0.5 |
| $r_{\mathrm{rms}}$ n-WGL | (nm) | 0.4 | | 0.4 | | 1.1 (0.6) | |

Table 7.4: Characterization results for sample $J_{\mathrm{II}}^{450\,\mathrm{nm}}$, $K_{\mathrm{II}}^{450\,\mathrm{nm}}$, $K_{\mathrm{III}}^{450\,\mathrm{nm}}$ and $K'^{450\,\mathrm{nm}}_{\mathrm{III}}$. For sample $K'^{450\,\mathrm{nm}}_{\mathrm{III}}$ the In mole fraction in the wave guide was reduced to 0.01 with respect to 0.02 in sample $K_{\mathrm{III}}^{450\,\mathrm{nm}}$.

Samples $J_{\mathrm{II}}^{450\,\mathrm{nm}}$ and $J_{\mathrm{III}}^{450\,\mathrm{nm}}$ with 200 nm thick GaN or $In_{0.02}Ga_{0.98}N$ n-side waveguides were reproduced with a DQW instead of a TQW. Furthermore, the barrier thickness was decreased from 7.5 to 4.5 nm in order to increases the hole injection in the first QW. The new samples are denoted as $K_{\mathrm{II}}^{450\,\mathrm{nm}}$ (GaN WGL) and $K_{\mathrm{III}}^{450\,\mathrm{nm}}$ ($In_{0.02}Ga_{0.98}N$ WGL). The heterostructure properties as well as analysis results are summarized in Tab. 7.4.

Fig. 7.15 shows the 10 K-PL spectra of samples $J_{\mathrm{II}}^{450\,\mathrm{nm}}$ (TQW) and $K_{\mathrm{II}}^{450\,\mathrm{nm}}$ (DQW). Both samples exhibit luminescence at 490 nm. The 10 K-FWHM decreases from around 30 to 23 nm as the QW number decreases. Furthermore, the temperature dependence of the normalized PL intensity (see inset of Fig. 7.15) is stronger for the DQW sample than for the TQW. These findings are attributed to a higher crystal perfection of the active region (see Sec. 6.2.3) and less lateral band gap non-uniformities (also see Sec. 4.3.2) for the DQW than for the TQW.

The optical pumping experiments on sample $K_{\mathrm{II}}^{450\,\mathrm{nm}}$ revealed an optical threshold power density as low as 350 $\mathrm{kW/cm^2}$ at $\lambda_{\mathrm{las}} \simeq 464$ nm. On sample $K_{\mathrm{III}}^{450\,\mathrm{nm}}$ no laser

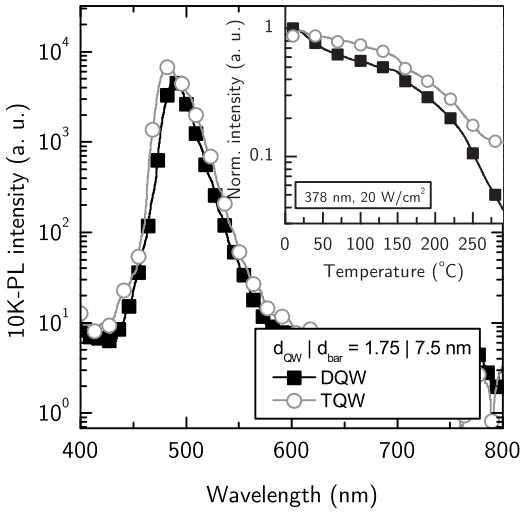


Figure 7.15: 10 K-PL spectra of samples $J_{\mathrm{II}}^{450\,\mathrm{nm}}$ (TQW) and $K_{\mathrm{II}}^{450\,\mathrm{nm}}$ (DQW). The inset shows the temperature dependency of the normalized PL intensity for both samples.

operation was achieved. A similar sample with reduced In mole fraction of 0.01 in the n-side waveguide ($K'^{450\,\mathrm{nm}}_{\mathrm{III}}$) showed lasing with a $i_{\mathrm{th}} \geq 1.5\,\mathrm{MW/cm^2}$ at a wavelength of 455 nm.

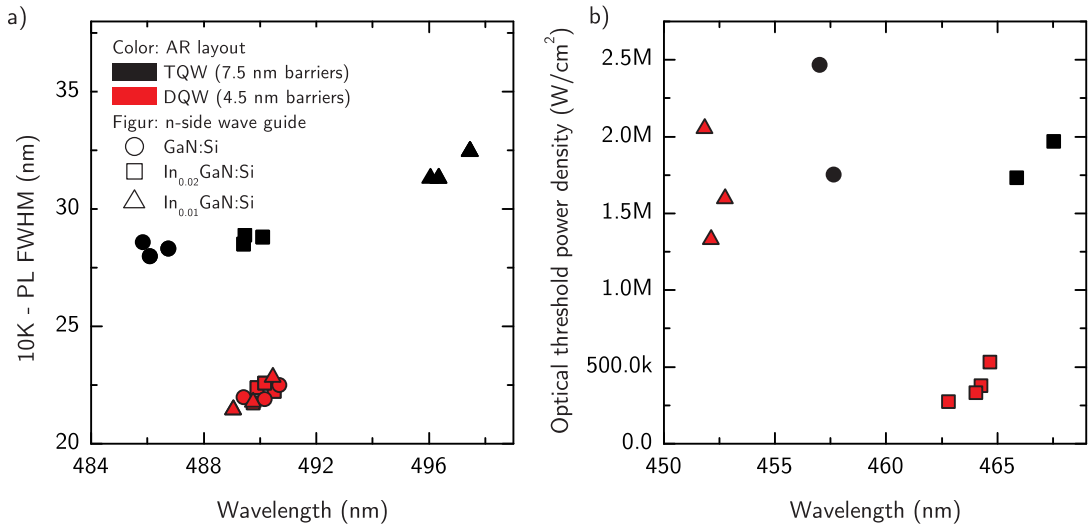


Figure 7.16: 10K-PL FWHM (a) and optical threshold power density (b) of samples $J_{\mathrm{II}}^{450\,\mathrm{nm}}$,$J_{\mathrm{III}}^{450\,\mathrm{nm}}$, $K_{\mathrm{II}}^{450\,\mathrm{nm}}$, $K_{\mathrm{III}}^{450\,\mathrm{nm}}$ and $K'^{450\,\mathrm{nm}}_{\mathrm{III}}$ . The 378 nm diode laser(20 W/cm$^2$) and the HeCd laser was used for excitation for the PL or optical pumping experiments, respectively.

The measurement results of the samples with the different number of QWs and different In mole fraction in the n-side waveguide are summarized in Fig. 7.16. By reducing the QW number and the barrier thickness the optical threshold power density was reduced to around 300 kW/cm$^2$. This result is attributed to an increased crystal perfection of the active region as well as to a reduced volume of gain material. The simulations suggest that the n-side QW in the TQW structure does not contribute remarkably to the gain. The optimization criteria developed in Sec. 6.2.3 proved correct for the samples with the GaN n-side waveguides only. Here, a narrow PL line width corresponds to a high crystal perfection of the active region and therefore a

low optical threshold power density.

It was shown that the introduction of an $In_{0.02}Ga_{0.98}N$ waveguide has no positive impact on the device characteristics. The samples with InGaN waveguides show no correlation between the PL-FWHM and the optical threshold power densities. It is assumed that the high roughness of the waveguide layer results in a strong carrier localization in the active regions in these structures. Nevertheless, the $r_{rms}$ roughness of the wave guiding layer correlates the optical threshold power densities. The optical threshold power densities increase as the morphology of the waveguide layer underneath the active region roughens. Despite the improved modal confinement the samples with the InGaN waveguides suffer from a deterioration of the AR. In summary, the optimization of the InGaN waveguides on the n-sides requires further effort in order to reduce the roughness associated with spiral growth as reported in Sec. 3.3.2. For this reason we concentrate on the approach with the GaN waveguides.

### 7.3.2 Adjustment of the well thickness

By reducing the number of QWs the laser threshold but also the optical confinement and output power of the laser decreases. To compensate for the gain material reduction the thickness of the QWs can be increased. This heterostructure parameter was found to have a huge influence on both the device properties as well as the material perfection of the active region. As shown in Sec. 4, samples with QW thicknesses below 1.5 and above 2.5 nm exhibited enhanced spatial band gap fluctuations due to thickness or In mole fraction variations. On the one hand the thin QWs benefit from a high oscillator strength due to a low spatial separation of the carriers the QWs. On the other hand, microscopic modeling of InGaN/ GaN LD devices [138] predicts an increase of $i_{th}$ as $d_{QW}$ decreases due to a higher spontaneous emission induced loss current. Furthermore the effective mode index and therefore the $\Gamma$ decreases as the overall In mole fraction in the active region decreases. Since the described effects work in opposite direction the optimum QW is determined by device simulations first. Since the LD emission wavelengths is very sensitive to QW width the In mole fraction in the QW is adjusted accordingly in order to realize emission around 450 nm.

Fig. 7.17 shows the simulated $x_{QW}$ and $d_{QW}$ dependency of the LD modal gain. Superimposed to the color plot the corresponding emission wavelengths are shown (thick black lines for 440 and 460 nm). The simulated heterostructure layout corresponds to the initial 450 nm LD layout in Tab. 7.1 but 200 nm GaN waveguides and 4.5 nm thin barrier according to the results above. The number of QWs was reduced to one in order to decrease the simulation time and increase the simulation stability. Since only one QW primarily contributes to the gain of the whole active region (see Fig. 7.14) this simplified approach allows the prediction of the LD characteristics.

First the influence of $d_{QW}$ on the emission wavelength at a constant $x_{QW}$ of 0.2 is discussed. At low QW thicknesses around 1 nm the simulated LD wavelength is 410 nm. Increasing $d_{QW}$ to 3 nm the wavelength is shifted to 450 nm due to a lower quantization energy of the carriers in the quantum well. Since the intrinsic fields are not completely screened by the carriers at the carrier density corresponding to

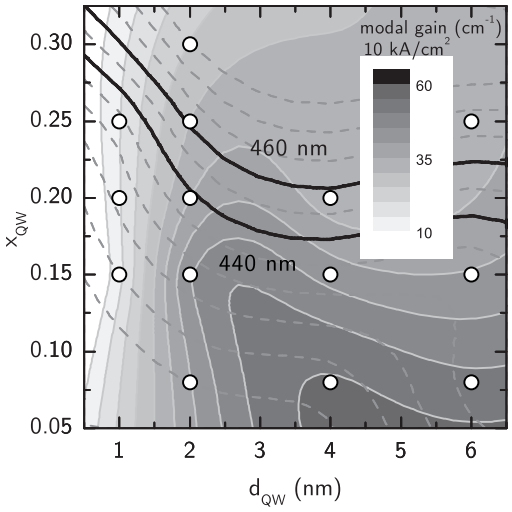


Figure 7.17: 450 nm LD device simulation: $d_{\mathrm{QW}}$ and $x_{\mathrm{QW}}$ dependency of the modal gain at 10 kA/cm$^2$. The corresponding LD wavelengths are represented by the thick black lines (of 440 and 460 nm). The contour lines are interpolations of the simulated $d_{\mathrm{QW}}$ and $x_{\mathrm{QW}}$ values represented by the open circles.

10 kA/cm$^2$, the emission wavelength is additionally red-shifted due to the QCSE. According to the simulations no further red-shift is expected as $d_{\mathrm{QW}}$ increases to 8 nm. For these thick QWs the sensitivity of $\lambda_{\mathrm{las}}$ to the quantization energy and the QCSE is very low.

In order to realize LD emission around 450 nm for all $d_{\mathrm{QW}}$ the $x_{\mathrm{QW}}$ had to be adjusted in the simulations. Due to the red-shift of the luminescence described above the In mole fraction in the quantum wells can be decreased from to 0.3 ($d_{\mathrm{QW}}$=1 nm) to 0.2 (3 nm and above). To reveal the optimum combination of $x_{\mathrm{QW}}$ and $d_{\mathrm{QW}}$ for a 450 nm LD the color coded modal gain between the thick black lines in Fig. 7.17 is analyzed.

For small $d_{\mathrm{QW}}$ and high $x_{\mathrm{QW}}$ the modal gain at 10 kA/cm$^2$ is around 10 cm$^{-1}$. $g_{\mathrm{mod}}$ increases to around 40 cm$^{-1}$ as $d_{\mathrm{QW}}$ increases to 3 nm ($x_{\mathrm{QW}}$=0.2). The increase is due to the increase of the confinement factor and the decrease of the spontaneous emission loss as $d_{\mathrm{QW}}$ increases. Furthermore, the piezoelectric field strength decreases as $x_{\mathrm{QW}}$ decreases. Increasing $d_{\mathrm{QW}}$ further $g_{\mathrm{mod}}$ can not be increased any more but slightly decreases. In this $d_{\mathrm{QW}}$ range the reduction of the spontaneous emission loss and the increase of $\Gamma$ are more than compensated by the lower oscillator strength.

**Experimental verification of the simulated structure variations**

In order to reveal the optimum combination of $x_{\mathrm{QW}}$ and $d_{\mathrm{QW}}$ regarding the best crystal perfection of the active region and the lowest $i_{\mathrm{th}}$ a set of optically pump-able structures ($L_{\mathrm{oLD}}^{450\,\mathrm{nm}}$) was prepared. By varying the well growth time between 45 and 105 s and the well growth temperature between 750 and 800 °C $d_{\mathrm{QW}}$ was varied between 1.5 and 3.5 nm and $x_{\mathrm{QW}}$ between 0.1 and 0.2.

Fig 7.18 a) shows the PL wavelength and FWHM of set $L_{\mathrm{oLD}}^{450\,\mathrm{nm}}$. The emission wavelength of the samples increases as $d_{\mathrm{QW}}$ decreases or the QW growth temperature decreases. The latter results in an increase of the In mole fraction in the QWs from around 0.1 at 800 °C to 0.2 at 750 °C. The observed wavelength-shift is due to the variation of the quantization energy in the different QWs as well as the different

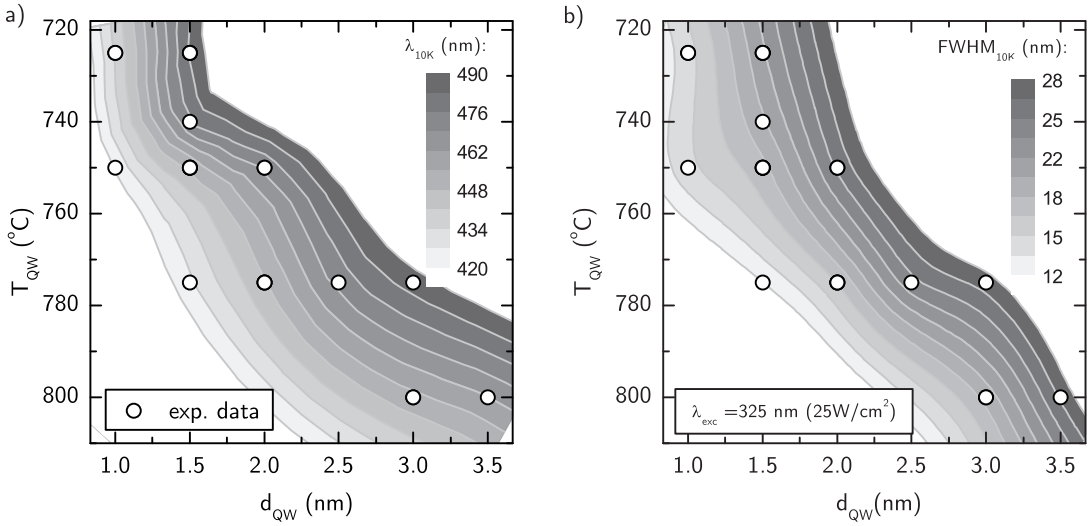


Figure 7.18: PL wavelength (a) and FWHM (b) at 10 K for sample set $L_{\mathrm{oLD}}^{450\,\mathrm{nm}}$ with varying $d_{\mathrm{QW}}$ and QW growth temperature. The contour lines are interpolations of the experimental results represented by the open circles. A HeCd laser (325 nm) with 25 W/cm$^2$ was used for excitation.

manifestation of the QCSE.

The line width in Fig 7.18 b) shows a distinct sensitivity to the QW parameters. According to Sec. 6 the crystal perfection of the different active regions can be evaluated by analyzing the PL-FWHM. In this case the correlation is not straight forward. As has been shown by Schubert et al. and Hangleiter et al. [139, 140] in a system with (statistical) band gap fluctuations the line width naturally increases as the well width increases. Since it is hard to qualify the crystal perfection in set $L_{\mathrm{oLD}}^{450\,\mathrm{nm}}$ the device properties are determined by optical pumping experiments.

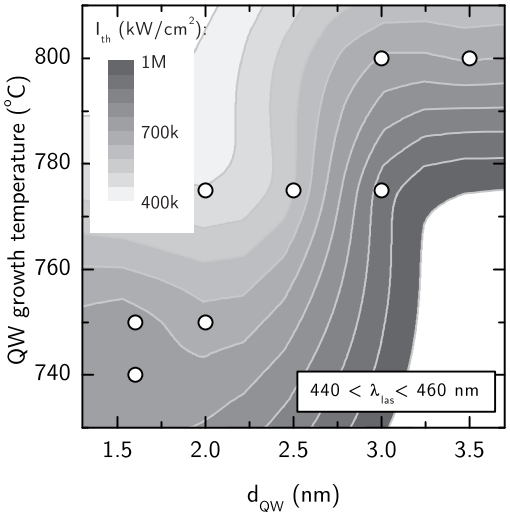


Figure 7.19: Color plot of the experimentally determined $d_{\mathrm{QW}}$ and $x_{\mathrm{QW}}$ dependency of $i_{\mathrm{th}}$ of oLD structures of set $L_{\mathrm{oLD}}^{450\,\mathrm{nm}}$. The corresponding laser wavelengths above the threshold are between 440 and 460 nm for all samples. A 266 nm frequency quadrupled Nd:YAG laser is used for excitation. The contour lines are interpolations of the experimental results represented by the open circles

Fig. 7.19 shows the experimentally determined $d_{\mathrm{QW}}$ and $x_{\mathrm{QW}}$ dependency of the $i_{\mathrm{th}}$ for the samples of set $L_{\mathrm{oLD}}^{450\,\mathrm{nm}}$. All structures show distinct lasing and emission between 440 and 460 nm above the threshold. The lowest $i_{\mathrm{th}}$ of around 300 kW/cm$^2$ was achieved for the sample with the 2 nm thick $d_{\mathrm{QW}}$ grown at 775 °C. Despite the

predictions of the simulations discussed above the optical threshold power density increases as the well thickness increases to 3 nm. The sample with the 3 nm thick QW (800 °C) exhibits an $i_{\mathrm{th}}$ around 700 kW/cm$^2$.

Since the material perfection in the different samples can not be resolved, one can only speculate on the disagreement between the simulation and the experiment. In Sec. 4.3 the lateral band gap non-uniformities increase as $d_{\mathrm{QW}}$ increases. On the other hand the spatial homogeneity increases as $x_{\mathrm{QW}}$ increases (see Sec. 5.3.1) Most probably the first effect is more dominant and therefore $i_{\mathrm{th}}$ is increased for the wide QW. In order to improve the material quality for the wide QWs with the alleged highest modal gain the influence of the growth conditions on the material perfection is investigated further in the next section.

**Adjustment of the active region growth conditions for wide QWs**

The QW growth conditions are already optimized to provide a high In incorporation efficiency and low spatial band gap fluctuations (according to the optimization scheme described in Sec. 6). Since further QW growth condition variations are limited by the material requirements the growth of the quantum barriers is analyzed. Their crystal perfection has a huge influence on the device properties for two reasons: First, the crystal perfection of the QW depends on the morphology of the barrier layer on which it is grown. Secondly, the barrier material has a high overlap with the part of the optical mode that has the highest intensity. An improvement of the crystal perfection will therefore improve the perfection of the QWs and reduce sub-band gap absorption in the active region.

The samples discussed so far in this section feature the barrier growth scheme according to Fig. 4.1. After the QW deposition 0.5 to 1 nm thick GaN cap layer is grown at QW growth temperature. Since the small cap thickness is below the In segregation length (see. Sec. 4.2.2) this nominally GaN layer contains In. After the QW cap deposition the growth is stopped in order to raise the growth temperature by 75 K and the barrier layer is deposited using a reduced In mole fraction in the vapor. The ratio of the In mole fraction in the vapor is 0.2 for barrier / well growth.

To investigate the influence of the barrier growth conditions on the AR crystal perfection DQW samples with 3 nm wide wells and but different barrier growth schemes are prepared. The first sample in the set ($M_{\mathrm{oLD}}^{450\,\mathrm{nm}}$) follows a barrier growth scheme as described above. For the second sample the barrier growth temperature was not increased with respect to the well growth temperature. Also, the complete active region is grown without a growth interruption and it does not contain a QW capping layer.

Fig. 7.20 shows the LT-PL spectra and the temperature dependent PL intensity for set $M_{\mathrm{oLD}}^{450\,\mathrm{nm}}$. The samples with the LT barriers exhibits a 30 nm blue-shifted emission with respect to the sample with the HT barriers. The line width drops from 28 to 16.5 nm as the barrier growth temperature decreases. As can be seen in the inset in Fig. 7.20 the sample with the HT barriers exhibits a higher RT/10 K-PL intensity ratio which is attributed to a stronger localization of the carriers in spatial band-gap

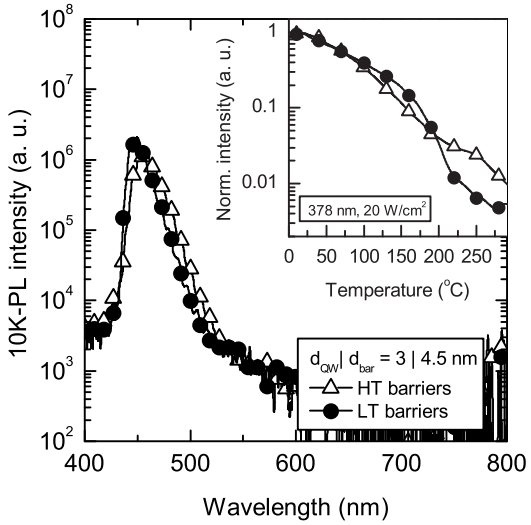


Figure 7.20: 10 K-PL spectra of sample set $M_{\mathrm{oLD}}^{450\,\mathrm{nm}}$ with HT and LT barriers. The inset shows the temperature dependency of the normalized PL intensity for both samples.

non-uniformities. Therefore, from the presented data the LT barrier growth scheme is assumed to improve the crystal perfection of the active region.

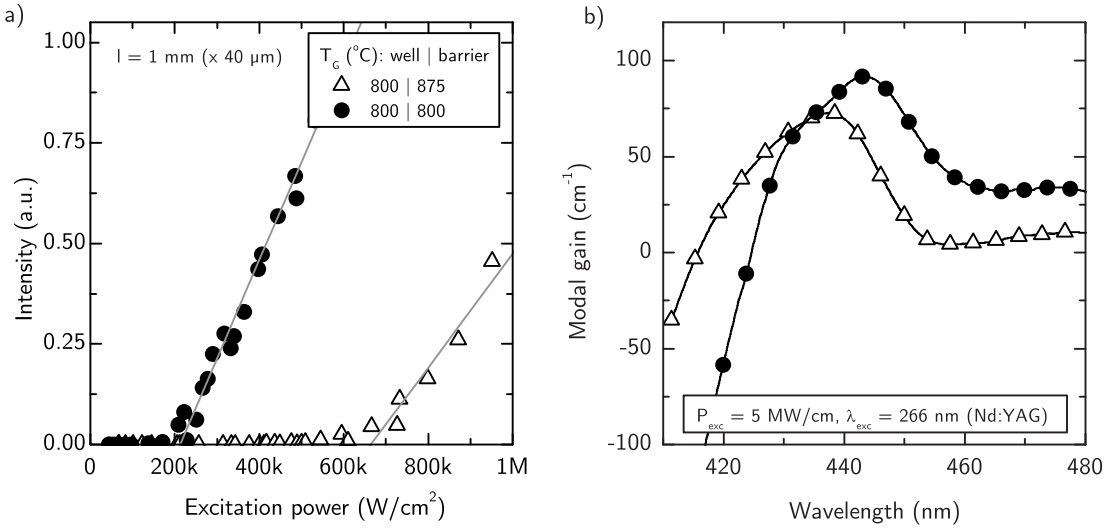


Figure 7.21: a) L-I characteristics of sample set $M_{\mathrm{oLD}}^{450\,\mathrm{nm}}$ with different QW and barrier growth temperatures. b) Spectra of the corresponding modal gain. The quadrupled Nd:YAG laser was used for excitation with an excitation power density of around 5 MW/cm$^2$.

Fig. 7.21 shows L-I characteristics and the modal gain spectra for the optically pump-able structures of set $M_{\mathrm{oLD}}^{450\,\mathrm{nm}}$. By reducing the barrier growth temperature the optical threshold power density is reduced from 700 to 200 kW/cm$^2$. The gain spectra exhibits a peak gain of around 90 cm$^{-1}$ at 443 nm in comparison to 70 cm$^{-1}$ at 438 nm for the HT barrier growth scheme. Interestingly, the shift between the gain maximum and the LT-PL peak is higher for the sample with the HT barriers. The finding can be explained by the proposed higher band gap non-uniformities in the sample with the HT barriers. At low excitation conditions the LT-PL luminescence is dominated by recombination from the band-gap minima. Increasing the excitation density the band gap minima fill up and the recombination of energetically higher

states dominates the spectra.

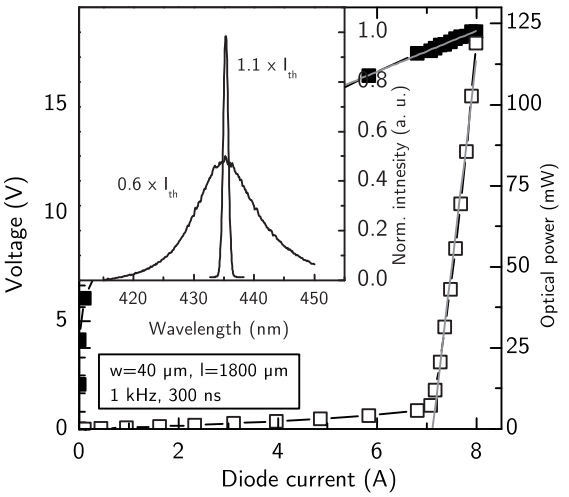


Figure 7.22: P-U-I characteristic of a BA-LD with a 40 $\mu$m wide contact stripe fabricated from sample $M_{\mathrm{LD}}^{450\,\mathrm{nm}}$. The repetition rate and pulse length was 1 kHz and 300 ns, respectively. The optical output power was determined for a single uncoated facet.

In order to analyze lasing through current-injection the sample with the LT-barrier growth scheme was reproduced as current injection LD on a GaN substrate. The sample is denoted as $M_{\mathrm{LD}}^{450\,\mathrm{nm}}$ and contains the AR of set $M_{\mathrm{oLD}}^{450\,\mathrm{nm}}$ with the LT barrier growth scheme and optimized waveguiding as described in Sec. 7.2.2. Fig. 7.22 shows the P-U-I characteristics as well as the spectra below and above $i_{\mathrm{th}}$. Lasing is achieved beyond a diode current of around 7 A. The corresponding current density is $10\,\mathrm{kA/cm^2}$.

## 7.4 Summary

Starting with a heterostructure layout for a 405 nm LD it was investigated how the heterostructure design needs to be modified in order to realize lasing at longer wavelengths. In a first step the heterostructure growth was transferred from sapphire substrate to GaN substrate. The investigations showed that the advantages of a lower threading dislocation density, a better cleaveability and higher thermal conductivity are accompanied by an inferior spatial homogeneity of the In incorporation on a large scale. Due to the lack of different thermal expansion coefficients in the substrate epi-layer system the wafer is concave during active region deposition. The resulting different thermal coupling of the wafer with the heating source is reduced by the usage of concavely pre-bowed GaN substrates or substrates with a higher thickness.

The next step toward a 450 nm laser structure was the adjustment of waveguiding. Due to the lower refractive index differences at longer wavelengths the optical confinement of the mode is increasingly reduced as the wavelength is increased. Approaches to increase the optical confinement by increasing the Al mole fraction in the cladding layer or the In mole fraction in the waveguides proved not practicable due to layer cracking and surface roughening. In order to reduce the mode leakage into the substrate the thickness of the wave guiding layer was increased. This way

the intensity of the mode in the cladding layer and thus the mode leaking into the substrate is reduced.

The last section of this chapter dealt with the adjustment of the active region. By comparing device simulation with growth variations the optimum quantum well width regarding modal gain and material perfection of the active region was determined to 3 nm for emission around 450 nm in comparison to 3.5 nm (405 nm). Furthermore, the QW number was reduced from 3 (405 nm) to 2 (450 nm) in order to improve the material perfection and the homogeneity of the hole injection into the wells. It turned out, that the material perfection of the active region can be further improved by adjustments of the barrier growth scheme. By decreasing the barrier width and barrier growth temperature both the luminescence line width and the optical laser threshold power density are considerably reduced. Lasing through current-injection was proved for a BA-LD laser structure emitting a 440 nm with an $i_{\mathrm{th}}$ of around $10\,\mathrm{kA/cm^2}$.

# 8

# Summary and Outlook

The presented work describes the MOVPE growth and investigation of InGaN quantum structures for laser heterostructures emitting in the violet/ blue wavelength region. The work focuses on two aspects of the device development: First, the understanding of the growth processes and the control of the material properties of the active region. Second, the establishment of a device development scheme involving the growth and simulation of different heterostructures and their characterization. By correlation of the different experimental and theoretical results optimization criteria for the different aspects of the device development, e.g. the design and the growth of the active region and the design of the waveguiding structure, were developed.

On the example of the InGaN active region the methodology can be easily explained. There is any number of designs and possibilities to grow a MQW emitting in a distinct wavelength. Not uncommonly, the variation of a single parameter affects different structure properties in different ways. Furthermore, the characterization of the complex structures gives not necessarily an unique result. For this reason it is important to exactly understand the growth mechanisms and the influence of the growth conditions on the material and heterostructure properties. Due to the vast optimization possibilities a simple and straight forward criterion, that allows the prediction of the improvement or deterioration of the device characteristics is mandatory for the device development.

It turned out that lateral uniformity of the material properties in the active region, such as the quantum well thickness and in mole fraction in the solid have a strong impact on the device efficiency. It was shown that the non-uniformity is mainly due to the transition from layer by layer growth to 3D growth during InGaN deposition. By analyzing the line width of the low excitation luminescence as a figure of merit the lateral uniformity of the InGaN quantum wells was improved. By adjusting the thicknesses of the InGaN well and barrier layers, optimizing the growth conditions and changing to substrates with lower defect densities the lateral variation of the well thickness and the in mole fraction in the solids was reduced. The device data show a significant reduction of the optical threshold power densities as the uniformity of the InGaN layer in the active region increases. Reproducing the active region in current injection device structures and processing them to BA-LD threshold current densities of around $4\,\mathrm{kA/cm^2}$ for 400 nm LDs and $10\,\mathrm{kA/cm^2}$ for 440 nm LDs were achieved.

Using the described optimization methods the perfection of the active region, the optical confinement of the mode and the electrical properties of the structure

can be further improved in order to decrease the threshold current densities. As mentioned in the introduction the nitride based LDs are only commercially available for a limited number of wavelengths or specifications in general. For this reason the presented work provides the basis technology for the realization of special applications in the wavelength range between 400 nm and 440 nm. in this range the substitution of conventional emitters for spectroscopic applications is of big interest. Further projects that benefit from the work are the realization of a blue femtosecond laser and a LD emitting at 435.9 nm for laser cooling of mercury atoms.

Future work has to address the optimization of heterostructure design and p-type doping in order to further increase the output power and lower the threshold current density. Having optimized the basic laser structure using stripe lasers also more complex device designs like tapered laser diodes or amplifiers can be developed.

# Bibliography


[1] Yamashita, H., Fukui, K., Misawa, S., and Yoshida, S. *Journal of Applied Physics* 50(2), 896–898 (1979).

[2] Wu, J., Walukiewicz, W., Yu, K., Ager III, J., Haller, E., Lu, H., Schaff, W., Saito, Y., and Nanishi, Y. *Applied Physics Letters* 80, 3967 (2002).

[3] Davydov, V., Klochikhin, A., Emtsev, V., Kurdyukov, D., Ivanov, S., Vekshin, V., Bechstedt, F., Furthmüller, J., Aderhold, J., Graul, J., et al. *physica status solidi (b)* 234(3), 787–795 (2002).

[4] Goto, O., Tomiya, S., Hoshina, Y., Tanaka, T., Ohta, M., Ohizumi, Y., Yabuki, Y., Funato, K., and Ikeda, M. volume 6485, 64850Z. SPIE, (2007).

[5] Risk, W., Gosnell, T., Nurmikko, A., and MyiLibrary. *Compact blue-green lasers*. Cambridge University Press New York, (2003).

[6] Hale, G. and Querry, M. *Applied Optics* 12(3), 555–563 (1973).

[7] Deka, C. and Steinkamp, J. A. *Appl. Opt.* 35(22), 4481–4489 (1996).

[8] Farr, N., Chave, A., Freitag, L., Preisig, J., White, S., Yoerger, D., Titterton, P., and Instn, W. *OCEANS, 2005. Proceedings of MTS/IEEE* 1, 928–934 (2005).

[9] Gilmore, D. A., Gurka, D., and Denton, M. B. *Appl. Spectrosc.* 49(4), 508–512 (1995).

[10] Broglia, M. *Appl. Opt.* 32(3), 334–338 (1993).

[11] Ruiz-Martinez, M., Berka, J., Belenkii, A., Foret, F., Miller, A., and Karger, B. *Analytical Chemistry* 65(20), 2851–2858 (1993).

[12] Damelincourt, J. J., Aubes, M., Fragnac, P., and Karabourniotis, D. *Journal of Applied Physics* 54(6), 3087–3097 (1983).

[13] Spielman, A., Perrone, J. B., Teklehaimanot, A., Balcha, F., Wardlaw, S. C., and Levine, R. A. *Am J Trop Med Hyg* 39(4), 337–342 (1988).

[14] Hnscheid, T. *Transactions of the Royal Society of Tropical Medicine and Hygiene* 102(6), 520 – 521 (2008).

[15] Rieder, C. L. and Khodjakov, A. *Science* 300(5616), 91–96 (2003).

[16] Zochowski, M., Wachowiak, M., Falk, C., Cohen, L., Lam, Y., Antic, S., and Zecevic, D. *Biol Bull* 198(1), 1–21 (2000).

[17] Winefordner, J. D. and Vickers, T. J. *Analytical Chemistry* 36(1), 161–165 (1964).

[18] Lichtman, J. and Conchello, J. *Nature Methods* 2(12), 910–919 (2005).

[19] Markov, I. *Crystal Growth for Beginners: Fundamentals of Nucleation, Crystal Growth and Epitaxy*. World Scientific, (2003).

[20] Stringfellow, G. and Corporation, E. *Organometallic vapor-phase epitaxy: theory and practice*, volume 19. Academic Press New York, (1989).

[21] Amano, H., Kito, M., Hiramatsu, K., and Akasaki, I. *Japanese Journal of Applied Physics* 28(Part 2, No. 12), L2112–L2114 (1989).

[22] Nakamura, S., Senoh, M., and Mukai, T. *Japanese Journal of Applied Physics* 32(Part 2, No. 1A/B), L8–L11 (1993).

[23] Geotz, W., Johnson, N., Walker, J., Bour, D., Amano, H., and Akasaki, I. *Applied Physics Letters* 67, 2666 (1995).

[24] Brandt, M. S., Ager, J. W., Götz, W., Johnson, N. M., Harris, J. S., Molnar, R. J., and Moustakas, T. D. *Phys. Rev. B* 49(20), 14758–14761 May (1994).

[25] Kuhn, B., Welsch, M., Kessler, M., and Scholz, F. *phys. stat. sol.(a)* 176, 789 (1999).

[26] Nakamura, S., Iwasa, N., Senoh, M., and Mukai, T. *Jpn. J. Appl. Phys.* 31(Part 1, No. 5A), 1258–1266 (1992).

[27] Einfeldt, S., Kirchner, V., Heinke, H., Dießelberg, M., Figge, S., Vogeler, K., and Hommel, D. *J. Appl. Phys.* 88, 7029–7036 dec (2000).

[28] Bernardini, F., Fiorentini, V., and Vanderbilt, D. *Phys. Rev. B* 56(16), R10024–R10027 Oct (1997).

[29] Im, J. S., Kollmer, H., Off, J., Sohmer, A., Scholz, F., and Hangleiter, A. *Phys. Rev. B* 57(16), R9435 apr (1998).

[30] Miller, D. A. B., Chemla, D. S., Damen, T. C., Gossard, A. C., Wiegmann, W., Wood, T. H., and Burrus, C. A. *Phys. Rev. Lett.* 53(22), 2173– nov (1984).

[31] Minsky, M. S., Watanabe, S., and Yamada, N. *J. Appl. Phys.* 91(8), 5176–5181 (2002).

[32] Strite, S. and Morkoc, H. *Journal of Vacuum Science & Technology B: Microelectronics and Nanometer Structures* 10(4), 1237–1266 (1992).

[33] Panish, M. B. and Temkin, H. *Growth and Properties of Phosphorus Containing III-V Heterostructures*, volume 26. Springer-Verlag, Berlin, Heidelberg, (1993).

[34] Keller, B., Keller, S., Kapolnek, D., Kato, M., Masui, H., Imagi, S., Mishra, U., and DenBaars, S. *Electronics Letters* 31(13), 1102–1103 (1995).

[35] Nakamura, S. *Jpn. J. Appl. Phys.* 30(Part 2, No. 10A), L1705–L1707 (1991).

[36] Wang, H.-M., Zhang, J.-P., Chen, C.-Q., Fareed, Q., Yang, J.-W., and Khan, M. A. *Applied Physics Letters* 81(4), 604–606 (2002).

[37] Mihopoulos, T. G., Gupta, V., and Jensen, K. F. *J. Cryst. Growth* 195(1-4), 733–739 dec (1998).

[38] Brunner, F., Protzmann, H., Heuken, M., Knauer, A., Weyers, M., and Kneissl, M. *Phys. Status Solidi (c)* 5(6), 1799–1801 (2008).

[39] Stoney, G. *Proceedings of the Royal Society of London. Series A, Containing Papers of a Mathematical and Physical Character* 82(553), 172–175 (1909).

[40] Kirchner, V., Fehrer, M., Figge, S., Heinke, H., Einfeldt, S., Hommel, D., Selke, H., and Ryder, P. *phys. stat. sol. (b)* 216(1), 659–662 (1999).

[41] Brunner, F., Knauer, A., Schenk, T., Weyers, M., and Zettler, J. *Journal of Crystal Growth* 310(10), 2432–2438 (2008).

[42] Reeber, R. and Wang, K. In *MATERIALS RESEARCH SOCIETY SYMPOSIUM PROCEEDINGS*, volume 622, 6–6. Warrendale, Pa.; Materials Research Society; 1999, (2001).

[43] Schenk, H. P. D., de Mierry, P., Laügt, M., Omnès, F., Leroux, M., Beaumont, B., and Gibart, P. *Applied Physics Letters* 75(17), 2587–2589 (1999).

[44] Piner, E. L., Behbehani, M. K., El-Masry, N. A., McIntosh, F. G., Roberts, J. C., Boutros, K. S., and Bedair, S. M. *Applied Physics Letters* 70(4), 461–463 (1997).

[45] Grzanka, S., Franssen, G., Targowski, G., Krowicki, K., Suski, T., Czernecki, R., Perlin, P., and Leszczyński, M. *Applied Physics Letters* 90(10), 103507 (2007).

[46] Schmidt, O., Wolst, O., Kneissl, M., Kiesel, P., Yang, Z. H., Teepe, M., and Johnson, N. M. *phys. stat. sol. (c)* 2(7), 2891–2894 (2005).

[47] Takagi, S. *Acta Crystallographica* 15(12), 1311–1312 Dec (1962).

[48] Zaumseil, P. *Rocking Curve & Reflectivity Curve Simulation & Fitting.* IHP, Im Technologiepark 25, D-15236 Frankfurt (Oder), Germany. dynamical theory of X-ray reflection using the matrix approach.

[49] van Look, J.-R., Einfeldt, S., Kruger, O., Hoffmann, V., Knauer, A., Weyers, M., Vogt, P., and Kneissl, M. *Photonics Technology Letters, IEEE* 22(6), 416 –418 mar. (2010).

[50] Wenzel, H. *Opt. Quantum. Electron.* 38(12), 953–961 sep (2006).

[51] STR Group Ltd., St.-Petersburg, R.

[52] Crosslight Software Inc., Burnaby, C.

[53] Fewster, P. F. and Andrew, N. L. *Thin Solid Films* 319(1-2), 1–8 apr (1998).

[54] Robinson, I. K. *Phys. Rev. B* 33(6), 3830–3836 Mar (1986).

[55] Howe, P., Ru, E. C. L., Clarke, E., Murray, R., and Jones, T. S. *Journal of Applied Physics* 98(11), 113511 (2005).

[56] People, R. and Bean, J. *Applied Physics Letters* 47, 322 (1985).

[57] Holec, D., Costa, P., Kappers, M., and Humphreys, C. *J. Cryst. Growth* 303(1), 314–317 may (2007).

[58] Cremades, A., Piqueras, J., Albrecht, M., Stutzmann, M., and Strunk, H. *Materials Science and Engineering: B* 80(1-3), 313 – 317 (2001).

[59] Pereira, S., O'Donnell, K., and daCostaAlves, E. *Advanced Functional Materials* 17(1), 37–42 (2007).

[60] Pereira, S., Correia, M. R., Monteiro, T., Pereira, E., Alves, E., Sequeira, A. D., and Franco, N. *Applied Physics Letters* 78(15), 2137–2139 (2001).

[61] Shikanai, A., Azuhata, T., Sota, T., Chichibu, S., Kuramata, A., Horino, K., and Nakamura, S. *Journal of Applied Physics* 81(1), 417–424 (1997).

[62] Carrier, P. and Wei, S.-H. *Journal of Applied Physics* 97(3), 033707 (2005).

[63] Wu, X. H., Elsass, C. R., Abare, A., Mack, M., Keller, S., Petroff, P. M., DenBaars, S. P., Speck, J. S., and Rosner, S. J. *Appl. Phys. Lett.* 72(6), 692 (1998).

[64] Kawaguchi, Y., Shimizu, M., Yamaguchi, M., Hiramatsu, K., Sawaki, N., Taki, W., Tsuda, H., Kuwano, N., Oki, K., Zheleva, T., and Davis, R. F. *J. Cryst. Growth* 189-190, 24–28 jun (1998).

[65] Kim, I.-H., Park, H.-S., Park, Y.-J., and Kim, T. *Applied Physics Letters* 73(12), 1634–1636 (1998).

[66] Burton, W. K., Cabrera, N., and Frank, F. C. *Philosophical Transactions of the Royal Society of London. Series A, Mathematical and Physical Sciences* 243(866), 299–358 Jun (1951).

[67] Srikant, V., Speck, J. S., and Clarke, D. R. *Journal of Applied Physics* 82(9), 4286–4295 (1997).

[68] Lester, S. D., Ponce, F. A., Craford, M. G., and Steigerwald, D. A. *Applied Physics Letters* 66(10), 1249–1251 (1995).

[69] Ning, X., Chien, F., Pirouz, P., Yang, J., and Khan, M. *Journal of Materials Research* 11(3), 580–592 (1996).

[70] Metzger, T., Höpler, R., Born, E., Ambacher, O., Stutzmann, M., Stömmer, R., Schuster, M., Göbel, H., Christiansen, S., Albrecht, M., and Strunk, H. P. *Philosophical Magazine A* 77(4), 1013–1025 (1998).

[71] Wellmann, P. J., Sakwe, S. A., Oehlschlager, F., Hoffmann, V., Zeimer, U., and Knauer, A. *J. Cryst. Growth* In Press, Corrected Proof, – (2007).

[72] Grandjean, N., Massies, J., and Raymond, F. *Japanese Journal of Applied Physics* 33(Part 2, No. 10A), L1427–L1430 (1994).

[73] Northrup, J. E., Romano, L. T., and Neugebauer, J. *Appl. Phys. Lett.* 74(16), 2319–2321 (1999).

[74] Nye, J. F. *Physical Properties of Crystals: Their Representation by Tensors and Matrices.* Oxford University Press, (1957).

[75] Romanov, A. E., Baker, T. J., Nakamura, S., Speck, J. S., and Group, E. U. *J. Appl. Phys.* 100(2), 023522 (2006).

[76] Piprek, J. and Nakamura, S. *IEE Proceedings - Optoelectronics* 149(4), 145–151 (2002).

[77] Keller, S., Chichibu, S. F., Minsky, M. S., Hu, E., Mishra, U. K., and DenBaars, S. P. *J. Cryst. Growth* 195(1-4), 258–264 dec (1998).

[78] van der Laak, N. K., Oliver, R. A., Kappers, M. J., and Humphreys, C. J. *J. Appl. Phys.* 102(1), 013513–8 jul (2007).

[79] Stephenson, G. B., Eastman, J. A., Thompson, C., Auciello, O., Thompson, L. J., Munkholm, A., Fini, P., DenBaars, S. P., and Speck, J. S. *Applied Physics Letters* 74(22), 3326–3328 (1999).

[80] Huang, X. R., Bai, J., Dudley, M., Dupuis, R. D., and Chowdhury, U. *Applied Physics Letters* 86(21), 211916 (2005).

[81] Kisielowski, C., Liliental-Weber, Z., and Nakamura, S. *Japanese Journal of Applied Physics* 36(Part 1, No. 11), 6932–6936 (1997).

[82] Duxbury, N., Bangert, U., Dawson, P., Thrush, E. J., der Stricht, W. V., Jacobs, K., and Moerman, I. *Appl. Phys. Lett.* 76(12), 1600–1602 (2000).

[83] Davidson, J. A., Dawson, P., Wang, T., Sugahara, T., Orton, J. W., and Sakai, S. *Semiconductor Science and Technology* 15(6), 497 (2000).

[84] Sasaki, A., Nishizuka, K., Wang, T., Sakai, S., Kaneta, A., Kawakami, Y., and Fujita, S. *Solid State Communications* 129(1), 31 – 35 (2004).

[85] Lahmann, S., Hitzel, F., Rossow, U., and Hangleiter, A. *phys. stat. sol. (c)* 0(7), 2202–2205 (2003).

[86] Fuhrmann, D., Netzel, C., Rossow, U., Hangleiter, A., Ade, G., and Hinze, P. *Applied Physics Letters* 88(7), 071105 (2006).

[87] Tapfer, L. and Ploog, K. *Phys. Rev. B* 40(14), 9802–9810 Nov (1989).

[88] Massies, J., Turco, F., Saletes, A., and Contour, J. P. *Journal of Crystal Growth* 80(2), 307 – 314 (1987).

[89] Dussaigne, A., Damilano, B., Grandjean, N., and Massies, J. *J. Cryst. Growth* 251(1-4), 471–475 apr (2003).

[90] Gerthsen, D., Hahn, E., Neubauer, B., Potin, V., Rosenauer, A., and Schowalter, M. *phys. stat. sol. (c)* 0(6), 1668–1683 (2003).

[91] Schulze, F., Bläsing, J., Dadgar, A., and Krost, A. *Applied Physics Letters* 82(25), 4558–4560 (2003).

[92] Chen, H., Feenstra, R., Northrup, J., Neugebauer, J., and Greve, D. *MRS Int. J. N. S. R.* 6, 1 (2001).

[93] Mayrock, O., Wünsche, H.-J., and Henneberger, F. *Phys. Rev. B* 62(24), 16870–16880 dec (2000).

[94] Jinschek, J., Erni, R., Gardner, N., Kim, A., and Kisielowski, C. *Solid State Communications* 137(4), 230 – 234 (2006).

[95] Gerthsen, D., Neubauer, B., Rosenauer, A., Stephan, T., Kalt, H., Schön, O., and Heuken, M. *Applied Physics Letters* 79(16), 2552–2554 (2001).

[96] Hangleiter, A., Hitzel, F., Lahmann, S., and Rossow, U. *Appl. Phys. Lett.* 83, 1169 (2003).

[97] Piprek, J., editor. *Nitride semiconductor devices: principles and simulation*. Wiley-VCH-Verl, Weinheim, (2007).

[98] Minsky, M. S., Fleischer, S. B., Abare, A. C., Bowers, J. E., Hu, E. L., Keller, S., and Denbaars, S. P. *Appl. Phys. Lett.* 72(9), 1066–1068 (1998).

[99] Queren, D., Schillgalies, M., Avramescu, A., Brüderl, G., Laubsch, A., Lutgen, S., and Strau, U. *Journal of Crystal Growth* 311(10), 2933 – 2936 (2009).

[100] Keller, S., Keller, B. P., Kapolnek, D., Abare, A. C., Masui, H., Coldren, L. A., Mishra, U. K., and Baars, S. P. D. *Applied Physics Letters* 68(22), 3147–3149 (1996).

[101] Zeimer, U., Jahn, U., Hoffmann, V., Weyers, M., and Kneissl, M. *Journal of Electronic Materials* 39, 677–683 (2010). 10.1007/s11664-010-1159-7.

[102] Nakamura, S. and Mukai, T. *Jpn. J. Appl. Phys.* 31, L1457–L1459 (1992).

[103] Doppalapudi, D., Basu, S. N., K. F. Ludwig, J., and Moustakas, T. D. *Journal of Applied Physics* 84(3), 1389–1395 (1998).

[104] Naranjo, F. B., Sánchez-García, M. A., Calle, F., Calleja, E., Jenichen, B., and Ploog, K. H. *Applied Physics Letters* 80(2), 231–233 (2002).

[105] Chen, F., Cartwright, A. N., Sweeney, P. M., and Cheung, M. C. *Mat. Res. Soc. Symp.* 693, I6.27.1–6 (2002).

[106] Liu, C. H., Su, Y. K., Wen, T. C., Chang, S. J., and Chuang, R. W. *J. Cryst. Growth* 254(3-4), 336–341 jul (2003).

[107] Gurskii, A., Pavlovskii, V., Lutsenko, E., Zubialevich, V., Yablonskii, G., Kalisch, H., Szymakowski, A., Jansen, R., Alam, A., Schineller, B., and Heuken, M. *J. Cryst. Growth* 275(1-2), e1047–e1051 feb (2005).

[108] Yablonskii, G. P., Pavlovskii, V. N., Lutsenko, E. V., Zubialevich, V. Z., Gurskii, A. L., Kalisch, H., Szymakowski, A., Jansen, R. H., Alam, A., Schineller, B., and Heuken, M. *Appl. Phys. Lett.* 85(22), 5158–5160 (2004).

[109] Cho, Y.-H., Song, J. J., Keller, S., Minsky, M. S., Hu, E., Mishra, U. K., and DenBaars, S. P. *Appl. Phys. Lett.* 73(8), 1128–1130 (1998).

[110] Bosi, M. and Fornari, R. *J. Cryst. Growth* 265(3-4), 434–439 may (2004).

[111] Kwon, Y.-H., Gainer, G. H., Bidnyk, S., Cho, Y. H., Song, J. J., Hansen, M., and DenBaars, S. P. *Applied Physics Letters* 75(17), 2545–2547 (1999).

[112] Sonderegger, S., Feltin, E., Merano, M., Crottini, A., Carlin, J. F., Sachot, R., Deveaud, B., Grandjean, N., and Ganiere, J. D. *Appl. Phys. Lett.* 89(23), 232109–3 dec (2006).

[113] Sugahara, T., Hao, M., Wang, T., Nakagawa, D., Nao, Y., Nishino, K., and Sakai, S. *Jpn. J. Appl. Phys.* 37, L1195–L1198 (1998).

[114] Neugebauer, J. *phys. stat. sol. (c)* 90(6), 1651–1667 (2003).

[115] Musikhin, Y. G., Gerthsen, D., Bedarev, D. A., Bert, N. A., Lundin, W. V., Tsatsul'nikov, A. F., Sakharov, A. V., Usikov, A. S., Alferov, Z. I., Krestnikov, I. L., Ledentsov, N. N., Hoffmann, A., and Bimberg, D. *Appl. Phys. Lett.* 80(12), 2099–2101 (2002).

[116] Lu, D., Florescu, D. I., Lee, D. S., Ramer, J. C., Parekh, A., Merai, V., Li, S., Gardner, J. J., Begarney, M. J., and Armour, E. A. *phys. stat. sol. (a)* 202(5), 795–798 (2005).

[117] Uchida, S., Takeya, M., Ikeda, S., Mizuno, T., Fujimoto, T., Matsumoto, O., Goto, S., Tojyo, T., and Ikeda, M. *Selected Topics in Quantum Electronics, IEEE Journal of* 9(5), 1252–1259 (2003).

[118] Perlin, P., Suski, T., Leszczynski, M., Prystawko, P., Swietlik, T., Marona, L., Wisniewski, P., Czernecki, R., Nowak, G., Weyher, J., Kamler, G., Borysiuk, J., Litwin-Staszewska, E., Dmowski, L., Piotrzkowski, R., Franssen, G., Grzanka, S., Grzegory, I., and Porowski, S. *Journal of Crystal Growth* 281(1), 107 – 114 (2005). The Internbational Workshop on Bulk Nitride Semiconductors III.

[119] Nagahama, S., Yanamoto, T., Sano, M., and Mukai, T. *Jpn. J. Appl. Phys.* 40(Part 1, No. 5A), 3075–3081 (2001).

[120] Nagahama, S., Iwasa, N., Senoh, M., Matsushita, T., Sugimoto, Y., Kiyoku, H., Kozaki, T., Sano, M., Matsumura, H., Umemoto, H., Chocho, K., and Mukai, T. *Japanese Journal of Applied Physics* 39(Part 2, No. 7A), L647–L650 (2000).

[121] Jacobs, K., Daele, B. V., Leys, M. R., Moerman, I., and Tendeloo, G. V. *J. Cryst. Growth* 248, 498–502 feb (2003).

[122] Liu, J. P., Jin, R. Q., Zhu, J. J., Zhang, J. C., Wang, J. F., Wu, M., Chen, J., Wang, Y. T., and Yang, H. *J. Cryst. Growth* 264(1-3), 53–57 mar (2004).

[123] Moon, Y.-T., Kim, D.-J., Song, K.-M., Choi, C.-J., Han, S.-H., Seong, T.-Y., and Park, S.-J. *J. Appl. Phys.* 89(11), 6514–6518 (2001).

[124] Olaizola, S. M., Pendlebury, S. T., O'Neill, J. P., Mowbray, D. J., Cullis, A. G., Skolnick, M. S., Parbrook, P. J., and Fox, A. M. *J. Phys. D: Appl. Phys.* 35(7), 599 (2002).

[125] Zheng, X. H., Chen, H., Yan, Z. B., Yu, H. B., Li, D. S., Han, Y. J., Huang, Q., and Zhou, J. M. *J. Cryst. Growth* 257(3-4), 326–332 oct (2003).

[126] Park, E.-H., Kang, D. N. H., Ferguson, I. T., Park, S.-K. J. J.-S., and Yoo, T.-K. *Applied Physics Letters* 90(3), 031102 (2007).

[127] Hansen, M., Piprek, J., Pattison, P. M., Speck, J. S., Nakamura, S., and DenBaars, S. P. *Appl. Phys. Lett.* 81(22), 4275–4277 nov (2002).

[128] Chang, Y., Luo, C., Kuo, H., Kuo, Y., Lin, C., and Wang, S. *Japanese Journal of Applied Physics* 44(11), 7916–7918 (2005).

[129] Kurth, F., Alam, A., Brien, D.and Dauelsberg, M., Schineller, B., Kaeppeler, J., and Heuken, M. Poster at ICMOVPE XIII, May 22-26 (2006).

[130] Heuken, M., Protzmann, H., Schoen, O., Luenenbuerger, M., Juergensen, H., Bremser, M., and Woelk, E. In *Wide-bandgap semiconductors for high-power, high-frequency, and high-temperature applications*, volume 572, 321. Materials Research Society, (1999). symposium held April 5-8, 1999, San Francisco, California, USA.

[131] Koukitu, A., Taki, T., Takahashi, N., and Seki, H. *J. Cryst. Growth* 197(1-2), 99–105 feb (1999).

[132] Martin, C., Dauelsberg, M., Protzmann, H., Boyd, A., Thrush, E., Heuken, M., Talalaev, R., Yakovlev, E., and Kondratyev, A. *Journal of Crystal Growth* 303(1), 318 – 322 (2007). Proceedings of the Fifth Workshop on Modeling in Crystal Growth - IWMCG-5.

[133] Feng, X., Huang, Y., and Rosakis, A. *International Journal of Solids and Structures* 45(13), 3688 – 3698 (2008). Special Issue Honoring K.C. Hwang - Fracture, Plasticity, Micro- and Nanomechanics, Special Issue Honoring K.C. Hwang.

[134] Ito, K., Hiramatsu, K., Amano, H., and Akasaki, I. *J. Cryst. Growth* 104(2), 533 – 538 (1990).

[135] Bandić, Z. Z., Bridger, P. M., Piquette, E. C., and McGill, T. C. *Applied Physics Letters* 73(22), 3276–3278 (1998).

[136] Kumakura, K., Makimoto, T., Kobayashi, N., Hashizume, T., Fukui, T., and Hasegawa, H. *Appl. Phys. Lett.* 86(5), 052105–3 jan (2005).

[137] Ino, N. and Yamamoto, N. *Applied Physics Letters* 93(23), 232103 (2008).

[138] Hader, J., Moloney, J. V., and Koch, S. W. *Appl. Phys. Lett.* 89(17), 171120 (2006).

[139] Schubert, E., Gobel, E., Horikoshi, Y., Ploog, K., and Queisser, H. *Phys. Rev. B, Condens. Matter* 30(2), 813–820 (1984).

[140] Hangleiter, A., Im, J., Off, J., and Scholz, F. *Physica Status Solidi B Basic Research* 216, 427–430 (1999).

# List of Symbols and Abbreviations

(0001) polar c-plane ∥ (0001)

$(10\bar{1}0)$ non-polar m-plane ∥ $(10\bar{1}0)$

$(10\bar{1}1)$ semi-polar plane ∥ $(10\bar{1}1)$

$(10\bar{1}5)$ asymmetric reflex

$(2\bar{1}02)$ semi-polar r-plane ∥ $(1\bar{1}02)$

$(2\bar{1}\bar{1}0)$ non-polar a-plane ∥ $(2\bar{1}\bar{1}0)$

$(2\bar{1}\bar{1}2)$ semi-polar plane ∥ $(2\bar{1}\bar{1}2)$

$\vec{b}$ Burgers vector

1D one-dimensional

2D two-dimensional

3D three-dimensional

$d_{\mathrm{QW}} + d_{\mathrm{bar}}$ MQW period

$a_{\parallel}$ in-plane lattice constant

$a_{\perp}$ out-of-plane lattice constant

AFM atomic force microscopy

Aix200-HT horizontal Aixtron AIX 200HT reactor with 1×2 inch configuration

Aix2400G3-HT horizontal Aixtron AIX 2400G3-HT planetary reactor with 11×2 inch configuration

Al aluminum

$\mathrm{Al_xGa_{(1-x)}N}$ aluminum gallium nitride

AlGaN aluminum gallium nitride

AlN aluminum nitride

$\alpha$ intensity absorption coefficient

$\alpha$ optical absorption coefficient

AR active region

Au gold

BA-LD broad area laser diode

BFC Burton, Frank and Cabrera

CL cladding layer

$\mathrm{Cp_2Mg}$ biscyclopentadienyl-magnesium

CsIn cesium indium compound

CW continuous wave

$d_{\mathrm{bar}}$ quantum barrier thickness

$d_{\mathrm{bar}}$ quantum barrier width

$d_{\mathrm{cap}}$ cap thickness

$d_{\mathrm{QW}}$ quantum well width

$d_{\mathrm{well}}$ quantum well width

$\Delta\mu$ driving force to grow a crystal

DNA desoxyribonucleic acid

DQW double quantum well

$e_{\mathrm{ij}}$ elements of the piezoelectric tensor

$E_{\mathrm{g}}^{\mathrm{abs}}$ band gap energy of fully strained material

$E_{\mathrm{g}}^{\mathrm{rlx}}$ band gap energy of fully relaxed material

EBL electron blocking layer

ELO epitaxial lateral overgrowth

$\epsilon_{ij}$ independent strain components

$\epsilon_{xx}$ lattice mismatch of $a_{\parallel}$

$F_p$ net polarization strength

$F_{pz}$ piezoelectric field strength

$f_{sat}$ satellite rotation flux

$f_{tot}$ total flux

fbh Ferdinand-Braun-Institut, Leibniz-Institut für Höchstfrequenztechnik

FWHM full width half maximum

$g$ optical material gain

$g_{mod}$ optical gain of the mode

Ga gallium

$\Gamma$ optical confinement factor

GaN:Mg magnesium-doped p-type gallium nitride

GaN:Si silicon-doped n-type gallium nitride

GaN gallium nitride

H atomic hydrogen

$H_2$ hydrogen

$h_{crit}$ critical layer thickness for pseudomorphic growth

HeCd helium cadmium

HRTEM high resolution electron microscopy

HR-XRD high resolution x-ray diffraction

HR-XRR high resolution x-ray reflectometry

HT high temperature

$i_{th}$ optical threshold power density

In indium

InGaN:Si silicon-doped n-type indium gallium nitride

InGaN indium gallium nitride

InN indium nitride

$j_{th}$ threshold current density

$\kappa$ wafer curvature

KOH potassium hydroxide

l distance of the growth steps

$\lambda_{CL}$ LT-CL wavelength

$\lambda_{las}$ lasing wavelength

$\lambda_{PL}$ PL wavelength

LASTIP Laser Technology Integrated Program

LD semiconductor laser diode

LED light emitting diode

L-I light output power versus current

LT low temperature

LT-CL low temperature cathodoluminescence

Mg magnesium

ML monolayer

MOVPE metal organic vapor phase epitaxy

MQW multiple quantum well

n.i.d. GaN non-intentionally doped gallium nitride

N nitrogen

$N_2$ nydrogen

$n$ refractive index

Nd:YAG neodymium-doped yttrium aluminum garnet

$NH_3$ ammonia

$\nu_{In}$ indium incorporation efficiency

oLD optically pump-able laser structure

$\Omega - 2\Theta$ Omega-2Theta scan

$P$ net polarization

$P_{exc}$ excitation power

$P_{pz}$ piezoelectric polarization

$p_{reactor}$ reactor pressure

$P_{sp}$ spontaneous polarization

Pd palladium

P-I light output power diode current characteristics

PL photoluminescence

P-U-I light output power diode voltage current characteristic

$Q_x$ reciprocal space x-coordinate

$Q_z$ reciprocal space z-coordinate

QCSE quantum-confined Stark effect

QIP quasi 2D semiconductor laser simulation program by H.Wenzel [50]

QW quantum well

R relaxation

$r_{rms}$ root mean square roughness

RF radio frequency

RHEED reflection high-energy electron diffraction

RSM reciprocal space mapping

RT room temperature

RTA rapid thermal annealing

SE secondary electrons

SEM scanning electron microscope

Si silicon

$Si_2H_6$ disilane

$\sigma$ standard deviation

SILENSe software tool for light emitting diode (LED) bandgap engineering [51]

SIMS secondary ion mass spectroscopy

SiN silicon nitride

SL single layer

SPSL short-period superlattice

$T_{AR}$ $T_{proc}$ for active region growth

$T_{bar}$ $T_{proc}$ for quantum barrier growth

$t_{bar}$ quantum barrier growth time

$T_G$ growth temperature

$T_{pocket}$ temperature of the pocket calculated from the pocket reflectivity at 950 nm

$T_{proc}$ process temperature measured at the backside of the susceptor

$T_{QW}$ $T_{proc}$ for quantum well growth

$t_{QW}$ quantum well growth time

$t_{seg}$ time available for segregation

$T_{surface}$ temperature of the wafer surface calculated from the wafer reflectivity at 400 nm

$\tau_{rad}$ radiative carrier life time

TD threading dislocation

TDD threading dislocation density

TD-PL temperature-dependent photoluminescence

TEGa triethylgallium

TEM transmission electron microscopy

Ti titanium

TMAl trimethylaluminum

TMGa trimethylgallium

TMIn trimethylindium

TQW triple quantum well

TR-PL time-resolved photoluminescence

UV ultra violet

$W(\varphi, \theta)$ strain energy

WGL wave guiding layer

$x_0$ converging In mole fraction

$x_{QW}$ QW In mole fraction

$x_s$ diffusion length of an ad-atom

$x_{\text{solid}}^{\text{Al}}$ molar fraction of aluminum in the solid

$x_{\text{solid}}^{\text{In}}$ indium mole fraction in the solid

$x_{\text{vapor}}^{\text{In}}$ molar fraction of indium in the gas phase

# List of Samples and Sample Sets

$A^{\prime\,\mathrm{GaN}}_{\mathrm{templ.}}$ : (E1340) 2.5 $\mu$m n.i.d. GaN on sapphire substrate

$A_{\mathrm{AlGaN}}$ : (E3245-1): 1.5 $\mu$m AlGaN layer with an Al mole fraction in the solid of 0.06 on a sapphire-based GaN template

$A^{\mathrm{d_{bar}}}$ : (E1835, E1835) 5×InGaN/GaN:Si MQW samples with 10 or 7.3 nm thick barriers grown with 75 °C increased $T_{\mathrm{bar}}$ with respect to $T_{\mathrm{QW}}$

$A^{\mathrm{GaN}}_{\mathrm{templ.}}$ : (E1416) 1.2 $\mu$m thick n.i.d. GaN template

$A^{\mathrm{InGaN}}_{\mathrm{d}}$ : (B2741, B2743) 15 or 120 nm thick InGaN SL with $x^{\mathrm{In}}_{\mathrm{vapor}} = 0.35$

$A^{\mathrm{InGaN}}_{\mathrm{spiral}}$ : (E1420) 100 nm thick InGaN layer grown at barrier conditions

$B^{\mathrm{d_{QW}}}$ : (E1905, E1906, E1907, E1908) 4×InGaN/GaN:Si MQW structure with varying $t_{\mathrm{QW}}$ between 40 and 100 s

$B^{\mathrm{InGaN}}_{\tilde{\mathrm{n}}}$ : (B2743, B2744, B2745, B2747, B2774, B2823) 120 nm thick InGaN SL on differently oriented GaN surfaces with $x^{\mathrm{In}}_{\mathrm{vapor}} = 0.2$ or 0.35

$C^{\mathrm{d_{QW}}}$ : (E2334, E2336, E2337) 3×InGaN/GaN:Si MQW structures with varying $t_{\mathrm{QW}}$ between 30 and 60 s on sapphire based GaN template including a AlGaN/GaN:Si SPSL

$D^{\mathrm{T_{AR}}}$ : (E1868, E1869, E1870,E1871) 3×InGaN /InGaN:Si MQW active regions grown at different $T_{\mathrm{AR}}$ between 850 and 890 °C and constant $x^{\mathrm{In}}_{\mathrm{vapor}}$

$D^{\mathrm{T_{AR}}}_{\mathrm{oLD}}$ : (B2912-1, B2912-2, B2912-3,B2912-4) optically pumpable laser structure with 3×InGaN/InGaN:Si MQW active regions grown at different $T_{\mathrm{AR}}$ between 850 and 890 °C and constant $x^{\mathrm{In}}_{\mathrm{vapor}}$

$D^{\mathrm{T_{AR}}}_{\mathrm{LD}}$ : (B2677-1, B2677-2, B2677-3B2677-4) current injection LD structure with 3×InGaN/InGaN:Si MQW active regions grown at different $T_{\mathrm{AR}}$ between 850 and 890 °C and constant $x^{\mathrm{In}}_{\mathrm{vapor}}$

$E^{\mathrm{TMIn}}$ : (E1319, E1328, E1339, E1342) 5×InGaN /silicon-doped n-type indium gallium nitride (InGaN:Si) MQW samples grown with $T_{\mathrm{AR}}$ between 760 and 840 °C and different $x^{\mathrm{In}}_{\mathrm{vapor}}$ but identical $x^{\mathrm{In}}_{\mathrm{solid}} = 0.09$ in the QW

$E_{\mathrm{LD}}^{\mathrm{TMIn}}$ : (B2193) current injection LD structures with 3×InGaN /InGaN:Si MQW active region grown at $T_{\mathrm{AR}} = 850\,^{\circ}\mathrm{C}$

$E_{\mathrm{oLD}}^{\mathrm{TMIn}}$ : (E1194, E1218, E1221, E1353, E1354) optically pumpable laser structures with 3×InGaN /InGaN:Si MQW active region grown at $T_{\mathrm{AR}}$ between 760 and 840 °C and different $x_{\mathrm{vapor}}^{\mathrm{In}}$ but identical $x_{\mathrm{solid}}^{\mathrm{In}} = 0.09$ in the QW

$F_{\mathrm{LD}}^{\mathrm{sapph./GaN}}$ : (B2184,B2479) 404 nm LD heterostructures with standard layout grown on either GaN substrate or sapphire-based GaN template

$G^{\mathrm{sapph./GaN}}$ : (E2711-1, E2711-2): standard 405 nm LD heterostructure grown on sapphire-based GaN template or GaN substrate, respectively

$H^{\mathrm{sapph.}}$ : (E2907-1): 120 ×AlGaN/GaN:Si SPSL on GaN:Si buffer on sapphire substrate

$I^{\mathrm{GaN}}$ : (E2915-1): n-side of LD structure with 450 nm active region on GaN substrate

$I^{\mathrm{sapph.}}$ : (E2915-3): n-side of laser structure with 450 nm active region on sapphire-based substrate

$J_{\mathrm{I}}^{450\,\mathrm{nm}}$ : (E2339) 450 nm optically pumpable laser structure with 1.75 and 7.5 nm thick QWs and barriers and standard 405 nm wave guiding heterostructure layout

$J_{\mathrm{II}}^{450\,\mathrm{nm}}$ : (E2772-2) 450 nm optically pumpable laser structure with 1.75 and 7.5 nm thick QWs and barriers and 200 nm thick n-side GaN wave guides

$J_{\mathrm{III}}^{450\,\mathrm{nm}}$ : (E2772-1) 450 nm optically pumpable laser structure with 1.75 and 7.5 nm thick QWs and barriers and 200 nm thick n-side $In_{0.02}Ga_{0.98}$N wave guides

$K_{\mathrm{II}}^{450\,\mathrm{nm}}$ : (E2771-2) reproduction of $J_{\mathrm{II}}^{450\,\mathrm{nm}}$ with an InGaN /InGaN DQW as active region

$K_{\mathrm{III}}^{450\,\mathrm{nm}}$ : (E2771-1) reproduction of $J_{\mathrm{III}}^{450\,\mathrm{nm}}$ with an InGaN /InGaN DQW as active region

$K\,'^{450\,\mathrm{nm}}_{\mathrm{III}}$ : (E2771-3) reproduction of $K_{\mathrm{II}}^{450\,\mathrm{nm}}$ with reduced In mole fraction of 0.01 in the n-side wave guide

$L_{\mathrm{oLD}}^{450\,\mathrm{nm}}$ : (E2889-1, E2890-1, E2896-1, E2888-1, E2897-1, E2895-1, E2892-1, E2891-1, E2893-1) reproduction of $K_{\mathrm{II}}^{450\,\mathrm{nm}}$ with varied $d_{\mathrm{QW}}$ between 1.5 and 3 nm and varied $x_{\mathrm{QW}}$ between 0.10 and 0.20

$M_{\mathrm{LD}}^{450\,\mathrm{nm}}$ : (B4031-1C) reproduction of the sample with the high temperature barriers of set $M_{\mathrm{oLD}}^{450\,\mathrm{nm}}$ as a current injection LD heterostructure

$M_{\mathrm{oLD}}^{450\,\mathrm{nm}}$ : (E2895-1, E2897-1) optically pumpable laser structures with 3 nm thick QWs but different barrier growth temperatures

$T_{\mathrm{(Al)GaN:Si}}$ : (E1729) 240×AlGaN/GaN:Si SPSL on sapphire-based GaN:Si template

# Danksagung

Die vorliegende Arbeit entstand am Ferdinand-Braun-Institut, Leibniz-Institut für Höchstfrequenztechnik und wurde finanziell im Rahmen des Sonderforschungsbereiches 787 der Deutschen Forschungsgemeinschaft gefördert. Für die Schaffung der wissenschaftlichen Randbedingen möchte ich Prof. Günther Tränkle, Prof. Michael Kneissl und Dr. Markus Weyers danken. Neben diesen Personen gilt mein besonderer Dank Dr. Arne Knauer, Dr. Frank Brunner, Dr. Sven Einfeldt und Dr. Eberhard Richter für hilfreiche Diskussionen und Anregungen bei Epitaxiefragen. Für die Analytik der Proben möchte ich mich bei Dr. Ute Zeimer, Dr. Carsten Netzel, Jan-Robert van Look, Daniel Matthesius, David Fendler, Jessica Schlegel, Anna Mogilatenko, Christian Friedrich, Christoph Stöllmacker, Tobias Arlt und Sohail Hatami bedanken. Dr. Hans Wenzel, Dr. Joachim Piprek und Jan-Robert van Look sei gedankt für die Simulation der Bauelementstrukturen und die Unterstützung bei eigenen Simulationen. Luca Redaelli, Hernan Rodriques und Dr. Sven Einfeldt möchte ich für die Prozessierung der Wafer danken. Thomas Tessaro, Torsten Petzke, Hans-Joachim Pöhls und Helen Lawrenz danke ich für die abgenommene Arbeit bei der Epitaxie, der Prozessierung und der Analytik der Wafer. Nicht zuletzt danke ich Alexandra und Mira für ihre Unterstützung zu Hause.